

**WestminsterResearch**

<http://www.westminster.ac.uk/research/westminsterresearch>

**Digital predistortion of RF amplifiers using baseband injection  
for mobile broadband communications**

**Milan Cabarkapa**

Faculty of Science and Technology

This is an electronic version of a PhD thesis awarded by the University of Westminster. © The Author, 2014.

This is an exact reproduction of the paper copy held by the University of Westminster library.

---

The WestminsterResearch online digital archive at the University of Westminster aims to make the research output of the University available to a wider audience. Copyright and Moral Rights remain with the authors and/or copyright owners.

Users are permitted to download and/or print one copy for non-commercial private study or research. Further distribution and any use of material from within this archive for profit-making enterprises or for commercial gain is strictly forbidden.

---

Whilst further distribution of specific materials from within this archive is forbidden, you may freely distribute the URL of WestminsterResearch:  
(<http://westminsterresearch.wmin.ac.uk/>).

In case of abuse or copyright appearing without permission e-mail  
[repository@westminster.ac.uk](mailto:repository@westminster.ac.uk)

# Digital Predistortion of RF Amplifiers Using Baseband Injection for Mobile Broadband Communications

Milan Cabarkapa

A thesis submitted in partial fulfilment of the  
requirements of the University of Westminster  
for the degree of Doctor of Philosophy

April 2014

## **ABSTRACT**

Radio frequency (RF) power amplifiers (PAs) represent the most challenging design parts of wireless transmitters. In order to be more energy efficient, PAs should operate in nonlinear region where they produce distortion that significantly degrades the quality of signal at transmitter's output. With the aim of reducing this distortion and improve signal quality, digital predistortion (DPD) techniques are widely used. This work focuses on improving the performances of DPDs in modern, next-generation wireless transmitters. A new adaptive DPD based on an iterative injection approach is developed and experimentally verified using a 4G signal. The signal performances at transmitter output are notably improved, while the proposed DPD does not require large digital signal processing memory resources and computational complexity. Moreover, the injection-based DPD theory is extended to be applicable in concurrent dual-band wireless transmitters. A cross-modulation problem specific to concurrent dual-band transmitters is investigated in detail and novel DPD based on simultaneous injection of intermodulation and cross-modulation distortion products is proposed. In order to mitigate distortion compensation limit phenomena and memory effects in highly nonlinear RF PAs, this DPD is further extended and complete generalised DPD system for concurrent dual-band transmitters is developed. It is clearly proved in experiments that the proposed predistorter remarkably improves the in-band and out-of-band performances of both signals. Furthermore, it does not depend on frequency separation between frequency bands and has significantly lower complexity in comparison with previously reported concurrent dual-band DPDs.

## ACKNOWLEDGEMENT

First of all, I would like to thank my director of studies, Dr. D. Budimir, for his excellent supervision, guidance and encouragement throughout the research work. In addition to offering me a research opportunity, he has kept me motivated throughout whole period of my PhD work. Although he had a lot of teaching and research responsibilities, he was always able to find time for discussion and advice that significantly improved my research work and for which I am truly thankful.

I am also grateful to my second supervisor, Dr. A. Tarczynski, for his useful suggestions, advice and assistance.

Next, I would like to express my deepest gratitude to my second supervisor, Dr. N. Neskovic, for her encouragement and extremely useful advice and suggestions. She was always able to find time, even when she was busy, for long-term discussions that notably help me and my research work.

I would also like to thank Dr. A. Neskovic, especially for his introduction and recommendation to Dr. D. Budimir.

The finance support provided by the Fund for Young Talents of Ministry of Youth and Sport of Serbia is greatly acknowledged.

Finally, I would like to dedicate this thesis to my friends and family who have always supported me.

# Table of Contents

<b>ABSTRACT</b> .....	<b>ii</b>
<b>ACKNOWLEDGEMENT</b> .....	<b>iii</b>
<b>LIST OF FIGURES</b> .....	<b>viii</b>
<b>LIST OF TABLES</b> .....	<b>xiv</b>
<b>LIST OF ABBREVIATIONS</b> .....	<b>xv</b>
<b>1. INTRODUCTION</b> .....	<b>1</b>
1.1. Overview of Recent Research .....	4
1.2. Aims and Objectives of the Research .....	5
1.2.1. Aims .....	5
1.2.2. Objectives .....	6
1.3. Outline of the Thesis.....	8
1.4. References.....	11
<b>2. Nonlinear Distortion in Power Amplifiers for Wireless Transmitters</b> .....	<b>14</b>
2.1. Introduction.....	14
2.2. PA System Parameters .....	14
2.2.1. Gain .....	14
2.2.2. Bandwidth .....	15
2.2.3. Power efficiency .....	15
2.2.4. P1dB Compression Point.....	16
2.2.5. Third Order Intercept Point (IP3).....	16
2.2.6. Power Back-off .....	18
2.2.7. Peak to Average Power Ratio (PAPR).....	19
2.3. Memory Effects .....	20
2.4. Signal Quality Parameters .....	21
2.4.1. Spectrum Regrowth.....	21
2.4.2. Adjacent Channel Power Ratio (ACPR).....	21
2.4.3. Error Vector Magnitude (EVM) .....	22
2.5. Performance Evaluation of PA Modelling.....	23
2.5.1. Mean Squared Error .....	23
2.5.2. Normalised Mean Squared Error .....	24
2.5.3. Adjacent Channel Error Power Ratio .....	24
2.6. OFDM Modulation System.....	25
2.7. LTE Technology .....	26
2.7.1. Transmission Bandwidths.....	27
2.7.2. Supported Frequency Bands .....	27
2.8. Multi-branch and Multi-frequency MIMO Transmitters .....	28

2.8.1.	Distortion in Multi-branch MIMO Transmitters.....	29
2.8.2.	Distortion in Multi-frequency MIMO Transmitters.....	31
2.9.	Conclusion.....	33
2.10.	References.....	33
<b>3.</b>	<b>Digital Predistortion Linearisation Techniques.....</b>	<b>36</b>
3.1.	Introduction.....	36
3.2.	DUT Model Extraction.....	37
3.3.	Mathematical Representation of the Models.....	38
3.3.1.	Look-up-table Models.....	38
3.3.2.	Volterra Models.....	39
3.3.3.	Memory Polynomial Models.....	41
3.3.4.	Wiener Model.....	43
3.3.5.	Hammerstein Model.....	43
3.4.	Behavioural Modelling Based Digital Predistortion.....	44
3.4.1.	Identification of DPD Functions – Direct and Indirect Learning Architectures.....	44
3.5.	Digital Predistortion Based on Artificial Neural Networks.....	46
3.6.	Digital Predistortion for Multi-branch MIMO Transmitters.....	49
3.6.1.	Crossover Digital Predistortion (CO-DPD).....	50
3.6.2.	Digital Predistortion for Multi-branch MIMO Transmitters Based on Combined Feedback.....	52
3.6.3.	Simplified Crossover Digital Predistortion (Simplified CO-DPD).....	55
3.7.	Digital Predistortion for Multi-frequency MIMO Transmitters.....	59
3.7.1.	2-D DPD Based on Memory Polynomials.....	61
3.7.2.	Low-complexity 2-D DPD.....	63
3.7.3.	2-D Augmented Hammerstein.....	65
3.7.4.	2-D Enhanced Hammerstein.....	66
3.7.5.	Dual-band DPD Based on Look-up-tables.....	67
3.7.6.	Extended-RVFTDNN for Dual-band Transmitters.....	68
3.8.	Band-limited Digital Predistortion.....	70
3.9.	Conclusion.....	73
3.10.	References.....	73
<b>4.</b>	<b>Injection-based Linearisation Techniques.....</b>	<b>80</b>
4.1.	Introduction.....	80
4.2.	RF Injection Techniques.....	81
4.2.1.	Second Harmonic Injection.....	81
4.2.2.	Frequency Deference Injection.....	84
4.2.3.	Combined Frequency Deference and Second Harmonic Injection.....	85
4.2.4.	Combined Frequency Deference and Third Harmonic Injection.....	87
4.3.	Baseband Components Injection Digital Predistortion.....	90

4.4.	Iterative Injection Digital Predistortion.....	92
4.5.	Conclusion .....	97
4.6.	References.....	98
<b>5.</b>	<b>Adaptive DPD for 4G Wireless Transmitters.....</b>	<b>100</b>
5.1.	Introduction.....	100
5.2.	Proposed Approach.....	100
5.3.	Least Square Regression (LSR).....	103
5.4.	Experimental Results.....	106
5.5.	Conclusion .....	108
5.6.	References.....	108
<b>6.</b>	<b>2-D DPD for Concurrent Dual-band Transmitters.....</b>	<b>110</b>
6.1.	Introduction.....	110
6.2.	Proposed 2-D DPD.....	110
6.3.	Experimental Setup of Concurrent Dual-band Transmitter.....	114
6.4.	Proposed Dual-band PA Characterisation .....	115
6.5.	Experimental 2-D DPD Results.....	118
6.6.	Conclusion .....	120
6.7.	References.....	120
<b>7.</b>	<b>A Generalised Linearity Enhancement Architecture for Concurrent Dual-band Transmitters .....</b>	<b>123</b>
7.1.	Introduction.....	123
7.2.	Fundamental Frequency Model for Concurrent Dual-band Transmitters.....	124
7.3.	Baseband Simulation Analysis.....	129
7.4.	Proposed Generalised DPD System.....	131
7.4.1.	Nonlinearity Compensation by Simultaneous Injection .....	132
7.4.2.	Iterative Simultaneous Injection .....	133
7.4.3.	Memory Effects Mitigation .....	135
7.5.	Experimental Setup .....	140
7.6.	PA Characterisation.....	141
7.7.	Concurrent Two-tone Test.....	142
7.8.	Experimental Extraction of Memory Mitigation Coefficients.....	144
7.9.	Experimental DPD Results .....	145
7.10.	Extension of the Proposed DPD for Multi-band Wireless Transmitters .....	147
7.11.	Discussion.....	148
7.12.	Conclusion .....	151
7.13.	References.....	152
<b>8.</b>	<b>CONCLUSION .....</b>	<b>155</b>
8.1.	Thesis Summary .....	155
8.2.	ORIGINALITY and CONTRIBUTIONS to KNOWLEDGE.....	158
8.3.	Future Work.....	160

<b>LIST OF PUBLICATIONS</b> .....	<b>163</b>
<b>APPENDIX</b> .....	<b>164</b>
Data Sheets for the Power Amplifiers.....	164

## LIST OF FIGURES

### Chapter 1

**Figure 1-1:** Cisco Forecasts 11.2 Exabytes per Month of Mobile Data Traffic by 2017 [1.3]

**Figure 1-2:** General block diagram of a radio base station

**Figure 1-3:** Radio base station energy consumption [1.6].

**Figure 1-4:** The transfer characteristics of an ideal and a real power amplifier

**Figure 1-5:** Functional block diagram of digital predistortion for power amplifiers

### Chapter 2

**Figure 2-1:** 3-dB bandwidth of the PA

**Figure 2-2:** The input-output and gain characteristics of a PA

**Figure 2-3:** The second and third order intercepts points

**Figure 2-4:** The output back-off, peak back-off and peak-to-average power ratio for power amplifiers

**Figure 2-5:** Typical IMD characteristics of the PA with memory effects evaluated using two-tone tests with different tone spacing

**Figure 2-6:** Improvements in spectrum regrowth in lower and upper adjacent channels

**Figure 2-7:** Block diagram of OFDM transmitter and receiver

**Figure 2-8:** Dual-input wireless transmitter for 2x2 MIMO communication system

**Figure 2-9:** Block diagram of concurrent dual-band transmitter

**Figure 2-10:** Power spectrum of the signal at: (a) the input and (b) output of a dual-band transmitter

## Chapter 3

**Figure 3-1:** The fundamental concept of digital predistortion

**Figure 3-2:** Behavioural model extraction procedure. Key steps from measurements to model validation

**Figure 3-3:** Direct learning DPD architecture

**Figure 3-4:** Indirect learning DPD architecture

**Figure 3-5:** RVFTDNN and RVRNN schematics [3.28]

**Figure 3-6:** A generalised real-valued two hidden layers ANN model for a PA [3.29]

**Figure 3-7:** CO-DPD model for dual-branch transmitters

**Figure 3-8:** Multi-branch MIMO transmitter model: (a) with multiple feedbacks (b) with selector based shared feedback (c) with combiner based shared feedback

**Figure 3-9:** The baseband equivalent N-MIMO OFDM transmitter with simplified CO-DPD

**Figure 3-10:** 2-D dual-cell DPD architecture

**Figure 3-11:** Block diagram of 2D augmented Hammerstein (2D-AH) model

**Figure 3-12:** The topology of extended-RVTDNN for concurrent dual-band behavioural modelling [3.52]

**Figure 3-13:** Band-limited Volterra series model

## Chapter 4

**Figure 4-1:** Second-order products injection system

**Figure 4-2:** Feedback-based second-order products injection circuit

**Figure 4-3:** RF injection technique using second harmonic and frequency difference

**Figure 4-4:** RF injection technique using third harmonic and frequency difference

**Figure 4-5:** Block diagram of a third-order baseband component injection

**Figure 4-6:** Block diagram of the digital predistorter using iterative injection of the in-band distortion components

## Chapter 5

**Figure 5-1:** Functional block diagram of the proposed predistorter

**Figure 5-2:** AM/AM characteristic used to extract the memoryless model for a ZFL-500 PA

**Figure 5-3:** Experimental setup

**Figure 5-4:** Spectrum regrowth improvement of PA downlink LTE signal

## Chapter 6

**Figure 6-1:** Functional block diagram of proposed predistorter as a part of concurrent dual-band transmitter

**Figure 6-2:** Measurement setup of concurrent dual-band transmitter

**Figure 6-3:** Comparisons of measured and modelled ZFL-500 PA transfer characteristics in single and dual-band transmitter mode: (a) operating frequency 400 MHz (b) operating frequency 500 MHz

**Figure 6-4:** Comparisons of measured and modelled Gain in single and dual-band transmitter mode: (a) operating frequency 400 MHz (b) operating frequency 500 MHz

**Figure 6-5:** The PSD responses in both operating frequencies of concurrent dual-band transmitter: (a)  $f_{lower} = 400\text{MHz}$ , (b)  $f_{upper} = 500\text{MHz}$

## Chapter 7

**Figure 7-1:** The cause of IM and CM distortion components

**Figure 7-2:** Power spectrum at the input and output of a dual-band transmitter (concurrent two-tone test)

**Figure 7-3:** Comparisons of simulated IM and CM distortion components for OFDM signals with variable ratio between occupied bandwidths of signals (BW1 and BW2) and their powers (PW1 and PW2): (a)  $BW1/BW2 = 1$ ,  $PW1/PW2 = 1$  (b)  $BW1/BW2 = 2$ ,  $PW1/PW2 = 2$  (c)  $BW1/BW2 = 4$ ,  $PW1/PW2 = 4$  (d)  $BW1/BW2 = 8$ ,  $PW1/PW2 = 8$ .

**Figure 7-4:** Functional block diagram of proposed predistorter as a part of concurrent dual-band transmitter

**Figure 7-5:** Baseband voltage levels of I and Q components: (a) QPSK (b) 16-QAM

**Figure 7-6:** Proposed memory mitigation in case of OFDM signal

**Figure 7-7:** Measurement setup of concurrent dual-band transmitter (CFH 2162-P3 PA was used as DUT)

**Figure 7-8:** Comparisons of measured and modelled PA transfer characteristics in single and dual-band transmitter mode: (a) operating frequency 880 MHz (b) operating frequency 2.14 GHz

**Figure 7-9:** Memory effects as sweep frequency spacing in lower band (a) lower band, (b) upper band

**Figure 7-10:** Memory effects as sweep frequency spacing in upper band (a) lower band, (b) upper band

**Figure 7-11:** Magnitude and phase of the normalised frequency response for three power levels (lower band)

**Figure 7-12:** Magnitude and Phase of the normalised frequency response for three power levels (upper band)

**Figure 7-13:** The PSD responses of concurrent dual-band transmitter (a) Scenario I, LTE 1.4 MHz – lower band, WCDMA – upper band (b) Scenario II, LTE 3 MHz – lower band, WCDMA – upper band (c) Scenario III, LTE 5 MHz – lower band, WCDMA – upper band

## LIST OF TABLES

### Chapter 2

**TABLE 2-1:** Transmission bandwidth configuration

**TABLE 2-2:** EUTRA operating bands

### Chapter 7

**TABLE 7-1:** Analytical forms of IM and CM distortion components

**TABLE 7-2:** BPSK modulation mapping

**TABLE 7-3:** QPSK modulation mapping

**TABLE 7-4:** 16-QAM modulation mapping

**TABLE 7-5:** 64-QAM modulation mapping

**TABLE 7-6:** The frequencies of intermodulation and cross-modulation products

**TABLE 7-7:** EVM Results

**TABLE 7-8:** Comparisons of this work with recent works on concurrent dual-band wireless transmitters

**TABLE 7-9:** Number of FLOPs for different operations performed into DSP

## **LIST OF ABBREVIATIONS**

ACEPR - Adjacent Channel Error Power Ratio

ACPR - Adjacent Channel Power Ratio

ADC - Analogue-to-Digital Conversion

ADS - Advanced Design System

AM - Amplitude Modulation

ANN - Artificial Neural Network

BJT - Bipolar Junction Transistor

BPF - Band-Pass Filter

CW - Continuous Wave

CM - Cross Modulation

DAC - Digital-to-Analogue Converter

DPD - Digital Predistortion

DSP - Digital Signal Processing

DUT - Device Under Test

ESG - Electronic Signal Generator

EVM - Error Vector Magnitude

ETSI - European Telecommunications Standards Institute

E-UTRA - Evolved-UMTS Terrestrial Radio Access

FFT - Fast Fourier Transform

FET - Field-Effect Transistor

FIR - Finite Impulse Response

4G - Fourth Generation

FDD - Frequency Division Duplex

GSM - Global System for Mobile communications

HSPA - High Speed Packet Access

ICT - Information Communication Technology

IM - Intermodulation

IM3 - Third-Order Intermodulation

IP3 - Third-Order Intercept Point

IMD - Intermodulation Distortion

IFFT - Inverse Fast Fourier Transform

LO - Local Oscillator

LTE - Long-Term Evolution

LUT - Look-Up-Table

LPF - Low-Pass Filter

MSE - Mean Squared Error

MIMO - Multiple Input Multiple Output

NMSE - Normalised Mean Squared Error

OFDM - Orthogonal Frequency Division Multiplexing

OBO - Output Back-Off

PAPR - Peak-to-Average Power Ratio

PBO - Peak Back-Off

PM - Phase Modulation

PD - Predistortion

PA - Power Amplifier

PSD - Power Spectrum Density

QAM - Quadrature Amplitude Modulation

QPSK - Quadrature Phase Shift Keying

RBS - Radio Base Station

RF - Radio Frequency

SISO - Single Input Single Output

3GPP - Third Generation Partnership Project

TDD - Time Division Duplex

2-D DPD - Two-dimensional Digital Predistortion

UMTS - Universal Mobile Telecommunication System

UE - User Equipment

VSA - Vector Signal Analyser

WCDMA - Wideband Code Division Multiple Access

WiMAX - Worldwide Interoperability for Microwave Access

## 1. INTRODUCTION

There are two persons without whom today's modern wireless communications would have never been possible, the first one being Nikola Tesla, the second one being Claude Shannon. On the one hand, it was Nikola Tesla who invented the radio and thus, for the first time, introduced us to the idea to wirelessly transfer communication messages [1.1]. On the other hand, Claude Shannon showed us how to transmit information through a channel reliably by describing his theory in "A Mathematical Theory in Communication" [1.2]. This work was fundamental for modern, stable communication.

Wireless communications represent one of the most developing areas nowadays. Moreover, the main trend in the future will be a rapid increase in network capacity requirements by users. As can be seen from Cisco forecast, shown in Figure 1-1, mobile data traffic will grow exponentially in the next few years [1.3]. On the whole, mobile data traffic is expected to grow to 11.2 exabytes per month by 2017. This is a 13-fold increase over 2012.

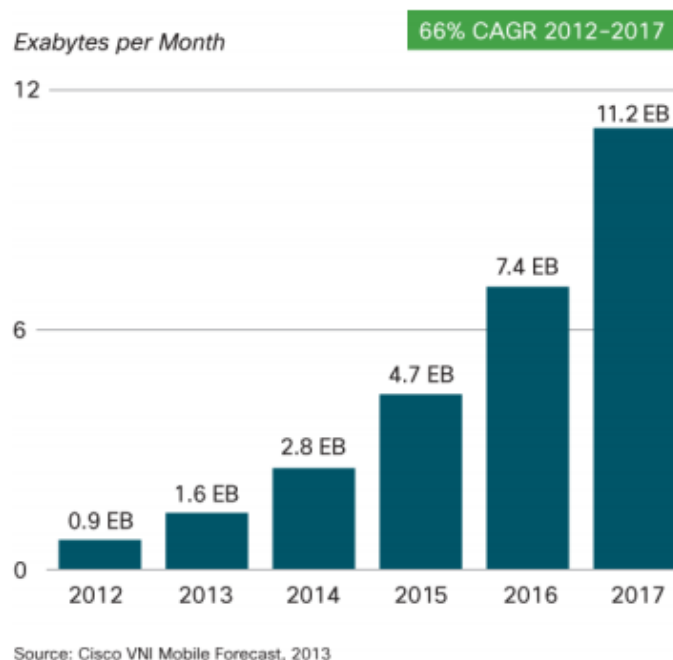


**Figure 1-1:** Cisco Forecasts 11.2 Exabytes per Month of Mobile Data Traffic by 2017 [1.3]

High capacity requirements require radio network solutions that have improved energy-efficiency. These energy-efficiency improvements without enduring the loss of signal quality are becoming an emerging goal of mobile operators and equipment designers. Energy cost accounts for as much as a half of mobile operators' operational expenses. Not only are solutions that improve energy-efficiency environmentally friendly, but they support sustainable, profitable business as well [1.4]. A lot of energy is consumed every year by the telecom infrastructures. The global Information Communication Technology (ICT) industry accounts for about 2% of the total human CO<sub>2</sub> footprint [1.5], [1.6]. Of that 2% CO<sub>2</sub> emission, 30% are accounted for by the world-wide telecom infrastructures and devices. A general block diagram of Radio Base Station (RBS), an essential part of mobile networks, is shown in Figure 1-2.

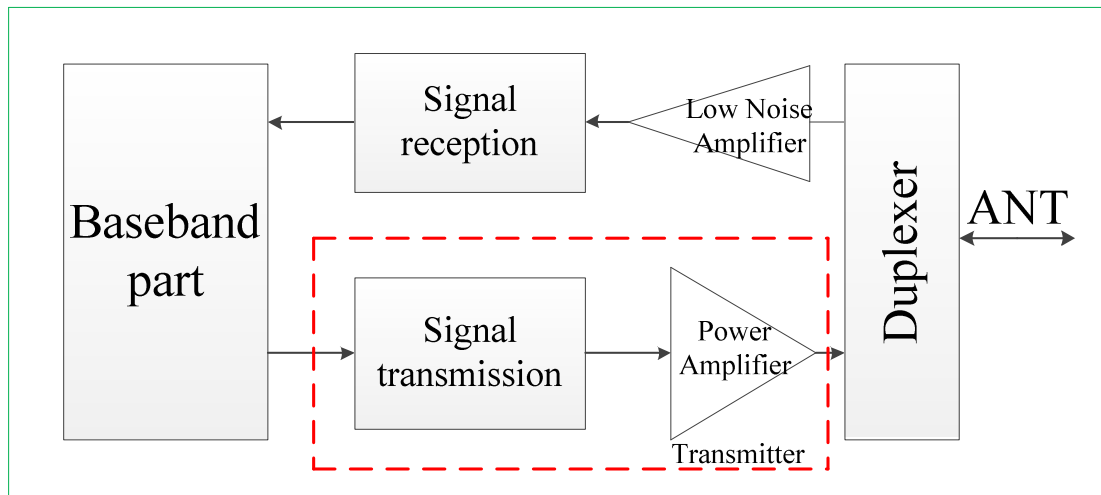


**Figure 1-2:** General block diagram of a radio base station

However, RBSs consume most of the power. The main question is where this power goes. Figure 1-3 shows the energy consumption pertaining to the different parts of a RBS [1.7]. From this figure, it is clear that Power Amplifiers (PAs) are the heaviest energy consumer in RBSs, consuming more than three quarters of the total power. On one hand, in order to achieve high efficiency and saving energy, PAs need to work in the highly nonlinear peak power regime. On the other hand, in that regime, PAs exhibit nonlinear distortion that creates problems related to preserving high signal quality [1.5].

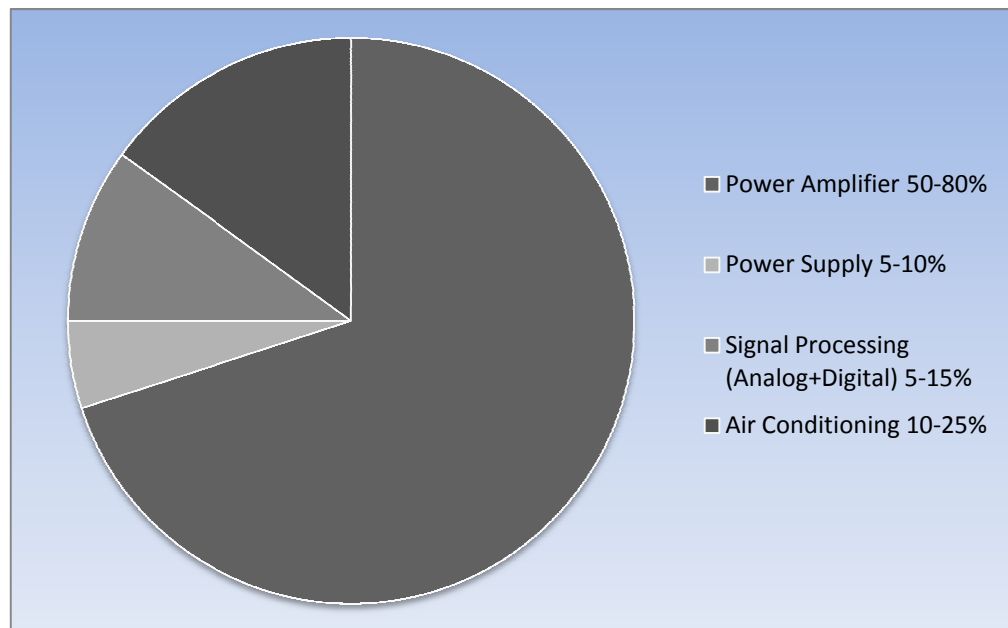


**Figure 1-3:** Radio base station energy consumption [1.7].

Modern, emerging mobile radio systems such as Wideband Code Division Multiple Access (WCDMA), High Speed Packet Access (HSPA), 3GPP Long-Term Evolution (LTE), and Mobile Worldwide Interoperability for Microwave Access (WiMAX), which all require radio transceivers able to support high data rates and throughput, have strong linearity requirements [1.8]-[1.11]. A lot of challenges for researchers and transmitter-design engineers in Vendor Companies have been introduced by utilizing high-capacity modulation schemas and multiple access techniques in transmitter design. The biggest problem during the transmitter design is PA. The high linearity of PA, high output power and high power efficiency are conflicting requirements. One can see from Figure 1-4 that the PA must operate in a near saturation region to satisfy the exacting requirements on spectrum and power efficiency [1.12]-[1.14]. However, the PA that amplifies the wideband signals with high peak to average power ratio (PAPR) produces high distortion level in that region. Aiming at solving the efficiency-linearity dilemma, one of the main trends in the design of wireless transmitters remains to provide enhanced transmitter functionalities utilising digital signal processing (DSP).

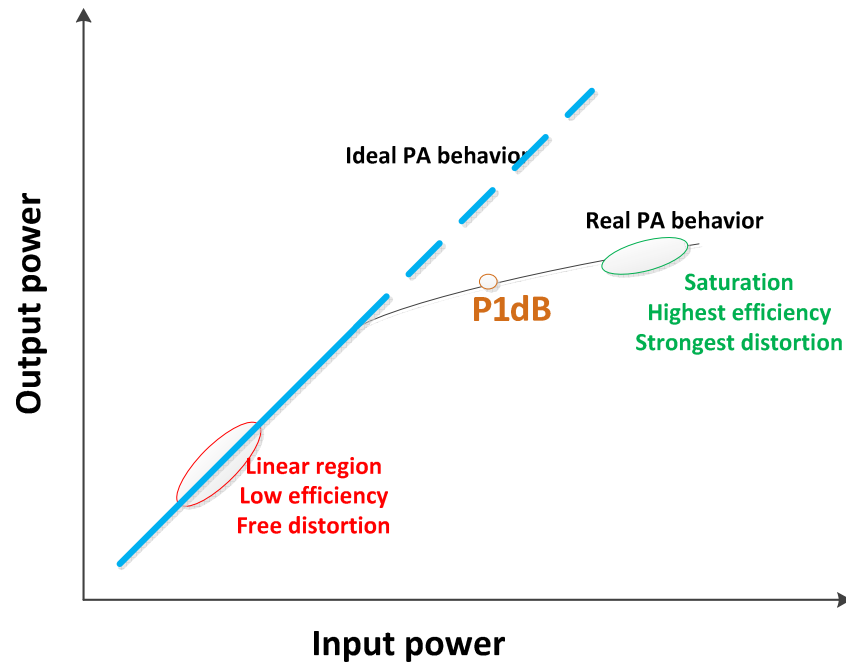


**Figure 1-4:** The transfer characteristics of an ideal and a real power amplifier

## 1.1. Overview of Recent Research

Current state-of-the-art linearisation techniques include feed-forward [1.15], RF feedback [1.16], and RF-based predistortion [1.17]; amongst them digital predistortion (DPD) implemented into DSP is the most cost effective method [1.18]-[1.23]. Functional block diagram of digital predistorter is shown in Figure 1-5. The DPD linearisation techniques for different wireless transmitters will be described in detail in Chapter 3. These techniques minimise the output distortion and reduce spectrum regrowth, and at the same time maximise power efficiency by digitally pre-processing the input signal in order to achieve a highly linear overall transfer function. However, current DPD solutions have a high computational complexity of predistorter design as well as high complexity and numerical instability of DPD model identification. These problems can be mitigated by employing novel advanced signal processing techniques based on injections of distortion products in the baseband block. The proposed approaches applied in adaptive 4G single input single output (SISO) and concurrent dual-band transmitters notably improve output signal quality and reduce high DSP computational complexity of DPD, which is the main problem of the state-of-the-art DPD solutions. Moreover, the proposed solutions for modern wireless transmitters have

many additional advantages in comparison with previously reported DPDs. These advantages will be discussed in detail in this PhD thesis.

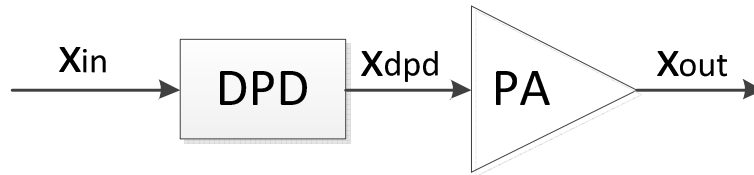


**Figure 1-5:** Functional block diagram of digital predistortion for power amplifiers

## 1.2. Aims and Objectives of the Research

The main goal is to develop the DPD technique which can deal with PA nonlinear distortion in modern wireless transmitters such as 4G SISO and multiband transmitters. In addition to PA nonlinear distortion, multiband and multi-branch MIMO transmitters have other side effects that researchers/engineers should be aware of. Cross-modulation (CM) as a most dangerous problem specific to multiband (multi-frequency MIMO) and nonlinear crosstalk specific to multi-branch MIMO transmitters will be investigated in detail. The entire PhD project is comprised of two major parts: to develop adaptive and low-complexity DPD technique for 4G SISO transmitters and to extend current DPD theory to be applicable in multiband wireless transmitters. These goals will be achieved by analysing existing solutions, studying phenomena that limit their functioning and developing methods to overcome them. Accomplishing these goals will result in improving the in-band and out-of-band performances of transmitting signals with significantly lower complexity of DPD.

### 1.2.1. Aims

This thesis has the following aims:

- Distortion analysis and behavioural modelling of power amplifiers in modern wireless transmitters such as 4G SISO, multi-frequency and multi-branch MIMO transmitters

- Theoretical development of novel adaptive DPD solution for 4G SISO transmitters
- Practical implementation and experimental validation of the proposed digital predistortion method using 4G signal and real power amplifier.
- Theoretical development of the new DPD theory for concurrent dual-band transmitter
- Practical implementation of the new digital predistortion method for concurrent dual-band wireless transmitters and its validation on experimentally emulated concurrent dual-band transmitter's test-bed.

### 1.2.2. Objectives

The individual research objectives to achieve these aims can be summarised as follows:

1. Investigation of several approaches for behavioural modelling of RF power amplifiers for the development of digital predistortion systems
2. Investigation of different adaptation methods to find the best compromise between accuracy and complexity for overcoming degradation in linearity of PA caused by variations in environmental conditions
3. Providing a comparative overview of existing digital predistortion techniques
4. Detailed investigation of digital predistortion based on baseband injection of distortion components
5. Providing a literature overview of recent advancements in the area of concurrent dual-band DPD and revealing the unresolved problems in this field.
6. Setting up the experimental test-bed for developing as well as testing new predistortion methods. Setup contains two real power amplifiers such as Mini Circuits ZFL-500 and CFH 2162-P3, Agilent ESG-D Series Signal Generator E4433B, Agilent MXG Vector Signal Generator N5182A, Agilent VSA Series Transmitter Tester and finally, MATLAB, ADS, Agilent Signal Studio Toolkit,

Agilent Distortion Suite 89604 and Agilent VSA 89601 Software as software tools

7. Creating LAN and GPIB connections between PC and instruments: ESG E4433B, MXG N5182A and VSA Series Transmitter Tester for faster offline and online data processing and developing of adaptive system that require all components of experimental test bed to be connected
8. Studying the nonlinear analysis of different power amplifiers and applying models for distortion behaviour analytical prediction in different types of wireless transmitters
9. Developing of new adaptive nonlinearity compensation technique for 4G wireless transmitters with online prediction of the PA distortion behaviour and calculating the predistorter parameters
10. Experimental verification of this technique
11. Developing baseband injection methodology applicable for concurrent dual-band transmitters
12. Theoretical derivation of the fundamental frequency model for concurrent dual-band transmitters
13. Studying the impact of each IM and CM distortion components by means of baseband simulation analysis
14. Developing of the new DPD using the simultaneous injection of IMs and CMs based on derived fundamental frequency model
15. Experimental validation of this DPD
16. Investigating computational complexity and linearising performances of the proposed DPD technique
17. Studying memory effects of power amplifiers, their influence on distortion as well as their influence on the performances of digital predistortion
18. Quantifying PA memory effects by concurrent two-tone test
19. Studying distortion compensation limit phenomena in concurrent dual-band transmitters and proposal for overcoming this phenomena

20. Experimental verification of complete linearity enhancement architecture using different signal sets and highly nonlinear PA exhibits memory effects
21. Comparative review of this work with recent works on concurrent dual-band wireless transmitters

### **1.3. Outline of the Thesis**

Recent expansion of wireless and mobile technologies with high data rates imposes more stringent requirements on electronic devices. High linearity of wireless transmitters is a key goal in order to provide users with required quality and range of services. As it was mentioned previously, efficiency and linearity of wireless transmitters are mutually exclusive characteristics. The common way of dealing with this is to enhance the efficiency at the price of linearity and to provide linearisation by an external unit. Therefore, linearisation of different types of wireless transmitters has become one of the main concerns for the design of high-speed wireless communication systems. This research work focuses on the topic of linearising modern wireless transmitters such as 4G SISO and concurrent dual-band transmitters by injection-based DPD methods implemented using DSP, which are cost effective, easily integrated and highly efficient. The thesis presents the work carried out over the period of three years aimed at contributing to the development of 4G and beyond-4G mobile wireless technologies.

Chapter 2 covers the system parameters of RF PA as well as PA memory effects and evaluation of PA behavioural modelling. The main signal quality metrics to quantify in-band and out-of-band signal performances are also presented. Orthogonal frequency division multiplex (OFDM) as a basis of next generation wireless communications systems is explained. Some of the features of 4G LTE important for the thesis topic are reviewed. Also, other effects that cause distortion such as crosstalk specific to multi-branch MIMO transmitters as well as cross-modulation specific to multi-frequency MIMO transmitters are introduced and discussed.

Chapter 3 presents a comparative overview of existing DPD linearisation techniques including the LUT-based DPD, Volterra-based DPD, memory polynomial

DPD and DPD based on artificial neural networks (ANN). The theoretical concept, main advantages and drawbacks of each DPD are presented and discussed. The most commonly used DPD extraction architectures such as direct learning architecture (DLA) and indirect learning architecture (ILA) are depicted in the Chapter. The extensions of DPD approaches to be applicable in multi-branch and multi-frequency MIMO transmitters are depicted also. The recent developments and existing problems in the area of DPD linearisation have been highlighted.

Chapter 4 overviews state-of-the-art linearisation techniques based on injection of distortion products. The main focus of the Chapter is on digitally implemented baseband injection-based techniques, especially on technique based on IM3 and IM5 injections as well as technique based on iterative injection approach. The injection-based methodology is a basis of the original developments of the thesis presented in Chapter 5, 6 and 7.

The adaptive, low-complexity DPD for 4G SISO wireless transmitters is introduced in Chapter 5. The PA linearisation is demonstrated by means of this DPD based on iterative injection of the in-band distortion components. This method has three important advantages. First, it uses real multiplications and real additions only and avoids complex Volterra, LUT or polynomials for nonlinearity compensation. Second, in contrast with existing injection-based DPD, the technique uses adaptive architecture, and therefore, is adaptive to the variation of PA nonlinear transfer function in real environmental conditions. The nonlinear PA model extraction method based on AM/AM least-squares polynomial regression approximation is explained and used in experiments. Third, the proposed DPD is verified experimentally using more than 10 dB peak-to-average power ratio (PAPR) 5-MHz downlink Long Term Evolution (LTE) signal. This is the first time that one injection-based technique is experimentally verified using a high PAPR signal such as real LTE signal. Also, this is the first adaptive, injection-based DPD.

Chapter 6 presents the proposed memoryless digital predistortion technique for concurrent dual-band transmitters based on simultaneous injection of IM and CM distortion components. The theoretical concept of the proposed DPD technique and verification of its feasibility and linearising performances by experiments are presented

in this Chapter. It has been demonstrated the linearisation of low-power ZFL-500 PA in experimentally emulated concurrent dual-band transmitter using this new 2-D DPD. The mathematical model of the proposed technique is derived for fifth-order polynomial. The PA nonlinear characterisation in single band and concurrent dual-band transmitter mode is described and discussed. The advantage of the proposed approach is its simplicity in comparison with state-of-the-art. Furthermore, the performances of the proposed DPD architecture do not depend on frequency separation between bands in concurrent dual-band transmitter.

In Chapter 7, the proposed technique described in Chapter 6 is further extended and new advancements are introduced. The technique is further generalised to any degree of nonlinearity. Also, an initial injection approach presented in Chapter 6 is extended to generalised iterative injection approach in Chapter 7, which is used to overcome distortion compensation limit phenomena in concurrent dual-band wireless transmitters caused by initial injection. In other words, the proposed approach is based on simultaneous iterative injection of the in-band IM and CM products. Moreover, in comparison with memoryless ZFL-500 PA, it is shown in experiments that CFH 2162-P3 PA exhibits memory effects that degrade the performances of the proposed DPD at the output of concurrent dual-band transmitter. The CFH 2162-P3 PA nonlinear characterisation in single band and concurrent dual-band mode are presented. The presence of memory effects are detected by concurrent two-tone test, which is also described in this Chapter. These memory effects are minimised in frequency domain by using baseband symbol adjustable normalised inverse  $S_{21}$ -parameter parallel multiplication. As it will be described, this procedure is done separately for both bands of concurrent dual-band transmitter. The experiments are done using different signal sets (LTE 1.4 MHz, LTE 3 MHz and LTE 5 MHz at 880 MHz and WCDMA at 2.14 GHz). To sum up, this Chapter brings theoretical background and experimental verification of the complete DPD system named “A Generalised Linearity Enhancement Architecture for Concurrent Dual-band Transmitters”. Numerous advantages of the proposed DPD in comparisons with previously reported concurrent dual-band DPDs are discussed in detail.

Chapter 8 presents the overall conclusions of the research work, including the thesis summary, original contributions to knowledge followed by the potential directions for the future work.

## 1.4. References

- [1.1] A. Marincic and D. Budimir, "Tesla's contribution to radiowave propagation," *Microw. Review*, vol. 7, no. 2. pp. 24-28, 2001.
- [1.2] C. E. Shannon, "A Mathematical Theory of Communication," *Bell System Tech. Journal*, vol. 27, pp. 379–423 and 623–656, Jul. and Oct. 1948.
- [1.3] "Cisco Visual Networking Index: Global Mobile Data Traffic Forecast Update 2012-2017," in White Paper, CISCO, Feb. 2013. Available Online:  
[http://www.cisco.com/en/US/solutions/collateral/ns341/ns525/ns537/ns705/ns827/white\\_paper\\_c11-520862.html](http://www.cisco.com/en/US/solutions/collateral/ns341/ns525/ns537/ns705/ns827/white_paper_c11-520862.html)
- [1.4] "Energy-saving solutions helping mobile operators meet commercial and sustainability goals worldwide," Ericsson App. Note, 2008. Available online:  
[http://www.ericsson.com/res/thecompany/docs/corpinfo/energy\\_efficiency.pdf](http://www.ericsson.com/res/thecompany/docs/corpinfo/energy_efficiency.pdf)
- [1.5] Haiying Cao "Linearization of High Efficiency Transmitters for wireless Communications," PhD thesis, Chalmers University of Technology, 2009.
- [1.6] "Gartner estimates ICT industry accounts for 2 percent of global CO2 emissions," *Gartner*, 2007. Available Online:  
<http://www.gartner.com/it/page.jsp?id=503867>
- [1.7] "Study on energy efficient radio access network (EERAN) Technologies," *Project Report, Technical University of Dresden*, 2009.
- [1.8] 3GPP technical specification, TS 36.100. Available Online:  
[http://www.3gpp.org/ftp/Specs/latest/Rel-8/36\\_series/](http://www.3gpp.org/ftp/Specs/latest/Rel-8/36_series/)
- [1.9] 3GPP technical specification, TS 36.200. Available Online:  
[http://www.3gpp.org/ftp/Specs/latest/Rel-8/36\\_series/](http://www.3gpp.org/ftp/Specs/latest/Rel-8/36_series/)

- [1.10] 3GPP technical specification, TS 36.500. Available Online:  
[http://www.3gpp.org/ftp/Specs/latest/Rel-8/36\\_series/](http://www.3gpp.org/ftp/Specs/latest/Rel-8/36_series/)
- [1.11] 3GPP technical specification, TS 36.104 V8.4.0. Available Online:  
[http://www.3gpp.org/ftp/Specs/latest/Rel-8/36\\_series/](http://www.3gpp.org/ftp/Specs/latest/Rel-8/36_series/)
- [1.12] M. Modeste, D. Budimir, M.R Moazzam, and C.S. Aitchison, "Analysis and practical performance of a difference frequency technique for improving the multicarrier IMD performance of RF amplifiers," *1999 IEEE MTT-S Symp. on Technologies for Wireless Applications*, pp.53-56, Feb. 1999.
- [1.13] F. H. Raab, P. Asbeck, S. Cripps, P. B. Kenington, Z. B. Popovic, N. Pothecary, J. F. Sevic, and N. O. Sokal, "Power Amplifiers and Transmitters for RF and Microwave," *IEEE Trans. Microw. Theory Tech.*, vol. 50, no. 3, pp. 814-826, March 2002.
- [1.14] P. B. Kenington, "*High Linearity RF Amplifier Design*," Artech House, 2000.
- [1.15] S. P. Stapleton, "Adaptive feedforward linearization for RF power amplifiers," in *Proc. 55th Automatic RF Tech. Group Conf. Dig.-Spring*, vol. 37, pp. 1-7, June 2000.
- [1.16] Y. Y. Woo, J. Kim, J. Yi, S. Hong, I. Kim, J. Moon, and B. Kim, "Adaptive digital feedback predistortion technique for linearizing power amplifiers," *IEEE Trans. Microw. Theory Tech.*, vol. 55, no. 5, pp. 932-940, May 2007.
- [1.17] S. P. Stapleton and F. C. Costescu, "An adaptive predistorter for a power amplifier based on adjacent channel emission," *IEEE Trans. Microw. Theory Tech.*, vol. 41, no. 1, pp. 49-56, Feb. 1992.
- [1.18] S. Hong, Y. Y. Woo, J. Kim, I. Kim, J. Cha, I. Kim, J. Moon, J. Yi, and B. Kim, "Weighted polynomial digital predistortion for low memory effect Doherty power amplifier," *IEEE Trans. Microw. Theory Tech.*, vol. 55, no. 5, pp. 925-931, May 2007.

- [1.19] J. Sirois, S. Boumaiza, M. Helaoui, G. Brassard, and F. M. Ghannouchi, "A robust modeling and design approach for dynamically loaded and digitally linearized Doherty amplifiers," *IEEE Trans. Microw. Theory Tech.*, vol. 53, no. 9, pp. 2875-2883, Sep. 2005.
- [1.20] P. L. Gilabert, A. Cesari, G. Montoro, E. Bertran, and J. M. Dilhas, "Multi-lookup table FPGA implementation of an adaptive digital predistorter for linearizing RF power amplifiers with memory effects," *IEEE Trans. Microw. Theory Tech.*, vol. 56, no. 2, pp. 372-384, Feb. 2008.
- [1.21] C. Eun and E. J. Powers, "A new Volterra predistorter based on the indirect learning architecture," *IEEE Trans. Signal Process.*, vol. 45, no. 1, pp. 223–227, Jan. 1997.
- [1.22] S.-C. Jung, O. Hammi, and F. M. Ghannouchi, "Design optimization and DPD linearization of GaN-based unsymmetrical Doherty power amplifiers for 3G multicarrier applications," *IEEE Trans. Microw. Theory Tech.*, vol. 57, no. 9, pp. 2105–2113, Sept. 2009.
- [1.23] A. S. Tehrani "Behavioral modeling of wireless transmitters for distortion mitigation", PhD thesis, Chalmers University of Technology, 2012.

## 2. Nonlinear Distortion in Power Amplifiers for Wireless Transmitters

### 2.1. Introduction

This Chapter describes the main system parameters of wireless transmitters specific for the transmitter's most challenging block such as PA. The main signal quality parameters and the PA modelling metrics in time and frequency domain are overviewed in this Chapter. Moreover, OFDM as a basis of modern wireless communications and 4G LTE technology are briefly presented because the PA nonlinear behaviour problems are much more noticeable in 4G in comparison with previous generations. This Chapter also introduces next-generation wireless transmitters such as multi-branch and multi-frequency MIMO transmitters. The Crosstalk and Cross-modulation are transmitter design problems specific for these wireless transmitter types. These problems and their impacts on the output signal degradation are explained in this Chapter.

### 2.2. PA System Parameters

The following subsections bring the definitions of the main PA system parameters [2.1], [2.2].

#### 2.2.1. Gain

The gain of a PA is the ratio of the output power to the input power. It is usually expressed in decibels (dB) with the following relation:

$$G(\text{dB}) = 10 \log \frac{P_{out}}{P_{in}} \quad (2.1)$$

where  $P_{in}$  is the input power and  $P_{out}$  is the output power.

### 2.2.2. Bandwidth

The bandwidth of the power amplifier is the range of frequencies for which the power amplifier delivers acceptable performance. Typically, the bandwidth is defined as the difference between the lower and upper half power points and is also called 3-dB bandwidth (Figure 2-1).

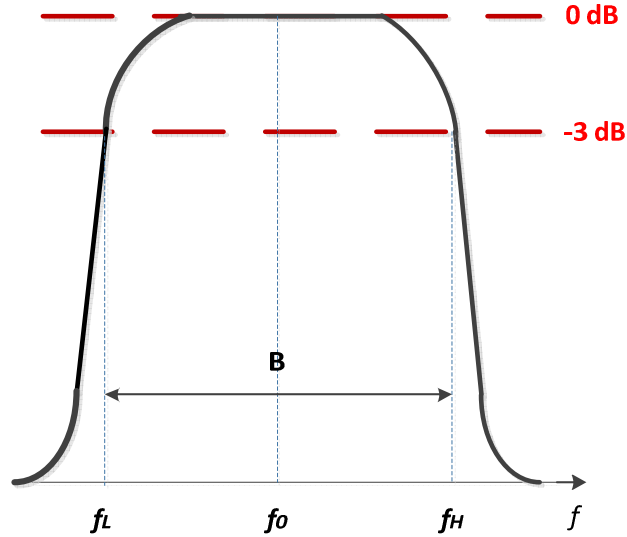


**Figure 2-1:** 3-dB bandwidth of the PA

### 2.2.3. Power efficiency

Power efficiency is the metric to quantify the ability of a system to transform the given input power to useful output power. The most power-consuming component of a wireless transmitter is the PA. Therefore, the PA is dominant component in determining the overall power efficiency of a wireless transmitter. There are three different definitions of power amplifier efficiency in literature, which are total efficiency, drain efficiency, and power added efficiency [2.1].

**Total efficiency** is defined as  $\eta_t = \frac{P_{out}}{P_{dc} + P_{in}}$ , where  $\eta_t$  is the total efficiency of the PA,  $P_{dc}$ ,  $P_{in}$  and  $P_{out}$  are the DC and RF powers at the input and output of the PA, respectively.

**Drain efficiency** is defined as  $\eta_D = \frac{P_{RF\ Drain}}{P_{dc\ Drain}}$ , where  $P_{dc\ Drain}$  and  $P_{RF\ Drain}$  are the DC and RF powers at the drain level of the transistor.

**Power added efficiency** is defined as  $\eta_{PAE} = \frac{P_{out} - P_{in}}{P_{dc}}$ , where  $\eta_{PAE}$  is the total power added efficiency of the PA,  $P_{dc}$ ,  $P_{in}$  and  $P_{out}$  are the DC and RF powers at the input and output of the PA, respectively.

#### 2.2.4. P1dB Compression Point

The typical PA input-output and gain characteristics are shown in Figure 2-2. The 1dB compression point (P1dB) is a measure of PA linearity. The gain of an amplifier compresses when the output signal level enters the compression region before it reaches saturation. Higher output power corresponds to a higher compression point. It is an input (or output) power for which the gain of the PA is 1 dB less than the small-signal gain (ideal linear gain).

The maximum saturation point corresponds to the point where the PA reaches its maximum output power. This maximum power is called the saturation power  $P_{sat[max]}$ . The 3 dB saturation power  $P_{sat[dB]}$  corresponds to the power for which the gain of the PA is 3 dB less than the small-signal gain.

#### 2.2.5. Third Order Intercept Point (IP3)

Figure 2-3 brings graphical derivation of second and third order intercept points. The third order intercept point (IP3) is a widely used metric in PAs, which gives information about the linearity of an amplifier. A higher IP3 means better linearity and lower distortion generation. It is the theoretical point at which the desired output signal and undesired third-order IM signal are equal in levels considering an ideal linear gain for the PA. The theoretical input point is the input IP3 (IIP3) and the output point is the output IP3 (OIP3).

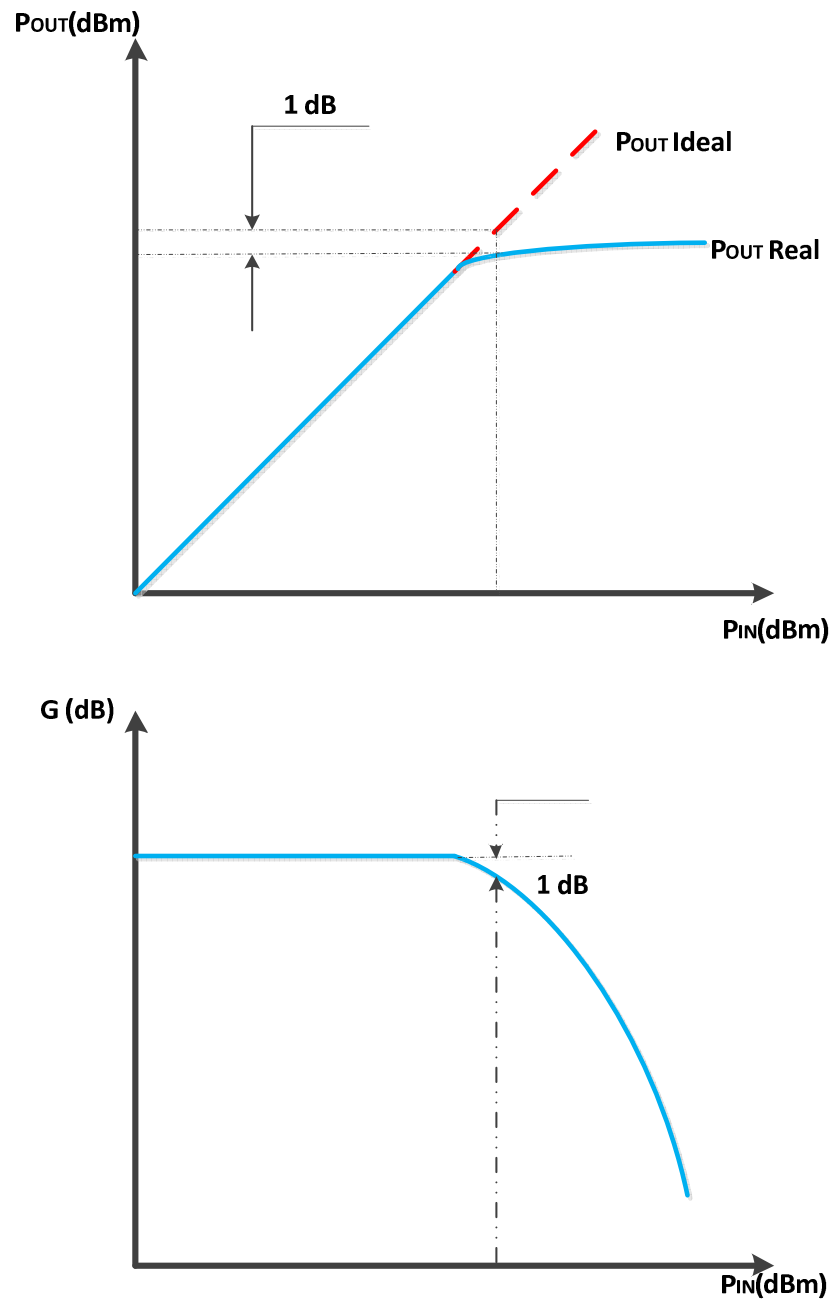


**Figure 2-2:** The input-output and gain characteristics of a PA

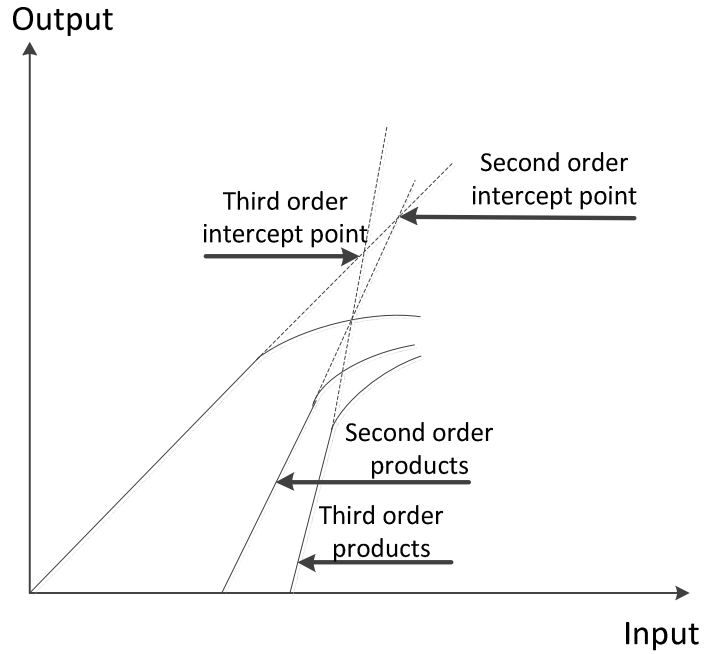


**Figure 2-3:** The second and third order intercept points

### 2.2.6. Power Back-off

The power back-off is defined as the ratio between the PA's saturation power to the RF signal's mean power. There are three types of power back-off: input back-off, output back-off and peak back-off [2.1], [2.2]. The back-off at the input of the PA (*IBO*) is obtained by:

$$IBO(dB) = P_{i,sat} - P_{i,mean} \quad (2.2)$$

where  $P_{i,sat}$  and  $P_{i,mean}$  are the saturation power and mean signal power at the input of the PA, respectively. Similarly, the back-off at the output of the PA (*OBO*) is given by:

$$OBO(dB) = P_{o,sat} - P_{o,mean} \quad (2.3)$$

where  $P_{o,sat}$  and  $P_{o,mean}$  are the saturation power and mean signal power at the output of the PA, respectively.

Finally, the Peak Back-Off (*PBO*) is given as follows:

$$PBO(dB) = P_{o,sat} - P_{o,peak} \quad (2.4)$$

This is the ratio of saturated output power ( $P_{o,sat}$ ) to peak output power ( $P_{o,peak}$ ). It should be noted that an increase of the back-off increases the linearity of the PA and vice versa.

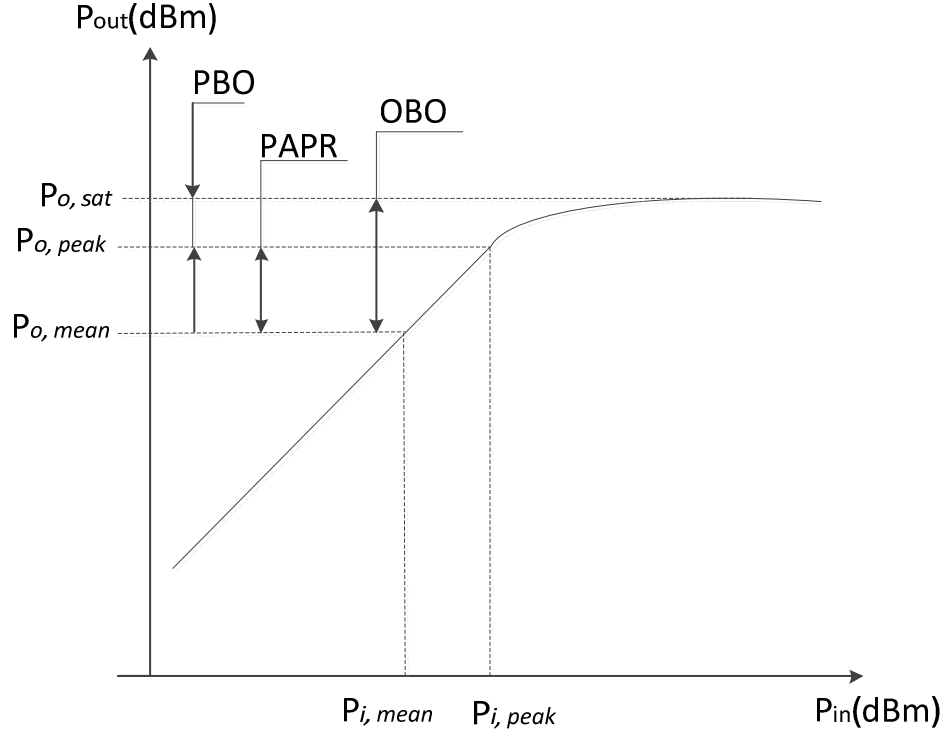


**Figure 2-4:** The output back-off, peak back-off and peak-to-average power ratio for power amplifiers

### 2.2.7. Peak to Average Power Ratio (PAPR)

A very important signal parameter in terms of linearity is signal's peak-to-average power ratio (PAPR), which is the ratio between the peak power  $P_{peak}$  (related to peak amplitude) and the average power  $P_{mean}$  (related to mean amplitude) of a signal. It is also called the crest factor and is given by [2.1]:

$$PAPR(dB) = 10 \log \left( \frac{\max(|x(t)|^2)}{\text{mean}(|x(t)|^2)} \right) = 10 \log \left( \frac{P_{peak}}{P_{mean}} \right) \quad (2.5)$$

As shown in Figure 2-4, when the power is logarithmically transformed in dBm, the PAPR is the difference between signal peak and average powers.

## 2.3. Memory Effects

Memory effects can be explained as time lags between amplitude (AM/AM) and phase (AM/PM) responses of PA [2.1]. Electrical and thermal are two types of memory effects. The electrical memory effects are dominant in wideband systems and they are produced by poor gate and drain decoupling in FET and base and collector decoupling in BJT. Also, they are generated by non-constant, frequency-dependent envelope impedances within frequency bands of interest. The time response of power amplifiers with memory depends not only on the instantaneous input signal, but on the previous inputs as well. These memory effects result in the frequency-dependent gain and phase shifts of the signal passing through the PA. Consequently, the memory effects cause distortion of the output signal and result in IMD asymmetry. The presence of memory effects also degrades the performances of DPD.

The two-tone measurement was proposed in [2.3] and widely used to evaluate PA memory effects [2.4]-[2.6]. The amplitudes of lower and upper intermodulation distortion were measured. The PA that exhibits memory effects causes an imbalance between lower and upper IM3, lower and upper IM5, etc. Typical IMD characteristics of the highly nonlinear, high-power PA with memory effects are shown in Figure 2-5.

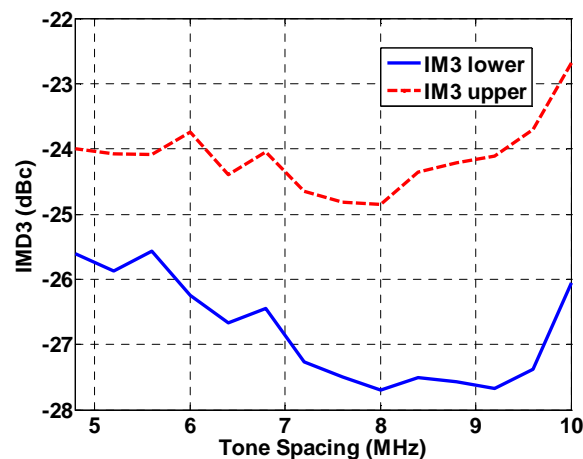


**Figure 2-5:** Typical IMD characteristics of the PA with memory effects evaluated using two-tone tests with different tone spacing

In this thesis, the PA memory effects in much more complex, concurrent dual-band transmitters are evaluated and compensated. This will be described in detail in Chapter 7.

## 2.4. Signal Quality Parameters

### 2.4.1. Spectrum Regrowth

The spectrum regrowth is the energy from the modulated signal that spreads into adjacent channels due to the PA nonlinearity. It can be defined at different offset frequencies from the operational carrier frequency and is measured in decibels relative to the carrier (dBc). Typically, the spectrum regrowth is measured at the offset frequency from the carrier equal to the half of modulated signal bandwidth, or sometimes 1.5 times the half of signal bandwidth. The spectrum regrowth improvements at the output of PA at lower and upper adjacent bands are graphically demonstrated in Figure 2-6.

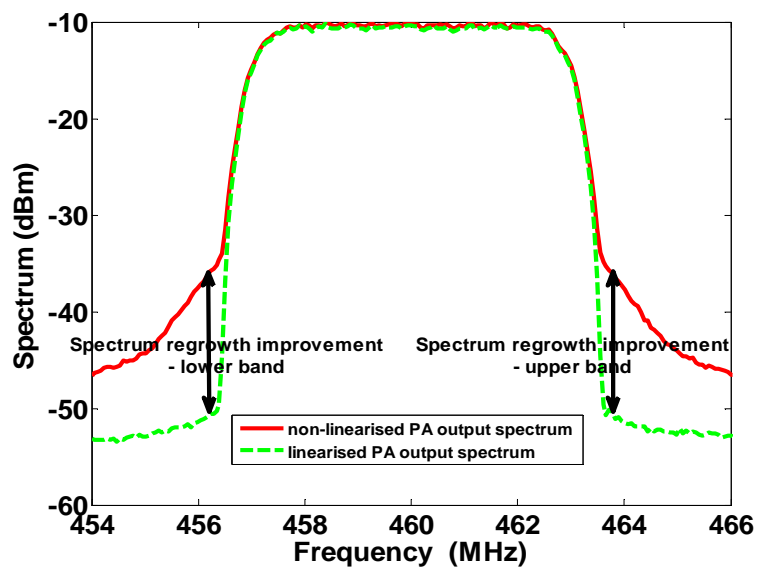


**Figure 2-6:** Improvements in spectrum regrowth in lower and upper adjacent channels

### 2.4.2. Adjacent Channel Power Ratio (ACPR)

The adjacent channel power ratio (ACPR) is one of the main figures of merit in the evaluation of IM distortion performance of RF PAs. It is a measure of spectrum regrowth that appears at the signal adjacent bands. ACPR is defined as the ratio of power in a bandwidth adjacent to the main channel to the power within the main signal

bandwidth. The ACPR for the right side of the power spectrum density (PSD) can be defined as [2.1]:

$$ACPR(right) = \frac{\int_{f_c + \Delta f - \frac{B}{2}}^{f_c + \Delta f + \frac{B}{2}} PSD(f) df}{\int_{f_c - \frac{B}{2}}^{f_c + \frac{B}{2}} PSD(f) df} \quad (2.6)$$

Similarly, the ACPR for the left side of the PSD can be obtained as:

$$ACPR(left) = \frac{\int_{f_c - \Delta f - \frac{B}{2}}^{f_c - \Delta f + \frac{B}{2}} PSD(f) df}{\int_{f_c - \frac{B}{2}}^{f_c + \frac{B}{2}} PSD(f) df} \quad (2.7)$$

where  $f_c$  is the carrier frequency,  $B$  is the bandwidth of the modulated signal, and  $PSD(f)$  is the power spectrum density at frequency  $f$ .

### 2.4.3. Error Vector Magnitude (EVM)

The in-band signal quality can be analysed based on its error vector magnitude (EVM) measurement in time domain. The EVM is a common metric for the fidelity of the constellation of information symbols. This is a measure of how far the actual (measured) points are from the ideal locations [2.1]. In other words, the EVM is the ratio of the power of the error vector to the power of the reference vector related to the ideal constellation. The EVM can be defined in decibels (dB):

$$\begin{aligned} EVM(dB) &= 10 \log_{10} \left( \frac{P_{error}}{P_{ideal}} \right) \\ &= 10 \log_{10} \left( \text{mean} \left( \frac{(I_{actual} - I_{ideal})^2 + (Q_{actual} - Q_{ideal})^2}{I_{ideal}^2 + Q_{ideal}^2} \right) \right) \end{aligned} \quad (2.8)$$

or in percentage (%):

$$EVM(\%) = \sqrt{\frac{P_{error}}{P_{ideal}}} * 100\% \quad (2.9)$$

where  $P_{error}$  and  $P_{ideal}$  are the power of the error vector and highest power point in the reference signal constellation,  $I_{ideal}$  and  $Q_{ideal}$  are the ideal in-phase and quadrature signals, and  $I_{actual}$  and  $Q_{actual}$  are the transmitted in-phase and quadrature signals.

## 2.5. Performance Evaluation of PA Modelling

The PA behavioural modelling is one of the crucial steps in developing of DPD with satisfied linearisation performances [2.7]. For the quantitative measure of an accuracy of the PA behavioural modelling, a mean squared error (MSE), a normalised mean squared error (NMSE) and an adjacent channel error power ratio (ACEPR) are typically used [2.8]. MSE and NMSE are used as accuracy metrics in time domain, whereas ACEPR is used in frequency domain.

### 2.5.1. Mean Squared Error

The simplest metric used to assess the accuracy of the chosen PA mathematical model is MSE defined as:

$$MSE_{dB} = 10 \log_{10} \left( \frac{1}{K} \sum_{n=1}^K |y_{meas}(n) - y_{est}(n)|^2 \right) \quad (2.10)$$

where  $y_{meas}$  and  $y_{est}$  are the measured and estimated output waveforms, respectively, and  $K$  is the number of samples of the output waveform.

### 2.5.2. Normalised Mean Squared Error

The second time-domain metric is NMSE defined as:

$$NMSE_{dB} = 10 \log_{10} \left( \frac{\sum_{n=1}^K |y_{meas}(n) - y_{est}(n)|^2}{\sum_{n=1}^K |y_{meas}(n)|^2} \right) \quad (2.11)$$

where, similarly as in MSE,  $y_{meas}$  and  $y_{est}$  are the measured and estimated output waveforms, and  $K$  is the number of samples of the output waveform.

### 2.5.3. Adjacent Channel Error Power Ratio

As a measure of accuracy of PA behavioural model in frequency domain, ACEPR is widely used. It can be defined as maximum of both lower and upper band ACEPR:

$$ACEPR = \max_{m=1,2} \left[ \frac{\int_{(adj)m} |Y_{meas}(f) - Y_{est}(f)|^2}{\int_{ch} |Y_{meas}(f)|^2} \right] \quad (2.12)$$

or as an average ACEPR:

$$ACEPR = \frac{1}{2} \left( \frac{\int |E(f)|^2 df_{lower adj ch} + \int |E(f)|^2 df_{upper adj ch}}{\int |Y_{meas}(f)|^2 df_{ch}} \right) \quad (2.13)$$

where  $Y_{meas}(f)$ ,  $Y_{est}(f)$  and  $E(f)$  are the discrete Fourier transforms of  $y_{meas}$ ,  $y_{est}$  and the error signal  $e(n)$ , defined as

$$e(n) = y_{meas}(n) - y_{est}(n). \quad (2.14)$$

## 2.6. OFDM Modulation System

Orthogonal frequency-division multiplexing (OFDM) is a basis of modern wireless communications. Using OFDM based signals, which have high PAPR, brings a lot of challenges for researchers and engineers. This is mainly because the PA that amplifies such high PAPR signals causes very high distortion level at the output of transmitter.

OFDM is realised using spectrum overlapping concept, where each substream is transmitted through a separated subcarrier [2.1], [2.9]. Substreams are orthogonal and they can be separated in demodulator. OFDM is implemented using an inverse fast Fourier transformation (IFFT) on transmitter side and FFT on receiver side. It also contains a cyclic prefix. OFDM is basically a multicarrier modulation technique. The centre frequencies of the overlapping channels are:

$$f_n = f_c + i\Delta f, \quad i = 0, \dots, N - 1 \quad (2.15)$$

where  $f_c$  is carrier frequency. The data rate for each substream is  $N$  times lower than the data rate of initial stream. The modulated signal related to all subcarriers is presented as:

$$s(t) = \sum_{i=0}^{N-1} s_i g(t) e^{j2\pi i \Delta f t} e^{j(2\pi f_c t + \varphi_i)} \quad (2.16)$$

where  $g(t)$  is the pulse-shaping filter,  $s_i$  is the complex symbol associated with  $i$ th subcarrier,  $\varphi_i$  is the phase of the  $i$ th subcarrier and  $\Delta f = 1/T_N$ . The subcarriers  $e^{j(2\pi(f_c + i\Delta f)t + \varphi_i)}$  provide a set of orthogonal basis functions over the OFDM symbol interval  $T_N$ .

OFDM implementation using IFFT and FFT is shown in Figure 2-7. The input data is first de-multiplexed into  $N$  parallel substreams. Each substream is then mapped to a real or complex symbol stream using some modulation constellation, e.g., QAM. An IFFT is computed on each set of symbols, giving a set of complex time-domain samples [2.1]. These samples are then up-converted to passband. The real and imaginary components are first converted to the analogue domain using digital-to-analogue convertors (DACs). These analogue signals are then used to modulate cosine

and sine waves at the carrier frequency  $f_c$ , respectively. Finally, these signals are summed and amplified to give the transmission signal,  $s(t)$ .

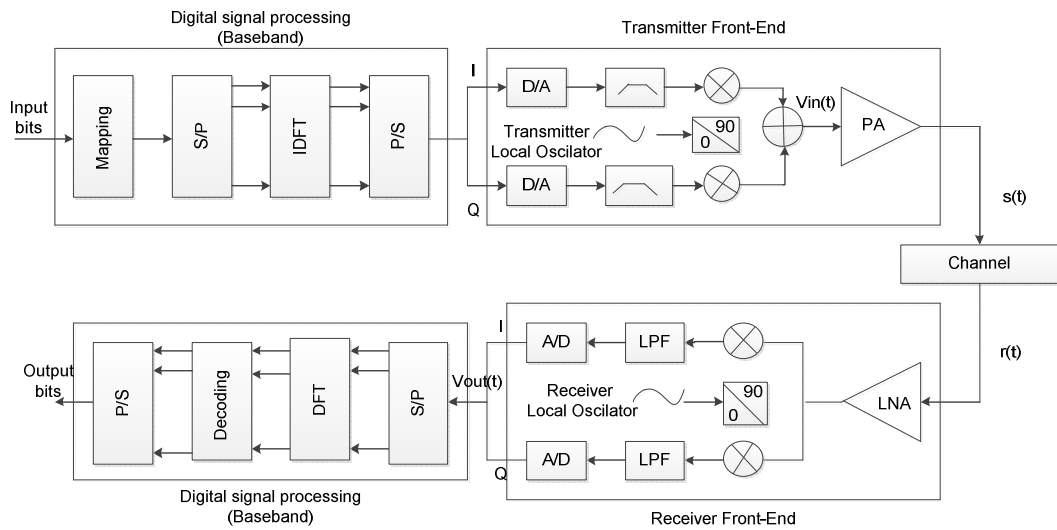


**Figure 2-7:** Block diagram of OFDM transmitter and receiver

The receiver pick up the signal  $r(t)$ , which is then down-converted to baseband using cosine and sine waves at the carrier frequency. This also creates signals centred on  $2f_c$ , so low-pass filters are used to reject these unwanted signals. The baseband signals are then sampled and digitised using analogue-to-digital convertors (ADCs). In order to convert these signals back to the frequency domain, FFT is utilised. After this FFT procedure,  $N$  parallel streams are obtained. They are converted to a binary stream using an appropriate symbol detector. These streams are then re-combined into a serial stream, which is an estimate of the transmitted information stream.

Due to the dispersive effects of the radio channel, intersymbol interference (ISI) of the adjacent OFDM symbol degrades the bit error rate (BER) performances. A cyclic extension is appended to the OFDM symbol to compensate for ISI. The cyclic prefix (CP) is typically created by copying the end of the OFDM symbol and placing that copy at the beginning of the symbol, for every symbol. The length of the CP is selected according to the impulse response of the radio channel [2.1], [2.9].

## 2.7. LTE Technology

The LTE radio transmission and reception specifications for the UE and the eNodeB RBS are documented in [2.10].

### 2.7.1. Transmission Bandwidths

LTE must support the international wireless market and regional spectrum regulations and spectrum availability. The specifications include variable signal bandwidths selectable from 1.4 to 20 MHz, with subcarrier spacing of 15 kHz. Subcarrier spacing is constant regardless of the signal bandwidth. 3GPP has defined the LTE radio interface to be adaptable to different signal bandwidths with minimum impact on system operation [2.11].

The smallest amount of resource that can be allocated in the uplink or downlink is called a resource block (RB). An RB is 180 kHz wide and lasts for one 0.5 ms timeslot. For standard LTE, a RB includes 12 subcarriers at 15 kHz spacing. Optionally, if 7.5 kHz subcarrier spacing is utilised, a RB comprises 24 subcarriers for 0.5 ms. The maximum number of RBs supported by each transmission bandwidth and the minimum total power dynamic range of different LTE signals are given in Table 2-1. The PAPR of the signal is one half of its dynamic range and directly depends on the signal bandwidth and the number of allocated resource blocks [2.12].

**TABLE 2-1:** Transmission bandwidth configuration

<b>Signal bandwidth (MHz)</b>	<b>1.4</b>	<b>3</b>	<b>5</b>	<b>10</b>	<b>15</b>	<b>20</b>
Transmission bandwidth configuration (RB)	6	15	25	50	75	100
Total power dynamic range (dB)	7.7	11.7	13.9	16.9	18.7	20

### 2.7.2. Supported Frequency Bands

The LTE specifications include all the frequency bands defined for UMTS, which is a list that continues to grow. There are 15 FDD operating bands and 8 TDD operating bands listed in Table 2-2. There is no consensus on which LTE band will first be deployed, since the answer is highly dependent on local variables. This lack of consensus is a significant complication for equipment designers and manufacturers. This is in contrast with the start of GSM and WCDMA, when both were specified for only one band. What is now established is that one may no longer assume that any particular frequency band is reserved for any radio access technology [2.11].

**TABLE 2-2: E-UTRA operating bands**

<b>E-UTRA operating band</b>	<b>Uplink (UL) operating band RBS receives UE transmits <math>F_{UL\_low} - F_{UL\_high}</math></b>	<b>Downlink (DL) operating band RBS transmits UE receives <math>F_{DL\_low} - F_{DL\_high}</math></b>	<b>Duplex mode</b>
1	1920-1980 MHz	2110-2170 MHz	FDD
2	1850-1910 MHz	1930-1990 MHz	FDD
3	1710-1785 MHz	1805-1880 MHz	FDD
4	170-1755 MHz	2110-2155 MHz	FDD
5	824-849 MHz	869-894 MHz	FDD
6	830-840 MHz	875-885 MHz	FDD
7	2500-2570 MHz	2620-2690 MHz	FDD
8	880-915 MHz	925-960 MHz	FDD
9	1749.9-1784.9 MHz	1844.9-1879.9 MHz	FDD
10	1710-1770 MHz	2110-2170 MHz	FDD
11	1427.9-1452.9 MHz	1475.9-1500.9 MHz	FDD
12	698-716 MHz	728-746 MHz	FDD
13	777-787 MHz	746-756 MHz	FDD
14	788-798 MHz	758-768 MHz	FDD
...			
17	704-716 MHz	734-746 MHz	FDD
...			
33	1900-1920 MHz	1900-1920 MHz	TDD
34	2010-2025 MHz	2010-2025 MHz	TDD
35	1850-1910 MHz	1850-1910 MHz	TDD
36	1930-1990 MHz	1930-1990 MHz	TDD
37	1910-1930 MHz	1910-1930 MHz	TDD
38	2570-2620 MHz	2570-2620 MHz	TDD
39	1880-1920 MHz	1880-1920 MHz	TDD
40	2300-2400 MHz	2300-2400 MHz	TDD

## 2.8. Multi-branch and Multi-frequency MIMO Transmitters

Multiple-input multiple-output (MIMO) is a promising technique that can improve the spectrum efficiency of wireless systems (see [2.13] and references therein). In fact, MIMO techniques can increase data rates, coverage of service area as well as communication reliability. Moving from single-input single-output (SISO) to MIMO

communication systems could theoretically multiply the capacity of the system or the system data rate by the number of outputs integrated in the MIMO transceiver. Majority of wireless systems have been reconsidered regarding the usage of MIMO. Its MIMO feature is intended for high-speed applications, and it covers both space-time codes and spatial multiplexing [2.1], [2.13]. In order to increase the data rate, MIMO is also utilised in 4G LTE standard.

The conventional definition of MIMO is that of a system with multiple inputs and multiple outputs. This definition is extended to Wireless communication topologies in which multiple modulated signals, separated in space or frequency domain, are simultaneously transmitted through a multiple/single branch radio frequency (RF) front-end [2.14].

MIMO systems, with modulated signals separated in space domain, refer to wireless topologies with multiple branches of RF front-ends, with all branches concurrently utilised in signal transmission. These types of MIMO systems are named **Multi-branch MIMO systems** [2.14].

MIMO systems, with modulated signals separated in frequency domain, refer to systems where multiple signals modulated in different carrier frequencies are simultaneously transmitted through a single branch RF front-end. These types of MIMO systems are named **Multi-frequency MIMO systems**. Typical examples of multi-frequency MIMO systems are concurrent dual-band and multi-carrier transmitters. The system in frequency domain comprises two independent baseband signals as the multiple inputs and two up-converted and amplified signals at two carrier frequencies as the multiple outputs. This type of MIMO system uses a single branch RF front-end to transmit multiple signals separated in frequency domain [2.14].

### 2.8.1. Distortion in Multi-branch MIMO Transmitters

In addition to possibly increasing the data rate without additional spectrum resources, multi-branch MIMO topology introduces numerous implementation challenges, which can be categorised into two groups. The first group are problems related to general transceiver design, such as transmitter linearity, receiver dynamic range, and imbalance and leakages in mixers, and is not specific to MIMO systems. On the transmitter side of  $2 \times 2$  multi-branch MIMO systems shown in Figure 2-8, there are two independent RF chains including PAs. As it was mentioned previously, PAs have

nonlinear characteristics in general, which leads to two major problems: one is spectrum regrowth, and the other is in-band signal distortion. The former can cause an increase of inter-channel interference, and the latter can degrade signal quality at transmitter output and therefore, bit error rate (BER) performance at the receiver side.

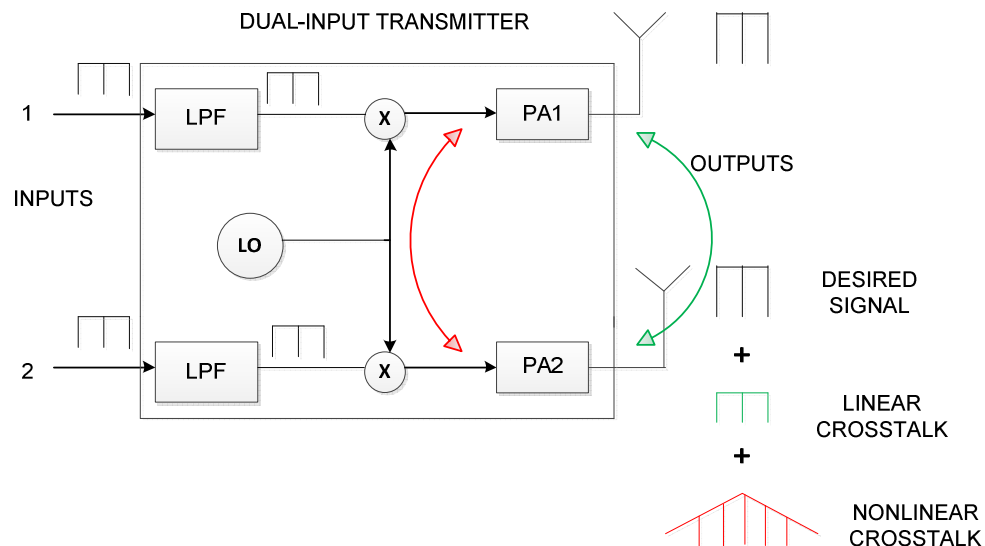


**Figure 2-8:** Dual-input wireless transmitter for 2x2 MIMO communication system

However, in order to reduce transceiver size, today's trend is to implement complete multi-branch MIMO transceiver on the same chipset. In that case, there are no independent signals' paths in multi-branch MIMO transceiver and crosstalk between them is unavoidable. This crosstalk between the multiple paths is one of the main issues. This problem belongs to the second group of problems specific to MIMO transceivers. Crosstalk or coupling effects are the result of signal interferences from two or more sources. Due to the fact that the signals in different paths use the same operating frequency and have equal transmission power, crosstalk is more likely between the paths [2.13], [2.15]. Furthermore, the crosstalk impact would be more noticeable in integrated circuit (IC) design, especially when the small size is very important. As shown in Figure 2-8, crosstalk in MIMO transceivers can be classified as linear or nonlinear. Crosstalk is considered linear when its effect at the output of the transmitter (at the antenna) can be modelled as a linear function of the interference and desired signals. In other words, the signal affected by linear crosstalk does not pass through nonlinear components. In contrast, nonlinear crosstalk affects the signal before it passes through a nonlinear component. Since the PA is the main source of nonlinearity, crosstalk that occurs in the transmitter circuit before the PA is the main

source of nonlinear crosstalk, while antenna crosstalk is considered linear. These two types of crosstalk seriously deteriorate the quality of the signal at transmitter output. In fact, they produce distortion that seriously degrades EVM metric [2.13], [2.15], [2.16]. Linear crosstalk can be easily mitigated on receiver side using matrix inversion algorithm [2.13], [2.16]. The nonlinear crosstalk is a much bigger problem and should be carefully considered during DPD design [2.13], [2.16]. If it is not taken into account, the performances of DPD can be seriously degraded.

### 2.8.2. Distortion in Multi-frequency MIMO Transmitters

The nonlinear behaviour is much more noticeable in multi-frequency MIMO systems. When considering concurrent dual-band transmitter shown in Figure 2-9, the two modulated signals at different operating frequencies are transmitted simultaneously.

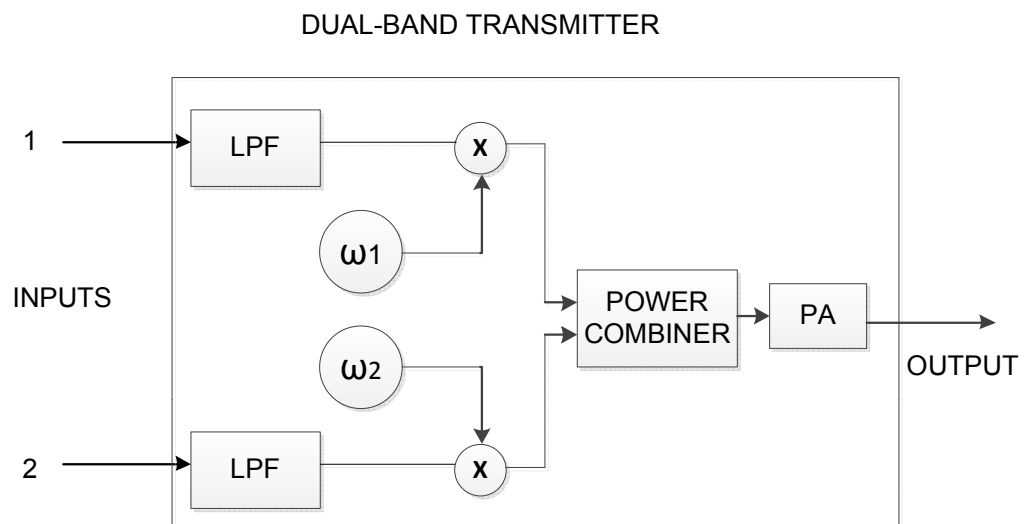


**Figure 2-9:** Block diagram of concurrent dual-band transmitter

In these concurrent dual-band transmitters, the distortion products at the transmitter output can be categorised into three major groups [2.17]. Figure 2-10 shows these three types of unwanted modulation products for a dual-band transmitter excited with a two-tone signal in each band.

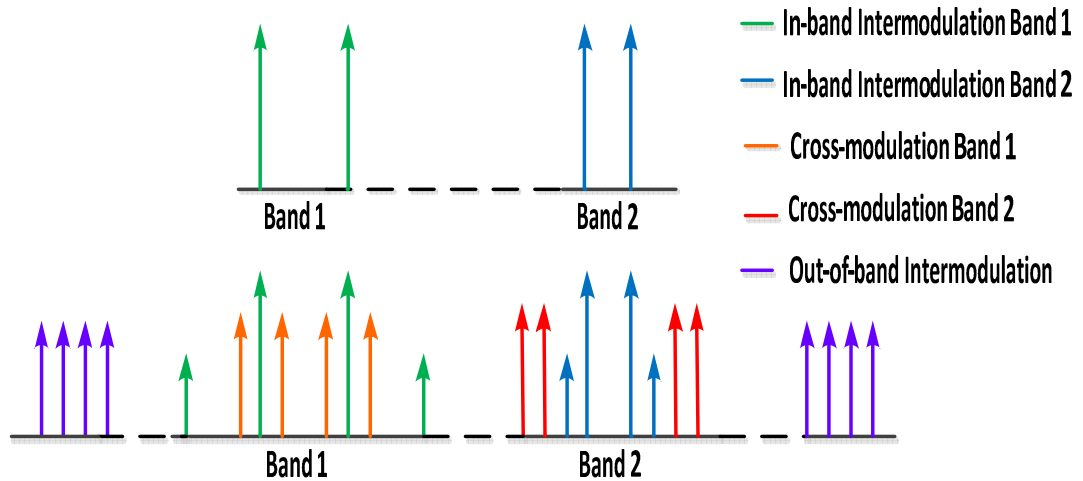


**Figure 2-10:** Power spectrum of the signal at: (a) the input and (b) output of a dual-band transmitter

The first group, dubbed in-band intermodulation, consists of the intermodulation products around each carrier frequency that are only due to the intermodulation between the tones within each band. This effect is similar to what it is case in single-band transmitters.

The second group, which includes the cross-modulation products, appears within the same frequency range as the in-band intermodulation. This distortion is the result of interaction between the signals in both frequency bands.

Finally, the last group, which is dubbed out-of-band intermodulation, is the intermodulation products between the two signals in both frequency bands. These out-of-band terms are located far away from the lower and upper frequency bands and can be easily filtered out. However, the in-band intermodulation and cross-modulations must be eliminated and compensated for.

There are problems in using conventional DPD techniques for compensation of the in-band intermodulation and cross-modulation distortion. Using a single digital predistorter to compensate for all the distortion requires capturing the whole dual-band signal spectrum at the output of the nonlinear dual-band or wideband PA. The bottleneck of this approach is the sampling rate limitation of the analogue-to-digital convertors (ADCs) and digital-to-analogue convertors (DACs), especially in case when frequency separation between bands is very large. Additionally, using two independent conventional DPDs for compensation of distortion in each carrier frequency is also not appropriate since the effect of cross-modulation products is not considered [2.17].

## 2.9. Conclusion

The fundamental parameters of power amplifier as the most challenging part of wireless transmitters, the main signal quality parameters and the main PA behavioural modelling metrics have been presented in this Chapter. In addition to this, the distortion problem in modern wireless transmitters has been described. The transmitters are characterised by their efficiency and linearity, which mostly depend on the PA mode of operation. As it has been outlined in Introduction, a PA is designed to operate in a nonlinear mode, and an additional device, usually implemented into DSP, is used for its linearisation. In order to successfully designed and implemented this device, the detailed analysis of different distortion types are becoming indispensable. It should be noted that the nonlinear distortion is significantly stronger in 4G SISO wireless transmitters because 4G signals have very high PAPR. Moreover, there are other sided negative effects such as cross-modulation and crosstalk in multi-frequency and multi-branch MIMO transmitters, respectively. Therefore, the additional distortion appears at transmitter output. If it is not taken into account, the linearisation quality will be seriously degraded. In consequence of that, the linearisation techniques should be specially designed for these wireless transmitters.

## 2.10. References

- [2.1] A. Mohammadi and F. M. Ghannouchi, "RF Transceiver Design for MIMO Wireless Communications." Springer, 2012.
- [2.2] D. Bondar, "Advanced Digital Predistortion of Power Amplifiers for Mobile and Wireless Communications", PhD Thesis, University of Westminster, London, UK, 2009.
- [2.3] W. Bösch and G. Gatti, "Measurement and simulation of memory effects in predistortion linearizers," *IEEE Trans. Microw. Theory Tech.*, vol. 37, pp. 1885–1890, Dec. 1989.
- [2.4] J. Vuolevi, T. Rahkonen, and J. Manninen, "Measurement technique for characterizing memory effects in RF power amplifiers," *IEEE Trans. Microw. Theory Tech.*, vol. 49, no. 8, pp. 1383–1389, Aug. 2001.

- [2.5] H. Ku, M. D. Mckinley, and J. S. Kenney, "Extraction of accurate behavioral models for power amplifiers with memory effects using two-tone measurements," in *IEEE MTT-S Int. Microw. Symp. Dig.*, Seattle, WA, pp. 139–142, 2002.
- [2.6] D. H. Wisell, B. Rudlund, and D. Ronnow, "Characterization of memory effects in power amplifiers using digital two-tone measurements," *IEEE Trans. Instrum. Meas.*, Vol. 56, No. 6, pp. 2757–2766, Dec. 2007.
- [2.7] F. M. Ghannouchi, and O. Hammi, "Behavioral modeling and predistortion," *IEEE Microw. Mag.*, vol.10, no.7, pp.52-64, Dec. 2009.
- [2.8] O. Hammi, M. Younes, and F. M. Ghannouchi, "Metrics and Methods for Benchmarking of RF Transmitter Behavioral Models With Application to the Development of a Hybrid Memory Polynomial Model," *IEEE Trans. Broad.*, vol. 56, no. 3, Sept. 2010.
- [2.9] E. Dahlman, S. Parkvall, J. Sköld and P. Beming, „3G Evolution HSPA and LTE for Mobile Broadband,” Linacre House, Jordan Hill, Oxford, OX2 8DP, Second edition, 2008.
- [2.10] ETSI TS 136 106 V8.3.0 (2009-10) Technical Specification. Available Online:  
[http://www.etsi.org/deliver/etsi\\_ts/136100\\_136199/136106/08.03.00\\_60/ts\\_136106v080300p.pdf](http://www.etsi.org/deliver/etsi_ts/136100_136199/136106/08.03.00_60/ts_136106v080300p.pdf)
- [2.11] "3GPP Long Term Evolution. System Overview, Product Development, and Test Challenges," Agilent Technologies, Palo Alto, CA, USA, Application Note 5991-2556EN, July 2013.  
Available Online: <http://cp.literature.agilent.com/litweb/pdf/5991-2556EN.pdf>
- [2.12] 3GPP Technical Specification, TS 36.104 V8.4.0.  
Available Online: [http://www.3gpp.org/ftp/Specs/latest/Rel-8/36\\_series/](http://www.3gpp.org/ftp/Specs/latest/Rel-8/36_series/)
- [2.13] S.A Bassam, M. Helaoui, and F.M. Ghannouchi, "Crossover Digital Predistorter for the Compensation of Crosstalk and Nonlinearity in MIMO

Transmitters," *IEEE Trans. Microw. Theory Tech.* , vol.57, no.5, pp.1119-1128, May 2009.

- [2.14] S. A. Bassam, F. M. Ghannouchi and M. Helaoui, "Multi-Cell Processing Architectures for Modeling and Impairment Compensation in Multi-Input Multi-output Systems," US Patent Application 12/780/455, filed 14 May 2010.
- [2.15] S. A. Bassam, M. Helaoui, S. Boumaiza, and F. M. Ghannouchi, "Experimental study of the effects of RF front-end imperfection on the MIMO transmitter performance," in *IEEE MTT-S Int. Microw. Symp. Dig.*, Atlanta, GA, Jun. 2008, pp. 1187–1190.
- [2.16] **M. Cabarkapa**, M. Bozic, N. Neskovic, A. Neskovic and D. Budimir, "Compensation of Undesired Effects in MIMO Wireless Transceivers", *IEEE International Symposium on Antennas and Propagation and CNC/USNC/URSI National Radio Science Meeting (APS2012)*, pp. 1-2, July 8-14, 2012, Chicago, Illinois, USA.
- [2.17] S. A. Bassam, M. Helaoui, and F. M. Ghannouchi, "2-D digital predistortion (2-D-DPD) architecture for concurrent dual-band transmitters," *IEEE Trans. Microw. Theory Tech.*, vol. 59, no. 10, pp. 2547–2553, Oct. 2011.

### 3. Digital Predistortion Linearisation Techniques

#### 3.1. Introduction

In order to achieve high capacity requirements of modern mobile wireless systems (WCDMA, HSPA, LTE and mobile WiMAX), high linearity is required in the entire signal path of both transmitter and receiver. As it was mentioned previously, the most rapidly developing power amplifier linearisation technique is Digital Predistortion (DPD) [3.1]-[3.8]. With the aim of being more energy efficient, PAs should operate in the highly nonlinear region close to saturation. However, when they operate in that region, PAs produce high level of in-band and out-of-band distortion. In order to reduce these distortions and improve signal quality, a baseband signal should be passed through DPD lineariser implemented into Digital Signal Processing (DSP) that, in an ideal case, is the PA's inverse transfer function (Figure 3.1). As can be seen, the overall transmitter's response is linear in that case.

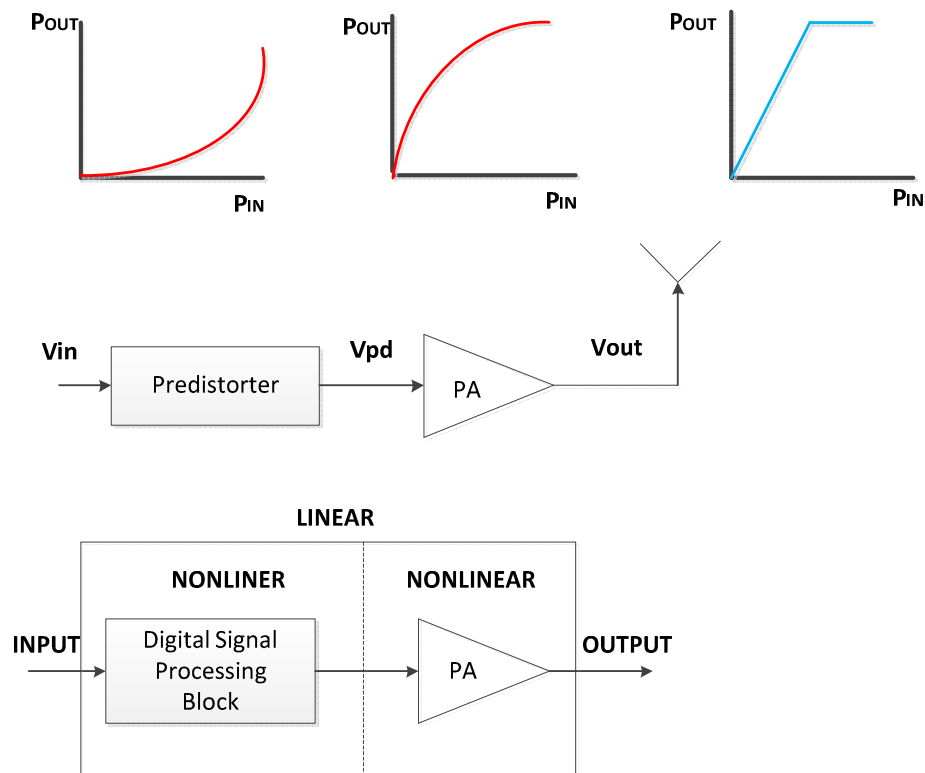


**Figure 3-1:** The fundamental concept of digital predistortion

The current chapter presents an overview of all the major DPD techniques used to increase the linearity of different types of wireless transmitters, describing the concepts of the techniques and highlighting their advantages and drawbacks.

### 3.2. DUT Model Extraction

Digital predistortion applies a complementary nonlinearity upstream of the PA so that the cascade of the digital predistorter and the PA behaves as a linear amplification system [3.9]. Behavioural modelling is essential to predict the nonlinearity of the PA and the transmitter in general. The synthesis of the predistortion function can be considered equivalent to behavioural modelling of the PA's inverse transfer function obtained by substitution of the PA's input and output signals with appropriate small-signal gain normalisation [3.9].

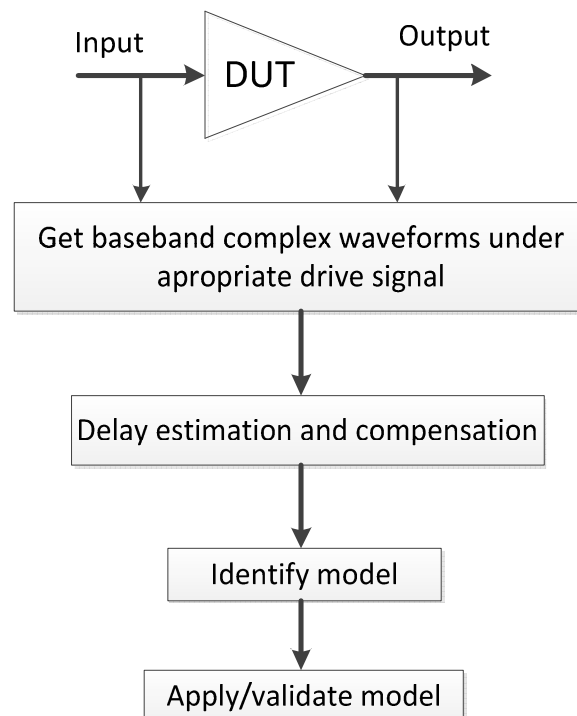


**Figure 3-2:** Behavioural model extraction procedure. Key steps from measurements to model validation

Behavioural modelling of DUT is very important in order to accurately quantify PA nonlinearities and memory effects [3.9]-[3.13]. Typically, DPD is considered closely together with Behavioural Modelling procedure [3.9]. This procedure is shown in Figure 3.2. The propagation delay through the DUT will introduce a mismatch

between the data samples used to calculate the instantaneous AM/AM and AM/PM characteristics of the DUT. This mismatch will translate into dispersion in the AM/AM and AM/PM characteristics that can be wrongly considered as memory effects. Therefore, the captured PA output signal must be time-aligned with the captured input signal [3.9]. The time-aligned input and output waveforms are then used to identify the behavioural model/digital predistorter of the DUT as well as its performance.

To sum up, one can say that the behavioural modelling procedure can be divided into two major parts: the observation and the formulation.

- The observation refers to the accurate acquisition of the signals at the input and output of the PA. This part includes experimental capturing of the signals and delay estimation and compensation procedure [3.9].
- The formulation corresponds to the choice of a suitable mathematical relation that describes all the significant interaction between the PA's input and output signals, its identification and validation [3.9].

Various mathematical representations of the model ("formulations") have been proposed for behavioural modelling and digital predistortion of RF PAs and transmitters [3.9]-[3.13]. The following section brings the description of the most widely used models.

### 3.3. Mathematical Representation of the Models

#### 3.3.1. Look-up-table Models

The look-up-table model is the basic behavioural model for memoryless AM/AM and AM/PM nonlinearities firstly introduced in [3.14]. The complex gain of the DUT is stored in two look-up tables. The output signal is given by:

$$x_{out}(n) = G(|x_{in}(n)|) \cdot x_{in}(n) \quad (3.1)$$

where  $G(|x_{in}(n)|)$  is the instantaneous complex gain of the DUT. The AM/AM and AM/PM characteristics of the DUT are derived from the measured data using averaging or polynomial fitting techniques. The nested look-up-table model was proposed to adapt the conventional look-up-table-based model to include memory effects [3.9]. The output waveform is given by

$$x_{out}(n) = G(|X_{in}(n)|) \cdot x_{in}(n) \quad (3.2)$$

where  $G(|X_{in}(n)|)$  is the instantaneous complex gain of the DUT, and  $X_{in}(n)$  is the input vector including the present and the  $M-1$  preceding samples defined as

$$X_{in}(n) = [x_{in}(n), x_{in}(n-1), \dots, x_{in}(n-M)] \quad (3.3)$$

To clarify, if the memory depth of nested look-up table is  $M = 1$ , there are  $K^2$  extracted and stored values of  $G(|X_{in}(n)|)$ , where  $K$  is a size of conventional LUT. In general case, there are  $K^{M+1}$  extracted and stored values of  $G(|X_{in}(n)|)$ . For instance, if  $K = 2^9 = 128$ , there will be 128 possible regions of amplitude  $|x_{in}(n)|$ . For each of these regions, there will be 128 possible regions of amplitude  $|x_{in}(n-1)|$ . Therefore, the instantaneous complex gain  $G$  should be extracted and indexed in two levels depending on amplitudes  $|x_{in}(n)|$  and  $|x_{in}(n-1)|$ . This is conventionally written as  $G(|X_{in}(n)|) = G(|x_{in}(n)|, |x_{in}(n-1)|)$ .

### 3.3.2. Volterra Models

**Volterra Model** is the most comprehensive model for dynamic nonlinear system. In this model, the relationship between the input and output waveforms is:

$$y(n) = \sum_{k=1}^K \sum_{i_1=0}^M \dots \sum_{i_p=0}^M h_p(i_1, i_2, \dots, i_p) \prod_{j=1}^k x(n - i_j) \quad (3.4)$$

where  $h_p(i_1, i_2, \dots, i_p)$  are the parameters of the Volterra model,  $K$  is the nonlinearity order of the model, and  $M$  is the memory depth. In fact, the number of parameters in

conventional Volterra model increases exponentially with nonlinearity order and memory depth. This limits the practical use of the Volterra series. To decrease this complexity, several techniques have been proposed to simplify the Volterra model. These include the pruning techniques and the dynamic deviation reduction technique [3.15], [3.5]. The Volterra-based models have demonstrated high accuracy in modelling mildly nonlinear PAs and transmitters.

To overcome the limitation of the classical Volterra series, a Volterra-like approach, called a modified Volterra series or dynamic Volterra series is developed, in which the input/output relationship for nonlinear system with memory is described as a memoryless nonlinear term plus a purely dynamic contribution. This was based on introducing dynamic deviation function

$$e(n, i) = x(n - i) - x(n) \quad (3.5)$$

which represents the deviation of the delayed input signal  $x(n - i)$  with the respect to the current input signal  $x(n)$ . This dynamic deviation function modifies (3.4) as follows:

$$y(n) = \sum_{k=1}^K \sum_{i_1=0}^M \dots \sum_{i_p=0}^M h_p(i_1, i_2, \dots, i_p) \prod_{j=1}^k [x(n) + e(n, i_j)] \quad (3.6)$$

In order to take advantage of the modified Volterra series, but also keep the model extraction as simple as possible, the following representation of the Volterra series is derived in [3.5]:

$$y(n) = \sum_{p=1}^P h_{p,0}(0, \dots, 0) x^p(n) + \sum_{p=1}^P \left\{ \sum_{r=1}^p \left[ x^{p-r}(n) \sum_{i_1=1}^M \dots \sum_{i_r=i_{r-1}}^M h_{p,r}(0 \dots 0, i_1 \dots i_r) \prod_{j=1}^r x(n - i_j) \right] \right\} \quad (3.7)$$

where  $h_{p,r}(0 \dots 0, i_1 \dots i_r)$  represents  $p$ th order Volterra kernel where the first  $p - r$  indices are “0”, corresponding to the input item  $x^{p-r}(n)x(n - i_1), \dots x(n - i_r)$ . In this representation  $r$  is the possible number of product terms of the delayed inputs in the input items.

### 3.3.3. Memory Polynomial Models

The memory polynomial model is widely used for behavioural modelling and digital predistortion of PAs/transmitters exhibiting memory effects. It corresponds to a reduction of the Volterra series in which only diagonal terms are kept [3.6]. The output waveform of the model is

$$y(n) = \sum_{k=1}^{K-1} \sum_{m=0}^{M-1} a_{km} \cdot x(n - m) \cdot |x(n - m)|^{k-1} \quad (3.8)$$

where  $K$  and  $M$  are the nonlinearity order and the memory depth of the DUT, respectively, and  $a_{mk}$  are the model coefficients.

Several variations of the memory polynomial model have been proposed in the literature. These include the orthogonal memory polynomial model [3.16], the envelope memory polynomial [3.9] and the memory polynomial model with cross-terms also referred to as the generalised memory polynomial model [3.6].

**The Envelope Memory Polynomial Model** can be seen as a combination between the memory polynomial model and the nested look-up model [3.9]. The output signal of the envelope memory polynomial model is given by

$$y(n) = \sum_{m=0}^M \sum_{k=1}^K a_{km} \cdot x(n) \cdot |x(n - m)|^{k-1} \quad (3.9)$$

where  $K$  and  $M$  are the nonlinearity order and the memory depth of the DUT, respectively, and  $a_{km}$  are the model coefficients. This formulation is similar to that of the memory polynomial model, except that only the magnitude information of the memory terms  $[x(n - 1), x(n - 2), \dots, x(n - M)]$  is required and their complex values

are not used. This makes this model simple to use for DPD implementation. It can be seen as an implementation of the nested look-up table model that takes advantage of the compact formulation and simple identification of memory polynomial model, where

$$G(|X(n)|) = \sum_{m=0}^M \sum_{k=1}^K a_{km} \cdot |x(n-m)|^{k-1} \quad (3.10).$$

**The Generalised Memory Polynomial Model** introduces cross-terms using the alternative Volterra formulation [3.6]. Thus, a generalised form of the  $k$ -th memory polynomial component is written in

$$\sum_{m=0}^M \sum_{k=1}^K b_{km} \cdot x(n) x(n-m)^k \quad (3.11),$$

where a delay of samples between the signal and its exponentiated envelope is inserted. Taking multiple such delayed versions of (3.11) using both positive and negative cross-term time shifts and combining with (3.8) results in the generalised memory polynomial

$$\begin{aligned} y(n) = & \sum_{k=0}^{K_a-1} \sum_{l=0}^{L_a-1} a_{kl} x(n-l) |x(n-l)|^k \\ & + \sum_{k=1}^{K_b} \sum_{l=0}^{L_b-1} \sum_{m=1}^{M_b} b_{klm} x(n-l) |x(n-l-m)|^k \\ & + \sum_{k=1}^{K_c} \sum_{l=0}^{L_c-1} \sum_{m=1}^{M_c} c_{klm} x(n-l) |x(n-l+m)|^k \end{aligned} \quad (3.12)$$

Here,  $K_a L_a$  are the number of coefficients for aligned signal and envelope (memory polynomial);  $K_b L_b M_b$  are the number of coefficients for signal and lagging (delaying) envelope; and  $K_c L_c M_c$  are the number of coefficients for signal and leading envelope. The main advantage of this cross-term model is that the coefficients, like those of the

memory polynomial, appear in linear form. Therefore, all of the coefficients can be simply and robustly estimated using any least-squares type of algorithm. This has positive implications for algorithm stability and computational complexity.

### 3.3.4. Wiener Model

The Wiener model is a two-box model composed of a linear finite impulse response (FIR) filter followed by a memoryless nonlinear function (see [3.9] and references therein). The output of this model is given by

$$x_{out}(n) = G(|x_1(n)|) \cdot x_1(n) \quad (3.13)$$

and

$$x_1(n) = \sum_{j=0}^M h(j) \cdot x_{in}(n-j) \quad (3.14)$$

where  $G$  is the memoryless instantaneous gain function implemented in the look-up table model and  $x_1(n)$  designates the output of the FIR filter,  $h(j)$  are the coefficients of the FIR filter impulse response, and  $M$  is the memory depth of the DUT.

### 3.3.5. Hammerstein Model

In the Hammerstein model, the static nonlinearity is applied before the linear filter (see [3.9] and references therein). Thus, the output waveform is given by:

$$x_{out}(n) = \sum_{j=0}^M h(j) \cdot x_1(n-j) \quad (3.15)$$

and

$$x_1(n) = G(|x_{in}(n)|) \cdot x_{in}(n) \quad (3.16)$$

where  $x_1(n)$ ,  $h(j)$ , and  $G(|x_{in}(n)|)$  refer to the output of the first box (look-up table model), the impulse response of the FIR filter, and the instantaneous gain of the look-up table model, respectively, and  $M$  is the memory depth of the DUT.

### 3.4. Behavioural Modelling Based Digital Predistortion

Over the years, many different approaches have been proposed to identify the coefficients of a digital predistorter [3.17]. In [3.18], a random search method based on a simple parameter perturbation was applied to identify a predistorter directly. However, it suffered from very slow convergence rate. The characteristic of a nonlinear PA was first estimated, and an analytical solution was then found to derive the inverse function of the PA in [3.19]. This approach is only feasible when the nonlinear order is low, since when the order becomes higher it will involve high computational complexity. Recently, many other identification structures have been proposed to identify the predistorter more efficiently and accurately. These identification structures are based on direct and indirect learning methods in general.

#### 3.4.1. Identification of DPD Functions – Direct and Indirect Learning Architectures

In order to identify digital predistorter, the methodology named Direct Learning has been widely proposed [3.20]-[3.22]. This technique is done by first constructing a direct model of the transmitter and then inverting this model. Direct learning means that the model of the input-output relation of the power amplifier is estimated first, and the predistortion is obtained directly by “pre-inverting” this PA characteristic. It should be noticed that an inverse of the power amplifier behavioural model is used directly to construct the DPD. This architecture commonly utilises the iterative procedures to optimise the parameter of DPD in order to minimise the error [3.21]. Figure 3-3 shows the block diagram of direct learning identification methodology. In order to minimise the errors between the output signal and the desired signal, the coefficients of the predistorter are estimated using adaptive algorithms [3.21]. In general, the direct learning method can have better performance than the indirect learning method.

However, the computational complexity of direct learning is higher and it usually converges more slowly.

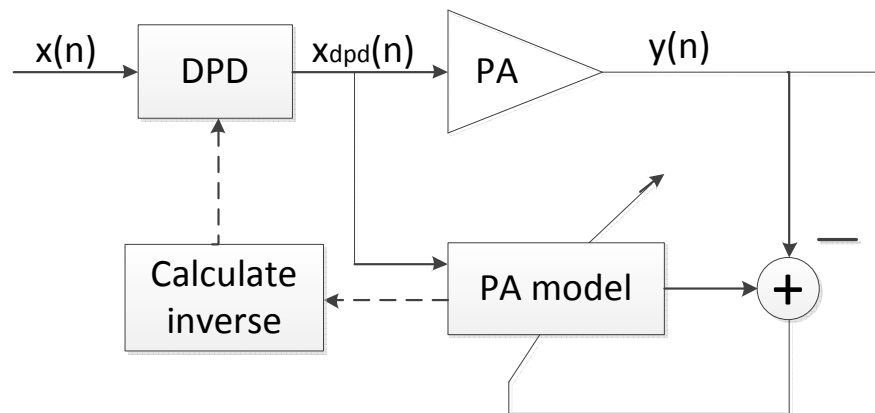


**Figure 3-3:** Direct learning DPD architecture

A large number of digital predistorters are based on indirect learning architecture (ILA) [3.1], [3.4], [3.23]. The method is named the indirect learning due to the post-inverse coefficients are first identified and then copied to work as a digital predistorter [3.23]. This post-compensator models the output into the desired input, and after that, can be used as a pre-inverting model for the DPD. This technique is shown in Figure 3-3.

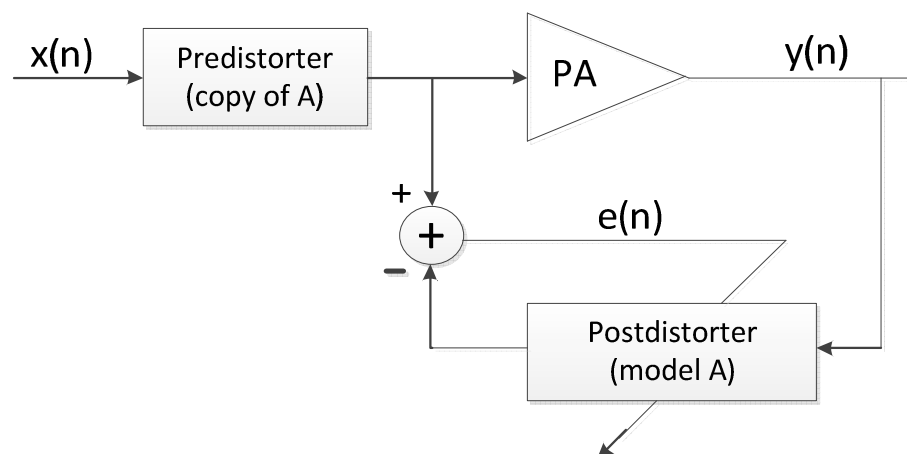


**Figure 3-4:** Indirect learning DPD architecture

Indirect learning means that a postdistorter first derives a postinverse of the nonlinear model without any predistorter and then the postdistorter is used as a

predistorter. The ILA typically uses block based least square solution [3.24], [3.25]. It has been shown that when a good behavioural model is obtained, a good inverse model can also be obtained [3.4]. Although this was verified in some cases, this is not a general fact. In some cases, the inversion of a nonlinear system may not be possible. In other words, not all nonlinear systems possess an inverse, and many systems can be inverted only for a restricted amplitude range of input [3.21].

The pros and cons of direct and indirect learning identification structures have been compared and summarised in [3.22] and [3.24].

### 3.5. Digital Predistortion Based on Artificial Neural Networks

Recently, the novel technique of artificial neural networks (ANNs) has attracted researchers in the field of PA modelling due to its successful implementation in signal processing, system identification, and control [3.26], [3.27]. The ANN approach has also been investigated as one of the DPD techniques for PAs and transmitters. Using ANN in this context is attractive because of its adaptive nature and the claim of a universal approximation capability. The real-valued recurrent neural network (RVRNN) shown in Figure 3-5 is one of the possible solutions of network topology. However, the real-valued focused time-delay neural network (RVFTDNN), also shown in Figure 3-5, was found to be the most suitable, accurate, and robust model for DPD-based linearisation of mildly as well as strongly nonlinear PAs [3.28]. This ANN is presented with input vectors of the length  $2(m + 1)$ , including real values of present and past inputs

$$X_{in} = [I_{in}(n), I_{in}(n - 1) \dots I_{in}(n - m), Q_{in}(n), Q_{in}(n - 1) \dots Q_{in}(n - m)], \quad (3.17)$$

where  $m$  is the memory depth. The outputs of ANN are expressed as follows:

$$I_{out}(n) = f_1(X_{in}(n)) \quad (3.18)$$

$$Q_{out}(n) = f_2(X_{in}(n)) \quad (3.19)$$

where  $f_1$  and  $f_2$  are functions modelled by RVFTDNN at any time instant  $n$ .

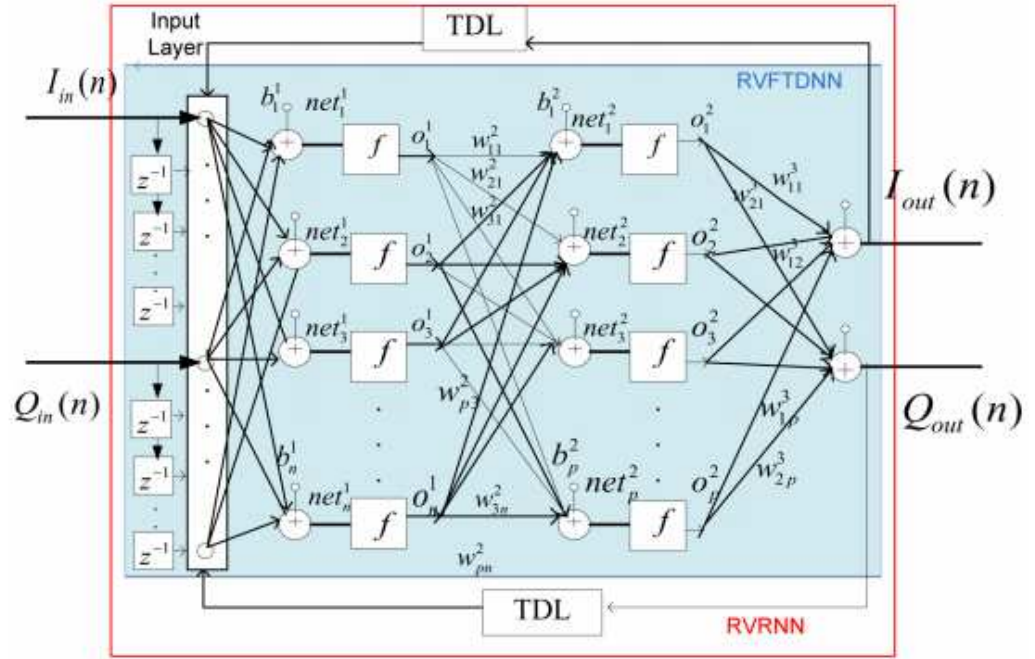


**Figure 3-5:** RVFTDNN and RVRNN schematics [3.28]

The *net* at any layer is given by

$$net_j^l(n) = \sum_{i=1}^q \omega_{ji}^l x_{in,i}^{l-1}(n) + b_j^l \quad (3.20)$$

where  $j$  denotes a neuron in hidden layer  $l$ , and  $\omega_{ji}^l$  denotes the synaptic weight connecting the  $i$ -th input to the  $j$ -th neuron of layer  $l$ . The output of any layer is given as

$$o_j^l = f(net_j^l(n)). \quad (3.21)$$

The output of any layer works as an input for the next layer. The output layer has a purelin activation function, which sums up the outputs of hidden neurons and linearly maps them at the output. The activation function for two hidden layers is typically the tansig function, which maps nonlinearity between -1 and 1 and is mathematically equivalent to hyperbolic tangent given as

$$\tanh(x) = \frac{\exp(x) - \exp(-x)}{\exp(x) + \exp(-x)} \quad (3.22)$$

Training is carried out in batch mode, supervised with a back-propagation learning algorithm (BPLA). During one epoch or iteration, two passes are made. During the forward pass, the cost function is calculated by

$$E = \frac{1}{2N} \sum_{n=1}^N [(I_{out}(n) - \hat{I}_{out}(n))^2 + (Q_{out}(n) - \hat{Q}_{out}(n))^2] \quad (3.23)$$

where  $I_{out}(n)$  and  $Q_{out}(n)$  are the desired outputs, and  $\hat{I}_{out}(n)$  and  $\hat{Q}_{out}(n)$  are the outputs from the ANN. Based on the error signal, backward computation is done in (3.20) to adjust the synaptic weights of the network in layer according to

$$\omega(n+1) = \omega(n) + \Delta\omega(n) \quad (3.24)$$

In (3.24),  $\omega(n)$  denotes the weights at a previous time instant,  $\omega(n+1)$  is the updated weight, and  $\Delta\omega(n)$  is calculated using the 1-D Levenberg–Marquardt algorithm form with the aim of minimizing the cost function. This algorithm was selected from among various algorithms because of its fast convergence properties [3.28]. For updated weights, the cost function is calculated in the forward pass; and, the whole procedure is carried out again until the desired performance is met or the ANN starts failing the validation procedure, drifting away from the generalisation criterion.

The RVFTDNN was trained to extract the normalised inverse characteristics according to

$$X_{in} = f^{-1}(y_{norm}) \quad (3.25)$$

where  $y_{norm}$  denotes the vector containing the I and Q components for the PA output at that instance and previous instances after normalizing it with a small-signal gain, and  $X_{in}$  denotes the vector containing the I and Q components of the input to the PA at that instance. The memory length was decided by an optimisation process. Finally, the initial input signal is passed through this trained ANN which actually acts as digital predistorter.

This solution can be further extended and Figure 3-6 depicts the ANN structure, where the in-phase (I) and quadrature (Q) components of the PA input and output

signals are used as network inputs [3.29]. This ANN model can be seen as a generalised version of the model described previously.

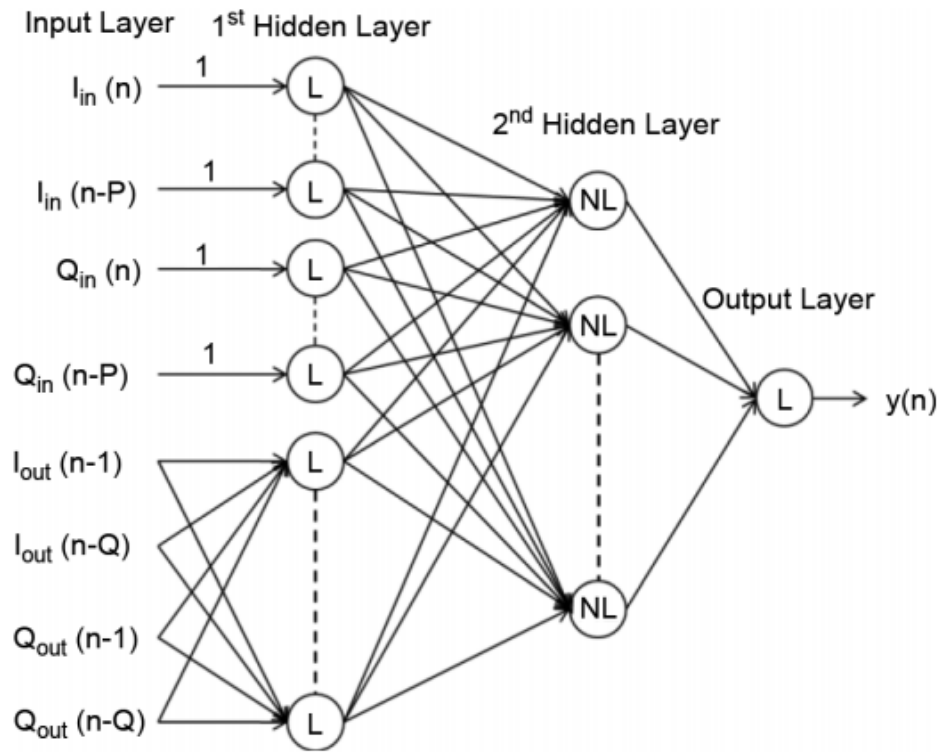


**Figure 3-6:** A generalised real-valued two hidden layers ANN model for a PA [3.29]

The following two sections describe the extensions of the previously presented solutions to be applicable in multi-branch and multi-frequency MIMO transmitters. However, these advanced solutions are followed by dramatic increase of the complexity that precludes their practical implementation.

### 3.6. Digital Predistortion for Multi-branch MIMO Transmitters

As it was discussed previously, the compensation of the PA nonlinearity is the main goal of DPD. However, there are other side effects such as quadrature modulation/demodulation (QM/QDM) errors [3.30], Local Oscillator (LO) self-coupling problem [3.31] or crosstalk specific to multi-branch MIMO systems [3.32], [3.33] to be aware of. The description of the crosstalk problem is given in Chapter 2. This section describes DPD models specifically designed for multi-branch MIMO transmitters to jointly compensate nonlinear crosstalk and PA nonlinearity.

### 3.6.1. Crossover Digital Predistortion (CO-DPD)

Conventional DPDs are not able to compensate for transmitter nonlinearity in the presence of nonlinear crosstalk. Therefore, the crossover digital predistorter (CO-DPD) model that can jointly compensate for both nonlinear crosstalk and transmitter nonlinearities was developed [3.32]. It can be assumed that there is only one major nonlinear component (PA) in the transmitter chain, and therefore, all the crosstalk terms from different sources could be added up before the PA to represent the nonlinear crosstalk. The linear crosstalk appears after the PA and is named the antenna crosstalk. Its effect can be compensated together with the effect of the wireless fading channel at the receiver side [3.32].

In the CO-DPD model, the entire MIMO transmitter is considered as a nonlinear system with two inputs  $(x_1, x_2)$  and two outputs  $(y_1, y_2)$ . The relation between the inputs and outputs is shown in matrix form as follows:

$$[y_1 \ y_2] = W[x_1 \ x_2]^T \quad (3.26)$$

where  $W$  is a nonlinear matrix function representing the nonlinear behaviour of the transmitter, which is composed of the PAs nonlinearity and the nonlinear crosstalk.

The conventional memory polynomial model is used to characterise the static and dynamic (memory effects) nonlinear behaviour of the transmitter. The closed-form expression relating the complex signals at the input and output of the nonlinear transmitter can be written as follows:

$$y(n) = \sum_{q=0}^Q \sum_{k=1}^K h_{k,q} |x(n-q)|^{k-1} x(n-q) \quad (3.27)$$

where  $x(n)$  and  $y(n)$  are the input and output complex signals,  $h_{k,q}$  are the polynomial coefficients,  $K$  and  $Q$  are the maximum polynomial order and memory depth, respectively. The memory polynomial model can be rewritten into the matrix form as follows:

$$\vec{y} = A_{\vec{x}} \vec{h} \quad (3.28)$$

where each symbol is defined as follows:

- $\vec{y} = [y(1) \dots y(N)]^T$  is  $N \times 1$  an vector representing  $N$  samples of the output signal.
- $\vec{h} = [h_{1,0} \ h_{2,0} \ \dots \ h_{K,0} \ \dots \ h_{1,Q} \ h_{2,Q} \ \dots \ h_{K,Q}]$  is a  $K(Q + 1)$  vector of the polynomial coefficients.
- $A_{\vec{x}} = [\beta_{\vec{x}}^0 \ \dots \ \beta_{\vec{x}}^q \ \dots \ \beta_{\vec{x}}^Q]$  is an  $N \times K(Q + 1)$  matrix
- $\beta_{\vec{x}}^q = \begin{bmatrix} 0_{1 \times q} & 0_{1 \times q} & \dots & 0_{1 \times q} \\ \beta_1(x(1)) & \beta_2(x(1)) & \dots & \beta_K(x(1)) \\ \vdots & \vdots & \ddots & \vdots \\ \beta_1(x(N - q)) & \beta_2(x(N - q)) & \dots & \beta_K(x(N - q)) \end{bmatrix}$  is a  $N \times K$  matrix and  $\beta_k(x(n))$  is defined as  $\beta_k(x(n)) = x(n)^{k-1}x(n)$ .
- $\vec{x} = [x(1) \dots x(N)]^T$  is an  $N \times 1$  vector representing  $N$  samples of the input signal.

The  $h_{k,q}$  coefficients can be determined by the pseudoinversing  $A_{\vec{x}}$  matrix as follows:

$$\vec{h} = \text{pinv}(A_{\vec{x}})\vec{y} \quad (3.29)$$

where  $\text{pinv}(A_{\vec{x}}) = (A_{\vec{x}}^H A_{\vec{x}})^{-1} A_{\vec{x}}^H$  is the pseudo-inverse of matrix  $A_{\vec{x}}$ . The memory polynomial model can be extended for the MIMO case, where there are two inputs and two outputs. The expression in (3.28) is extended for the dual-input dual-output system as follows:

$$[\vec{y}_1 \ \vec{y}_2] = [A_{\vec{x}_1} \ A_{\vec{x}_2}] \begin{bmatrix} \vec{h}_{1,1} & \vec{h}_{2,1} \\ \vec{h}_{1,2} & \vec{h}_{2,2} \end{bmatrix} \quad (3.30)$$

where  $A_{\vec{x}_1}$  and  $A_{\vec{x}_2}$  are the matrices defined for inputs  $\vec{x}_1$  and  $\vec{x}_2$ ,  $\vec{h}_{i,j}$  are the polynomial coefficients between input  $\vec{x}_j$  and output  $\vec{y}_i$ . Therefore the polynomial coefficients for the 2x2 MIMO model will be:

$$\begin{bmatrix} \overrightarrow{h_{1,1}} & \overrightarrow{h_{2,1}} \\ \overrightarrow{h_{1,2}} & \overrightarrow{h_{2,2}} \end{bmatrix} = \text{pinv}([A_{\overrightarrow{x_1}} \ A_{\overrightarrow{x_2}}])[\overrightarrow{y_1} \ \overrightarrow{y_2}]. \quad (3.31)$$

Similarly, to extract the DPD coefficients,  $\begin{bmatrix} \overrightarrow{d_{1,1}} & \overrightarrow{d_{2,1}} \\ \overrightarrow{d_{1,2}} & \overrightarrow{d_{2,2}} \end{bmatrix}$  the vector  $[\overrightarrow{y_1} \ \overrightarrow{y_2}]$  will be swapped with  $[\overrightarrow{x_1} \ \overrightarrow{x_2}]$ , and the  $A_{\overrightarrow{y_1}}$  and  $A_{\overrightarrow{y_2}}$  are defined based on output data  $\overrightarrow{y_1}$  and  $\overrightarrow{y_2}$ . Therefore, the DPD coefficients are:

$$\begin{bmatrix} \overrightarrow{d_{1,1}} & \overrightarrow{d_{2,1}} \\ \overrightarrow{d_{1,2}} & \overrightarrow{d_{2,2}} \end{bmatrix} = \text{pinv}([A_{\overrightarrow{y_1}} \ A_{\overrightarrow{y_2}}])[\overrightarrow{x_1} \ \overrightarrow{x_2}]. \quad (3.32)$$

The application of the calculated DPD functions is illustrated in Figure 3-7 where the DPD outputs  $z_1$  and  $z_2$  depend on both input signals  $x_1$  and  $x_2$ .

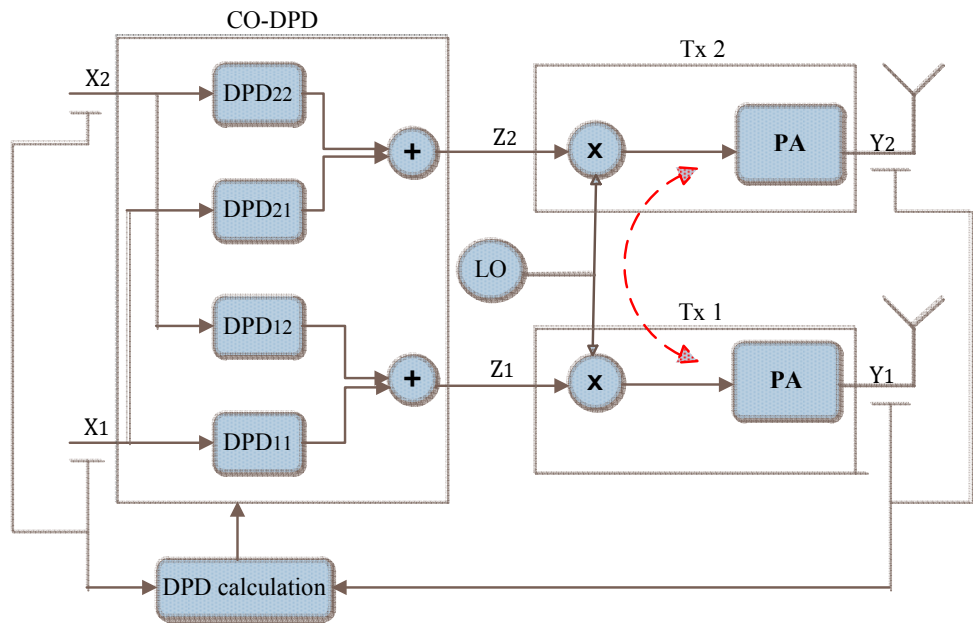


**Figure 3-7:** CO-DPD model for dual-branch transmitters

### 3.6.2. Digital Predistortion for Multi-branch MIMO Transmitters Based on Combined Feedback

When it is needed to apply previously described, conventional CO-DPD in transmitter with  $M$  transmitter's chains,  $M$  independent feedback paths are required (Figure 3-8(a)). To overcome multiple feedback paths, the two possible solutions were described in [3.34]. The first solution, shown in Figure 3-8(b), uses only one feedback

and time-sharing method among  $M$  PA outputs. In this case, crosstalk between different outputs is unavoidable and can seriously degrade the DPD linearisation performances. The second solution instead of constructing a separate feedback path at the output of each PA uses combined feedback which adds all the PAs' outputs to form a single feedback [3.34]. This solution is shown in Figure 3-8(c).

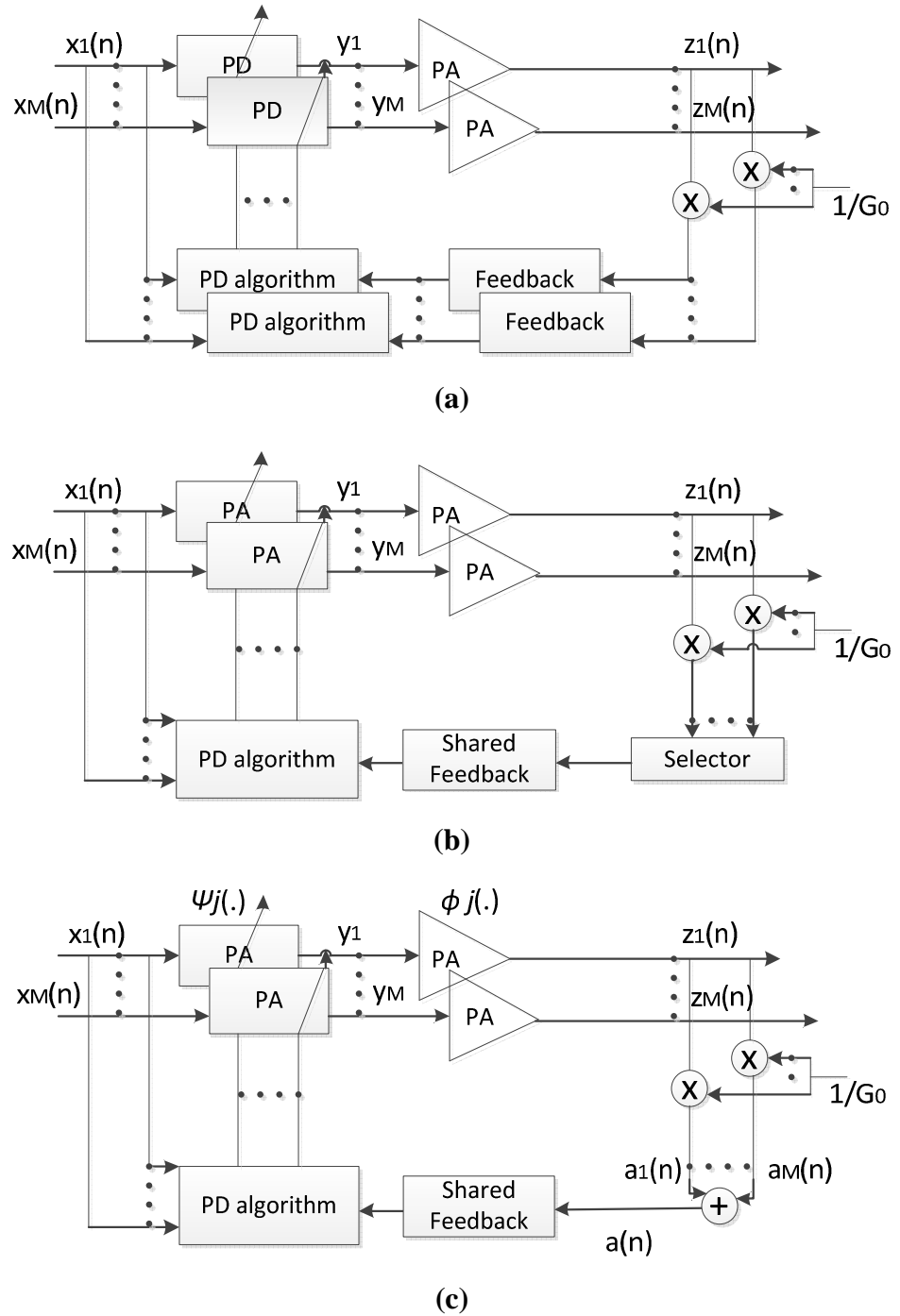


**Figure 3-8:** Multi-branch MIMO transmitter model: (a) with multiple feedbacks (b) with selector based shared feedback (c) with combiner based shared feedback

The DPD methodology shown in Figure 3-8(c) consists of two steps. The first step is PA identification procedure, and the second step is DPD parameters calculation from the identified PA characteristic.

The combined feedback signal  $a(n)$  can be written as follows:

$$a(n) = \frac{z_1(n)}{G_0} + \frac{z_2(n)}{G_0} + \dots + \frac{z_M(n)}{G_0} \approx \mathbf{w}^T \mathbf{y}(n) \quad (3.33)$$

where  $\mathbf{w} = [\mathbf{w}_1^T \mathbf{w}_2^T \dots \mathbf{w}_M^T]^T$  and  $\mathbf{y} = [\mathbf{y}_1^T \mathbf{y}_2^T \dots \mathbf{y}_M^T]^T$ . It should be noted that  $\mathbf{w}$  and  $\mathbf{y}(n)$  are the  $M$ -times augmented vectors by stacking up  $\{\mathbf{w}_i\}$  and  $\{\mathbf{y}_i(n)\}$ , respectively. Therefore, the size of  $\mathbf{w}$  is  $M$ -times bigger than that of  $\mathbf{w}_i$ , and by estimating  $\mathbf{w}$ ,  $M$  PA parameters  $\mathbf{w}_i$  for  $i = 1, \dots, M$  can be obtained. To identify the characteristic coefficients of the PAs, the error is defined as follows:

$$e(n) = a(n) - \tilde{\mathbf{w}}^T \mathbf{y}(n) \quad (3.34)$$

where  $\tilde{\mathbf{w}}$  is the PA parameter vector. To find the PA parameter  $\tilde{\mathbf{w}}$  that minimises  $e(n)$ , the least squares (LS) is employed. If  $N$  samples for  $n = 0, \dots, N$  are available and the PA characteristics are not changed during the  $N$ -sample period, the LS cost function can be expressed as:

$$J = \sum_{n=0}^N |e(n)|^2 = \sum_{n=0}^N |a(n) - \tilde{\mathbf{w}}^T \mathbf{y}(n)|^2 \quad (3.35)$$

The LS estimate of  $\tilde{\mathbf{w}}$  that minimises (3.35) can be obtained as:

$$\tilde{\mathbf{w}} = (\mathbf{Y}^H \mathbf{Y})^{-1} \mathbf{Y}^H \mathbf{a} \quad (3.36)$$

where  $\mathbf{a} = [a(1), a(2), \dots, a(N)]^T$  and  $\mathbf{Y} = [\mathbf{y}(1), \mathbf{y}(2), \dots, \mathbf{y}(N)]^T$ .

The next step is calculation of DPD functions. The parameters of DPDs can be calculated independently at each path because the  $M$  PA parameters are estimated. To find the DPD parameters, a cost function is defined for the  $j$ -th PA as follows:

$$\varepsilon_{hj} = E[|e_{hj}(n)|^2] \quad (3.37)$$

where

$$e_{hj}(n) = x_j(n) - z_j(n)/G_0. \quad (3.38)$$

As there is only one combined feedback path,  $z_j(n)$  cannot be used directly. Therefore, the  $j$ -th estimated PA parameter is used instead. Specifically, the error signals can be rewritten as:

$$e_{hj}(n) = x_j(n) - \tilde{\mathbf{w}}_j^T \mathbf{y}_j(n). \quad (3.39)$$

Using (3.39), the adaptive algorithm that minimises (3.37) can be applied (see [3.34] and references therein).

### 3.6.3. Simplified Crossover Digital Predistortion (Simplified CO-DPD)

This subsection is based on the author's publications [3.35] and [3.36]. The baseband equivalent transmitter model shown in Figure 3-9 is used to explain this concept like in [3.30], [3.31]. Undesired effects and the technique are explained in example of the MIMO transmitter with  $N$  RF front ends. Parameters  $\mathbf{c}_{ij}$  are used for crosstalk modelling between  $i$ -th and  $j$ -th RF front ends ( $i, j = 1, \dots, N$ , where  $j$  is crosstalk source branch,  $i$  is affected branch and  $\mathbf{c}_{ij} = \mathbf{c}_{ji}$ ). The affected signal with nonlinear crosstalk effects at the PA output of the  $i$ -th RF front end  $y_i$  is:

$$y_i = f_{PA}(\mathbf{c}_{i1} * z_1 + \dots + z_i + \dots + \mathbf{c}_{iN} * z_N) \quad (3.40)$$

where  $f_{PA}$  is nonlinear PA transfer function, the predistorted signal  $z_i = x_i$  when there are no additional blocks for DPD purposes (framed with green lines), and  $x_i$  ( $i = 1, \dots, N$ ) is the discrete time-domain OFDM signal at time instant  $n$  given as follows:

$$x_i(n) = \sum_{k=0}^{K-1} X_k^{(i)} e^{j\frac{2\pi}{K}kn} \quad (3.41)$$

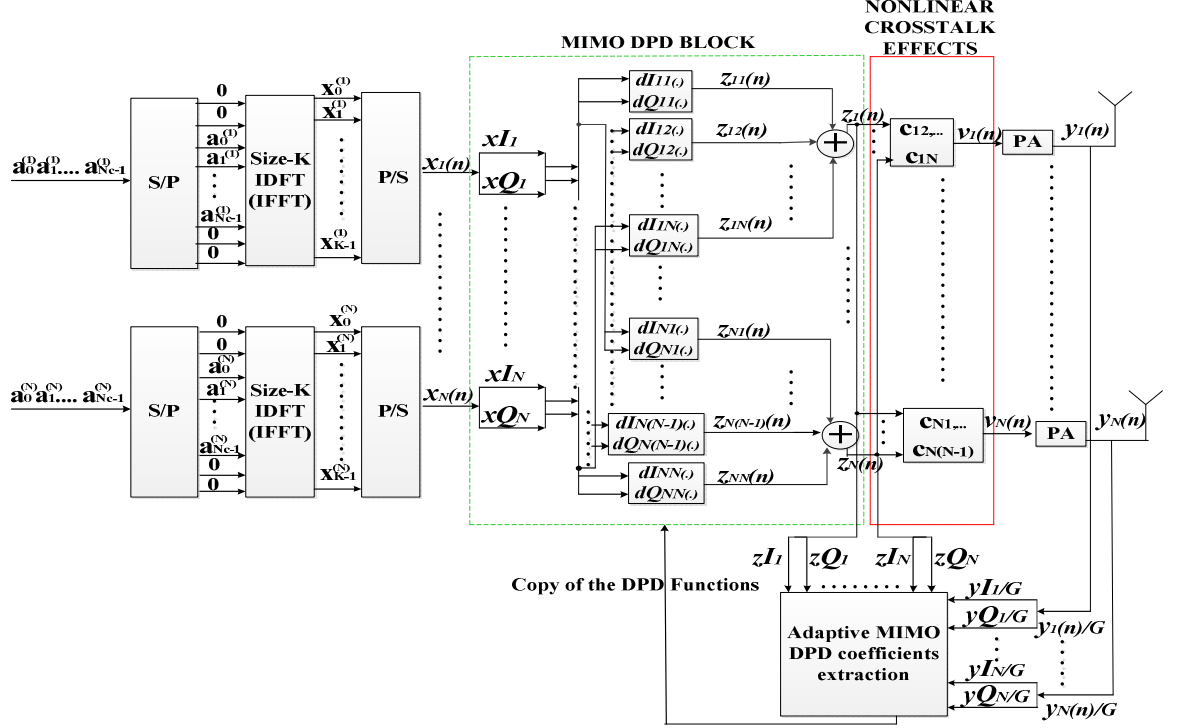


**Figure 3-9:** The baseband equivalent N-MIMO OFDM transmitter with simplified CO-DPD

The time-domain, PA input signal on carrier frequency  $\omega = 2\pi f$  with variable amplitude  $V_s(t)$  and variable phase  $\varphi(t)$  can be written as:

$$v_{IN}(t) = V_s(t) \cos(\omega t + \varphi(t)) = (vI(t) \cos \omega t - vQ(t) \sin \omega t)V \quad (3.42)$$

where  $V = |\overline{V_s(t)}|$  is the average value of the amplitude, normalised in-phase and quadrature components are  $vI(t) = \frac{V_s(t)}{V} \cos(\varphi(t))$ ,  $vQ(t) = \frac{V_s(t)}{V} \sin(\varphi(t))$ , and

$\overline{vI(t)^2 + vQ(t)^2} = 1$ . The PA nonlinear behaviour can be described with the quadrature Taylor-series amplifier model [3.37] given with the following equations:

$$y_i = (GI(vI_i) + jGQ(vQ_i))V_i \quad (3.43)$$

$$yI_i = GI(vI_i) = \sum_{k=0}^P A_k vI_i^k \quad (3.44)$$

$$yQ_i = GQ(vQ_i) = \sum_{k=0}^P B_k vQ_i^k \quad (3.45)$$

where  $y_i$  is a complex signal at the output of PA in  $i$ -th transmitter's branch ( $i = 1, \dots, N$ ),  $A_k$  and  $B_k$  are polynomial coefficients and  $P$  is a polynomial order of the PA model.

The proposed MIMO DPD block is shown in Figure 3-9. In order to suppress crosstalk effects from other branches, the predistorted signal at  $i$ -th transmitter's branch is a sum of signals from  $N$  branches:

$$z_i(n) = \sum_{k=1}^N zI_{ik} + j \sum_{k=1}^N zQ_{ik}, \quad i = 1, \dots, N \quad (3.46)$$

By substituting  $zI_{ik} = dI_{ik}(xI_k)$  and  $zQ_{ik} = dQ_{ik}(xQ_k)$ , signal  $z_i(n)$  becomes:

$$z_i(n) = \sum_{k=1}^N dI_{ik}(xI_k) + j \sum_{k=1}^N dQ_{ik}(xQ_k), \quad i = 1, \dots, N \quad (3.47)$$

where  $dI$  and  $dQ$  are  $P$ th-order polynomial functions with coefficients  $a_p$  and  $b_p$ :

$$dI(xI) = \sum_{p=1}^P a_p xI^p \quad (3.48)$$

$$dQ(xQ) = \sum_{p=1}^P b_p xQ^p \quad (3.49)$$

The polynomial functions  $dI_{ii}$  and  $dQ_{ii}$  ( $i=1, \dots, N$ ) are DPD functions which deal with PA nonlinearity. In contrast,  $dI_{ij}$  and  $dQ_{ij}$  ( $i, j = 1, \dots, N$  and  $i \neq j$ ) functions

have a goal to eliminate nonlinear crosstalk between  $i$ -th and  $j$ -th MIMO transmitter's paths. The equation (3.47) can be re-written into matrix form for the blocks of  $L$  samples as follows:

$$\vec{Z} = \begin{bmatrix} \overrightarrow{dI_{11}} & \dots & \overrightarrow{dI_{1N}} \\ \vdots & \ddots & \vdots \\ \overrightarrow{dI_{N1}} & \dots & \overrightarrow{dI_{NN}} \end{bmatrix} \begin{bmatrix} \mathbf{AI}_1 \\ \vdots \\ \mathbf{AI}_N \end{bmatrix} + j \begin{bmatrix} \overrightarrow{dQ_{11}} & \dots & \overrightarrow{dQ_{1N}} \\ \vdots & \ddots & \vdots \\ \overrightarrow{dQ_{N1}} & \dots & \overrightarrow{dQ_{NN}} \end{bmatrix} \begin{bmatrix} \mathbf{AQ}_1 \\ \vdots \\ \mathbf{AQ}_N \end{bmatrix} \quad (3.50)$$

where  $\overrightarrow{dI_{ij}}$  and  $\overrightarrow{dQ_{ij}}$  are vector representations of MIMO DPD polynomial coefficients for  $dI_{ij}$  and  $dQ_{ij}$  ( $i, j = 1, \dots, N$ ) polynomial functions;  $\vec{Z} = [\overrightarrow{ZI}_1 \dots \overrightarrow{ZI}_N]^T + j[\overrightarrow{ZQ}_1 \dots \overrightarrow{ZQ}_N]^T$ ;  $\overrightarrow{ZI}_i = [zI_i(1) \dots zI_i(L)]$  and  $\overrightarrow{ZQ}_i = [zQ_i(1) \dots zQ_i(L)]$  are the  $1 \times L$  vectors;

$$\mathbf{AI}_i = \begin{bmatrix} fI_1(xI(1)) & \dots & fI_1(xI(L)) \\ \vdots & & \vdots \\ fI_p(xI(1)) & \dots & fI_p(xI(L)) \end{bmatrix}$$

and

$$\mathbf{AQ}_i = \begin{bmatrix} fQ_1(xQ(1)) & \dots & fQ_1(xQ(L)) \\ \vdots & & \vdots \\ fQ_p(xQ(L1)) & \dots & fQ_p(xQ(L)) \end{bmatrix}$$

are  $P \times L$  matrices in which each element represents polynomial term  $fI_p(xI(n)) = (xI(n))^p$  or  $fQ_p(xQ(n)) = (xQ(n))^p$ , ( $p = 1$  for linear and  $p = 2, \dots, P$  for nonlinear terms), for matrices  $\mathbf{AI}_i$  and  $\mathbf{AQ}_i$ , respectively. The symbol  $P$  is a polynomial order and  $i$  denotes  $i$ -th MIMO transmitter's branch.

The coefficients of DPD polynomial functions  $dI_{ij}$  and  $dQ_{ij}$  ( $i, j = 1, \dots, N$ ) are extracted in feedback block named "Adaptive MIMO DPD coefficients extraction". This block calculates coefficients of DPD functions using modified expression (11). Namely, in (11), for the DPD extraction purpose, the terms  $xI(n)$  and  $xQ(n)$ ,  $n = 1, \dots, L$ , in matrices  $\mathbf{AI}_i$  and  $\mathbf{AQ}_i$  are replaced with  $\frac{yI(n)}{G}$  and  $\frac{yQ(n)}{G}$ , where  $G$  is a linear PA gain and  $n$  is sample's index. The solution of (3.50) given with the following equations

$$\begin{bmatrix} \overrightarrow{dI_{11}} & \dots & \overrightarrow{dI_{1N}} \\ \vdots & \ddots & \vdots \\ \overrightarrow{dI_{N1}} & \dots & \overrightarrow{dI_{NN}} \end{bmatrix} = \text{pinv}([\mathbf{AI}_1 \dots \mathbf{AI}_N])[\overrightarrow{ZI_1} \dots \overrightarrow{ZI_N}] \quad (3.51)$$

$$\begin{bmatrix} \overrightarrow{dQ_{11}} & \dots & \overrightarrow{dQ_{1N}} \\ \vdots & \ddots & \vdots \\ \overrightarrow{dQ_{N1}} & \dots & \overrightarrow{dQ_{NN}} \end{bmatrix} = \text{pinv}([\mathbf{AQ}_1 \dots \mathbf{AQ}_N])[\overrightarrow{ZQ_1} \dots \overrightarrow{ZQ_N}] \quad (3.52)$$

calculates the coefficients of the MIMO DPD polynomial functions. The function  $\text{pinv}(\mathbf{x}) = (\mathbf{x}^T \mathbf{x})^{-1} \mathbf{x}$  represents Moore-Penrose pseudo inverse based on inverting matrix using singular value decomposition and yields the well-known least square solution [3.38]-[3.40]. After this step, the extracted DPD functions are copied in “MIMO DPD Block” and applied to initial OFDM signals using (3.46). Therefore, this technique satisfies indirect learning adaptive DPD scheme [3.1], [3.4], [3.23] which is extended for the application in MIMO transmitters. As it was explained above, an excellent feature of the indirect learning is that it enables the estimation of the predistorter coefficients without need for a priori knowledge of the PA transfer functions.

### 3.7. Digital Predistortion for Multi-frequency MIMO Transmitters

The rapid development of multi-standard/multiband wireless communication systems has caused an urgent need for research on multi-frequency MIMO transmitters. The first step in developing transmitters of this kind is the design of dual-band transmitter and solving the problems specific to it. There have been frequent efforts to design transmitters to concurrently support two standards in different frequency bands (see [3.41] and references therein). The nonlinear PA that concurrently amplifies high peak-to-average power ratio (PAPR) wideband signals in two frequency bands produces distortion that significantly degrades signal quality. The distortion level is much higher in the case of dual-band transmitters than in the case of conventional single-band. Therefore, the baseband DPD have to be specifically designed for concurrent dual-band transmitters. In order to suppress distortion introduced in these transmitters, the various DPD techniques were proposed [3.41]-[3.52]. They are based on generalised frequency-

selective DPD architecture [3.42], dual-band IF DPD architecture [3.43], widely spaced carriers' DPD architecture [3.44], 2-D complex polynomials [3.41], [3.45], 2-D complex polynomials with subsampling feedback loop [3.46], 2-D complex cross-modulation (CM) basis functions [3.47], 2-D modified memory polynomials [3.48], 2-D augmented Hammerstein [3.49], 2-D Enhanced Hammerstein [3.50], dual-band memory polynomials based look-up tables (LUTs) [3.51] or extended real-valued focused time delay artificial neural networks (ANN) [3.52]. The linearisation performances of the solutions [3.42]-[3.44] depend on frequency separation between bands in concurrent dual-band transmitters. The solutions [3.41], [3.45]-[3.52] overcome this problem by using two identical DPD processing stages for two bands, two local oscillators and a combiner before the PA. This 2-D-DPD methodology based on dual-cell architecture was firstly presented in [3.41], where the RF signals in each band are captured and digitised separately. This architecture is shown in Figure 3-10. The model has been developed in such a way that two modulated signals contribute to the linearisation of each band. To clarify, in this architecture, there are two DPD blocks. The first one is used to compensate for the distortion at Band 1, whereas the second one is used to compensate for the distortion at Band 2. The outputs of both predistorter is then up-converted and combined together. The feedback signals are used in “Analyzing Stage” to train each DPD block separately.

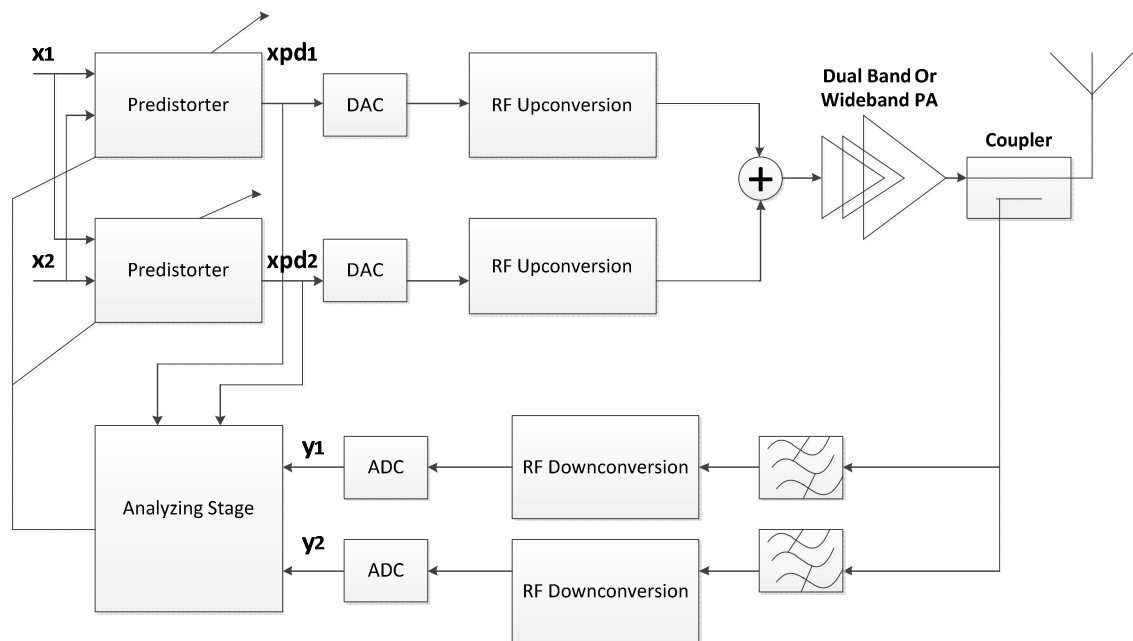


**Figure 3-10:** 2-D dual-cell DPD architecture

The solutions based on dual-cell architecture suffer from a high run-time computational complexity of predistorter design as well as a high computational complexity and numerical instability of DPD identification. However, these approaches were experimentally verified and widely used nowadays. The following subsections describe 2D-DPDs based on dual-cell architecture.

### 3.7.1. 2-D DPD Based on Memory Polynomials

The extension of the conventional memory polynomial model for an application in concurrent dual-band wireless transmitter is possible [3.41]. If the transmitter is modelled as memoryless fifth-order nonlinearity

$$y = x + x |x|^2 + x |x|^4 \quad (3.53)$$

and the discrete-time baseband equivalent input signal as

$$x = s_1 + s_2 = x_1 e^{-j\omega n T} + x_2 e^{j\omega n T} \quad (3.54)$$

the model output will be

$$\begin{aligned} y = & (x_1 + x_1 |x_1|^2 + x_1 |x_2|^2 + x_1 |x_1|^4 + 4x_1 |x_1|^2 |x_2|^2 + x_1 |x_2|^4) e^{-j\omega n T} + \\ & (x_2 + x_2 |x_1|^2 + x_2 |x_2|^2 + x_2 |x_1|^4 + 4x_2 |x_1|^2 |x_2|^2 + x_2 |x_2|^4) e^{j\omega n T} + \\ & (x_1^2 x_2^* + 2x_1^2 |x_1|^2 x_2^* + 3x_1^2 |x_2|^2 x_2^*) e^{-3j\omega n T} + \\ & (x_1^* x_2^2 + 2x_1^* |x_2|^2 x_2^2 + 3x_1^* |x_1|^2 x_2^2) e^{3j\omega n T} + (x_1^3 x_2^{*2}) e^{-j5\omega n T} + \\ & (x_1^{*2} x_2^3) e^{j5\omega n T} \end{aligned} \quad (3.55)$$

To clarify,  $n$  in  $x_1(n)$  and  $x_2(n)$  is omitted to simplify the notations. If it is assumed that the frequency offset between the two carrier frequencies is large enough, the output signals around each carrier frequency can be approximated as:

$$\begin{aligned}
 y(-\omega) &= (x_1 + x_1 |x_1|^2 + x_1 |x_2|^2 + x_1 |x_1|^4 + x_1 |x_1|^2 |x_2|^2 + x_1 |x_2|^4) e^{-j\omega nT} \\
 & \quad (3.56)
 \end{aligned}$$

$$\begin{aligned}
 y(\omega) &= (x_2 + x_2 |x_1|^2 + x_2 |x_2|^2 + x_2 |x_1|^4 + x_2 |x_1|^2 |x_2|^2 + x_2 |x_2|^4) e^{j\omega nT} \\
 & \quad (3.57)
 \end{aligned}$$

For the nonlinear system with dual baseband complex input signals with  $N$ th-order nonlinearity and  $(M-1)$ th-order memory depth, the generalised formulations for each output complex signal associated with the each of the input signals are as follows:

$$\begin{aligned}
 y_1(n) &= \sum_{m=0}^{M-1} \sum_{k=0}^N \sum_{j=0}^k c_{k,j,m}^{(1)} x_1(n-m) |x_1(n-m)|^{k-j} x_2(n-m)^j \\
 & \quad (3.58)
 \end{aligned}$$

$$\begin{aligned}
 y_2(n) &= \sum_{m=0}^{M-1} \sum_{k=0}^N \sum_{j=0}^k c_{k,j,m}^{(2)} x_2(n-m) |x_1(n-m)|^{k-j} x_2(n-m)^j \\
 & \quad (3.59)
 \end{aligned}$$

Equations (3.58) and (3.59) can be developed in matrix form as

$$\vec{y} = A_x^{(i)} \vec{C} \quad (3.60)$$

where

- $\vec{y}_i = [y(n) \cdots y(n+L-1)]^T$  is an  $L \times 1$  vector representing the  $L$  samples of the output signal at  $i$ -th output;
- $\vec{C} = [c_{0,0,0}^{(i)} c_{1,0,0}^{(i)} c_{1,1,0}^{(i)} \cdots c_{i,j,0}^{(i)} \cdots c_{N,N,0}^{(i)} \cdots c_{N,N,M-1}^{(i)}]^T$  is a  $\left(\frac{1}{2}\right) \left(\frac{M(N+1)(N+2)}{2}\right) \times 1$  vector of polynomial coefficients;

•

$A_{\vec{x}}^{(i)} = [b_{\vec{x}_i}^{(0)} \dots b_{\vec{x}_i}^{(P)} \dots b_{\vec{x}_i}^{(M-1)}]$  is a  $L \times \left(\frac{M(N+1)(N+2)}{2}\right)$  matrix;

•  $b_{\vec{x}_i}^{(P)} =$

$$\begin{bmatrix} x_i(n-p) & x_i(n-p)|x_i(n-p)|^{k-j} |x_{ii}(n-p)|^j & x_i(n-p)|x_{ii}(n-p)|^N \\ \vdots & \vdots & \vdots \\ x_i(n-p+L-1) & x_i(n-p+L-1)|x_i(n-p+L-1)|^{k-j} |x_{ii}(n-p+L-1)|^j & x_i(n-p+L-1)|x_{ii}(n-p+L-1)|^N \end{bmatrix},$$

where  $i \& ii = 1, 2$  and  $i \neq ii$ , is a  $L \times \left(\frac{(N+1)(N+2)}{2}\right)$  matrix that has its elements extracted from (3.60);

•  $\vec{x} = [x(n) \dots x(n+L-1)]^T$  is an  $L \times 1$  vector

The 2-D DPD functions can be determined using the indirect learning architecture and least square to solve (3.60) when  $x$  and  $y$  are swapped. After this step, these functions are applied to initial signals as follows:

$$x_1(n) = \sum_{m=0}^{M-1} \sum_{k=0}^N \sum_{j=0}^k c_{k,j,m}^{(1)} z_1(n-m) |z_1(n-m)|^{k-j} |z_2(n-m)|^j \quad (3.61)$$

$$x_2(n) = \sum_{m=0}^{M-1} \sum_{k=0}^N \sum_{j=0}^k c_{k,j,m}^{(2)} z_2(n-m) |z_1(n-m)|^{k-j} |z_2(n-m)|^j \quad (3.62)$$

### 3.7.2. Low-complexity 2-D DPD

In order to simplify previously described model, the approach named 2-D DPD was developed [3.47]. For instance, if the seventh-order memoryless model

$$y = a_{10}^{(i)} x + a_{30}^{(i)} x |x|^2 + a_{50}^{(i)} x |x|^4 + a_{70}^{(i)} x |x|^6, \quad i = 1, 2 \quad (3.63)$$

is used, the output signals around each carrier frequency look like as follows:

$$y_1(n) = a_{10}^{(1)} x_1 + a_{30}^{(1)} x_1 (|x_1|^2 + 2|x_2|^2) + a_{50}^{(1)} x_1 (|x_1|^4 + 6|x_1|^2|x_2|^2 + 3|x_2|^4) + a_{70}^{(1)} x_1 (|x_1|^6 + 12|x_1|^4|x_2|^2 + 18|x_1|^2|x_2|^4 + 4|x_2|^6) \quad (3.64)$$

$$y_2(n) = a_{10}^{(2)} x_2 + a_{30}^{(2)} x_2 (|x_2|^2 + 2|x_1|^2) + a_{50}^{(2)} x_2 (|x_2|^4 + 6|x_2|^2|x_1|^2 + 3|x_1|^4) + a_{70}^{(2)} x_2 (|x_2|^6 + 12|x_2|^4|x_1|^2 + 18|x_2|^2|x_1|^4 + 4|x_1|^6) \quad (3.65)$$

where  $y_1(n)$  and  $y_2(n)$  are the complex baseband output signals around each carrier frequency, and  $n$  in  $x_1(n)$  and  $x_2(n)$  is omitted to simplify the notations. By including the memory terms, it leads to the model named low-complexity 2D model:

$$y_1(n) = \sum_{m=0}^{M-1} \sum_{k=0}^K h_{km}^{(1)} x_1(n-m) f_{k+1}(|x_1(n-m), x_2(n-m)|) \quad (3.66)$$

$$y_2(n) = \sum_{m=0}^{M-1} \sum_{k=0}^K h_{km}^{(2)} x_2(n-m) f_{k+1}(|x_2(n-m), x_1(n-m)|) \quad (3.67)$$

where  $h_{km}^{(1)}$  and  $h_{km}^{(2)}$  are the model coefficients of each band,  $M$  is the memory depth and  $K+1$  is the nonlinearity order. For odd-order terms (odd numbers of  $k+1$ ),  $f_{k+1}(|x_1(n-m), x_2(n-m)|)$  is derived from (3.64) and (3.65) and has the following form:

$$f_{k+1}(|x_i|, |x_j|) = \begin{cases} 1, & k=0 \\ |x_i|^2 + 2|x_j|^2, & k=2 \\ |x_i|^4 + 6|x_i|^2|x_j|^2 + 3|x_j|^4, & k=4 \\ |x_i|^6 + 12|x_i|^4|x_j|^2 + 18|x_i|^2|x_j|^4 + 4|x_j|^6, & k=6 \end{cases} \quad (3.68)$$

For even-order terms  $f_{k+1}(|x_1(n-m), x_2(n-m)|)$  can be simply written as:

$$f_{k+1}(|x_i|, |x_j|) = ||x_i| + |x_j||^k, \quad k = 1, 3, 5, \dots \quad (3.69)$$

where  $i, j \in 1, 2$  and  $i \neq j$ . This model can be also identified using least square algorithm. In comparison with previously described 2-D memory polynomials, this model uses two summations. The total number of coefficients is decreased from  $M(K + 1)(K + 2)$  to  $2M(K + 1)$ .

### 3.7.3. 2-D Augmented Hammerstein

As it is known, for the single-band case, the Hammerstein model consists of a static nonlinearity block cascaded by a linear FIR filter. A block diagram of the Hammerstein model for dual-band transmitters named 2-D Augmented Hammerstein model is depicted in Figure 3-11 [3.49].

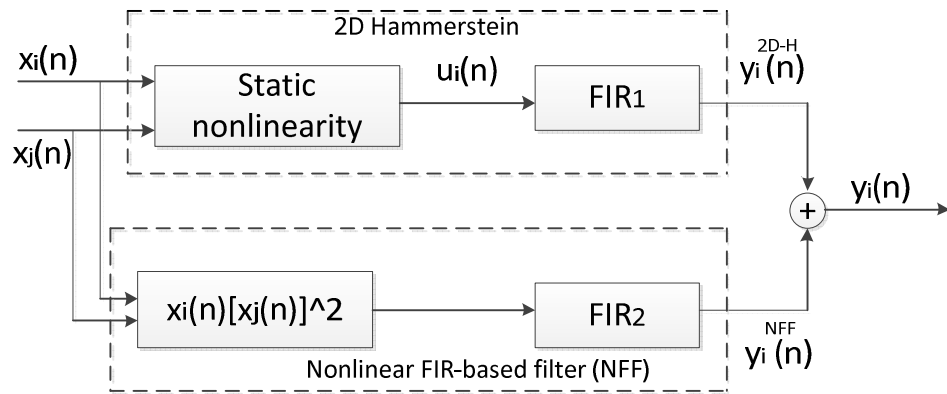


**Figure 3-11:** Block diagram of 2D augmented Hammerstein (2D-AH) model

As can be seen, the 2-D AH model consists of the 2-D Hammerstein model in parallel with nonlinear FIR-based filter (NFF). A 2-D Hammerstein model is described with following two equations:

$$u_i(n) = \sum_{k=0}^K \sum_{l=0}^k b_{kl}^{(i)} x_i(n) |x_i(n)|^{k-l} |x_j(n)|^l, \quad i, j \in \{1, 2\} \text{ and } i \neq j \quad (3.70)$$

$$y_i^{2D-H}(n) = \sum_{k=0}^K h_m^{(i)} u_i(n - m) \quad i, j \in \{1, 2\} \text{ and } i \neq j \quad (3.71)$$

The output signal of the NFF is given as follows:

$$y_i^{NFF} = \sum_{q=0}^{Q-1} g_q^{(i)} x_i(n-q) |x_j(n-q)|^2, \quad i, j \in \{1,2\} \text{ and } i \neq j \quad (3.72)$$

It should be noted that the NFF in (3.72) only considers the third-order nonlinear memory effect. Finally, the output of the 2-D AH model is sum of the (3.71) and (3.72):

$$y_i(n) = y_i^{2D-H}(n) + y_i^{NFF}(n), \quad i, j \in \{1,2\} \text{ and } i \neq j \quad (3.73)$$

#### 3.7.4. 2-D Enhanced Hammerstein

The Enhanced Hammerstein (EH) behavioural model consists of a memoryless polynomial followed by a Volterra filter [3.50]. Therefore, this model is capable to predict both the static nonlinearities and memory effects. The 2-D version of this model is expressed as follows:

$$u_1(n) = \sum_{k=1}^N \sum_{q=1}^k h_{k,q}^1 z_1(n) |z_1(n)|^{k-q} |z_2(n)|^{q-1} \quad (3.74)$$

$$u_2(n) = \sum_{k=1}^N \sum_{q=1}^k h_{k,q}^2 z_2(n) |z_1(n)|^{k-q} |z_2(n)|^{q-1} \quad (3.75)$$

where  $h_{k,q}^1$  and  $h_{k,q}^2$  are the kernels of the 2-D memoryless polynomials,  $z_1$  and  $z_2$  are the complex envelopes of the input signals of the PA at the carrier frequencies  $\omega_1$  and  $\omega_2$  and  $u_1$  and  $u_2$  are the complex envelopes of the output signals of the PA at the carrier frequencies  $\omega_1$  and  $\omega_2$ .  $N$  corresponds to the nonlinear order of the 2-D memoryless polynomials. The Volterra model is approximated by a simplified model as follows:

$$x_1(n) = \sum_{k=1}^P x_{1,k}(n) \quad (3.76)$$

where

$$x_{1,k}(n) = \begin{cases} \sum_{m_1=1}^{M_1} h_{m_1}^{(1,k)} u_1(n - m_1), & \text{for } k = 1 \\ \sum_{m_1=1}^{M_1} \sum_{m_2=1}^{M_2} \sum_{m_3=1}^{M_3} \sum_{q=1}^k h_{m_1, m_2, m_3}^{(1,k,q)} u_1(n - m_1) |u_1(n - m_2)|^{k-q} |u_2(n - m_3)|^{q-1}, & \text{for } k > 1 \end{cases} \quad (3.77)$$

and

$$x_2(n) = \sum_{k=1}^P x_{2,k}(n) \quad (3.78)$$

where

$$x_{2,k}(n) = \begin{cases} \sum_{m_1=1}^{M_1} h_{m_1}^{(2,k)} u_2(n - m_1), & \text{for } k = 1 \\ \sum_{m_1=1}^{M_1} \sum_{m_2=1}^{M_2} \sum_{m_3=1}^{M_3} \sum_{q=1}^k h_{m_1, m_2, m_3}^{(2,k,q)} u_2(n - m_1) |u_1(n - m_2)|^{k-q} |u_2(n - m_3)|^{q-1}, & \text{for } k > 1 \end{cases} \quad (3.79)$$

### 3.7.5. Dual-band DPD Based on Look-up-tables

A single band LUT model can be implemented efficiently as

$$y(n) = \sum_{q=0}^{Q-1} x(n - q) LUT_q[|x(n - q)|^2] \quad (3.80)$$

where the term  $\sum_{k=0}^{K-1} a_{2k+1,q} |x(n - q)|^{2k}$  used in conventional memory polynomial model is swapped by  $LUT_q[|x(n - q)|^2]$ . This model can be extended to be applicable in dual-band transmitters [3.51]. In that case, the output signal at Band 1 looks like:

$$y_1(n) = \sum_{q=0}^{Q-1} x_1(n-q) LUT_{1q}[|x_1(n-q)|^2, |x_2(n-q)|^2] \quad (3.81)$$

Two-dimensional LUTs are required here to represent all the product terms between  $|x_1(n-q)|^2$  and  $|x_2(n-q)|^2$  in (3.81). This leads to the high complexity of real-life implementation. However, this model can be simplified as follows:

$$y_1(n) = \sum_{q=0}^{Q-1} x_1(n-q) \{LUT_{1q}[|x_1(n-q)|^2] + LUT_{2q}[|x_2(n-q)|^2]\} \quad (3.82)$$

or

$$y_1(n) = \sum_{q=0}^{Q-1} x_1(n-q) \{LUT_{1q}[|x_1(n-q)|^2] + LUT_{2q}[|x_1(n-q)|^2 + |x_2(n-q)|^2]\} \quad (3.83)$$

The LUT-based 2-D DPD structure (3.83) is more accurate than the structure (3.82), but more complex and therefore, less efficient [3.51].

### 3.7.6. Extended-RVFTDNN for Dual-band Transmitters

An extended real-valued focused time-delay neural network (extended-RVFTDNN) was proposed to approximate the nonlinear behaviour of concurrent dual-band transmitters [3.52]. The topology of extended-RVFTDNN is illustrated in Figure 3-12. One can see that two single-band RVTDNNs are combined with mutual coupling; thus, the conventional ANN model is extended to a new neural network with four inputs and four outputs. Therefore, the outputs of this extended-RVFTDNN are all functions of the two input signals:

$$\begin{aligned} I_{out1}(n) = g_1[ & I_{in1}(n), I_{in1}(n-1), \dots, I_{in1}(n-p_1); Q_{in1}(n), \dots, Q_{in1}(n-q_1) \\ & I_{in2}(n), I_{in2}(n-1), \dots, I_{in2}(n-p_2); Q_{in2}(n), Q_{in2}(n-1), \dots, Q_{in2}(n-q_1) ] \end{aligned} \quad (3.84)$$

$$Q_{out1}(n) = g_2 [I_{in1}(n), I_{in1}(n-1), \dots, I_{in1}(n-p_1); Q_{in1}(n), \dots, Q_{in1}(n-q_1) \\ I_{in2}(n), I_{in2}(n-1), \dots, I_{in2}(n-p_2); Q_{in2}(n), Q_{in2}(n-1), \dots, Q_{in2}(n-q_1)] \quad (3.85)$$

$$I_{out2}(n) = g_3 [I_{in1}(n), I_{in1}(n-1), \dots, I_{in1}(n-p_1); Q_{in1}(n), \dots, Q_{in1}(n-q_1) \\ I_{in2}(n), I_{in2}(n-1), \dots, I_{in2}(n-p_2); Q_{in2}(n), Q_{in2}(n-1), \dots, Q_{in2}(n-q_1)] \quad (3.86)$$

$$Q_{out2}(n) = g_4 [I_{in1}(n), I_{in1}(n-1), \dots, I_{in1}(n-p_1); Q_{in1}(n), \dots, Q_{in1}(n-q_1) \\ I_{in2}(n), I_{in2}(n-1), \dots, I_{in2}(n-p_2); Q_{in2}(n), Q_{in2}(n-1), \dots, Q_{in2}(n-q_1)] \quad (3.87)$$

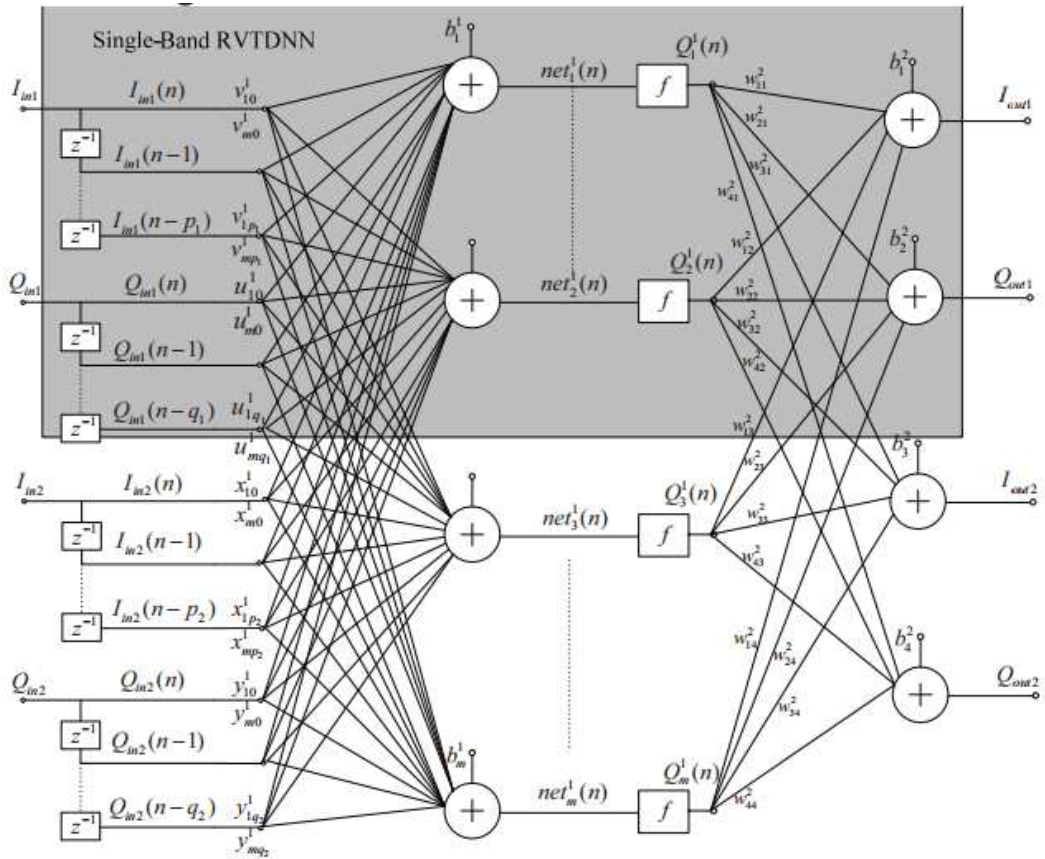


**Figure 3-12:** The topology of extended-RVFTDNN for concurrent dual-band behavioural modelling [3.52]

Due to the coupling of two single-band ANNs, the modelling of cross-modulation products as a result of the two input signals is automatically integrated into the ANN.

The four ANN outputs can be expressed as:

$$I_{out(i+1)} = \sum_{k=1}^m w_{(2i+1)k}^2 Q_k^1(n) + b_{2i+1}^2, \quad i = 0,1 \quad (3.88)$$

$$Q_{out(i+1)} = \sum_{k=1}^m w_{(2i+2)k}^2 Q_k^1(n) + b_{2i+2}^2, \quad i = 0,1 \quad (3.89)$$

where

$$Q_k^1(n) = f(\text{net}_k^1(n)) \quad k = 1,2,3, \dots, m \quad (3.90)$$

and

$$\begin{aligned} \text{net}_k^1(n) = & \sum_{i=0}^{p_1} v_{ki}^1 I_{in1}(n-i) + \sum_{i=0}^{q_1} u_{ki}^1 Q_{in1}(n-i) + \sum_{i=0}^{p_2} x_{ki}^1 I_{in2}(n-i) \\ & + \sum_{i=0}^{q_2} y_{ki}^1 Q_{in2}(n-i) + b_k^1 \end{aligned} \quad (3.91)$$

As in the RVFTDNN case [3.28], the chosen activation function for the hidden layer and the training algorithm was the *tansig* and Levenberg-Marquart (LM), respectively [3.52].

### 3.8. Band-limited Digital Predistortion

The constantly increasing demands for wide bandwidth create great difficulties in employing DPD in future ultra-wideband systems. This is mainly because the existing DPD system requires multiple times the input signal bandwidth in the transmitter and receiver chain, which is impractical to implement in practice. For instance, in the extremely wideband system such as LTE-Advanced, 100-MHz modulation bandwidth is required, which means that 500-MHz linearisation bandwidth will be required if the existing DPD techniques are utilised. Therefore, there is a new need for band-limited DPD research and development. This section describes pioneer

DPD technique in this direction [3.53]. A band-limiting function is inserted into the general Volterra operators in the DPD model to control the signal bandwidth under modelling, which logically transforms the general Volterra series-based model into a band-limited version. This approach eliminates the system bandwidth constraints of the conventional DPD techniques. It allows users to arbitrarily select the bandwidth to be linearised in the PA output according to the system requirements without sacrificing performances.

As shown in Figure 3-13, a band-limiting function is cascaded with the Volterra operator.

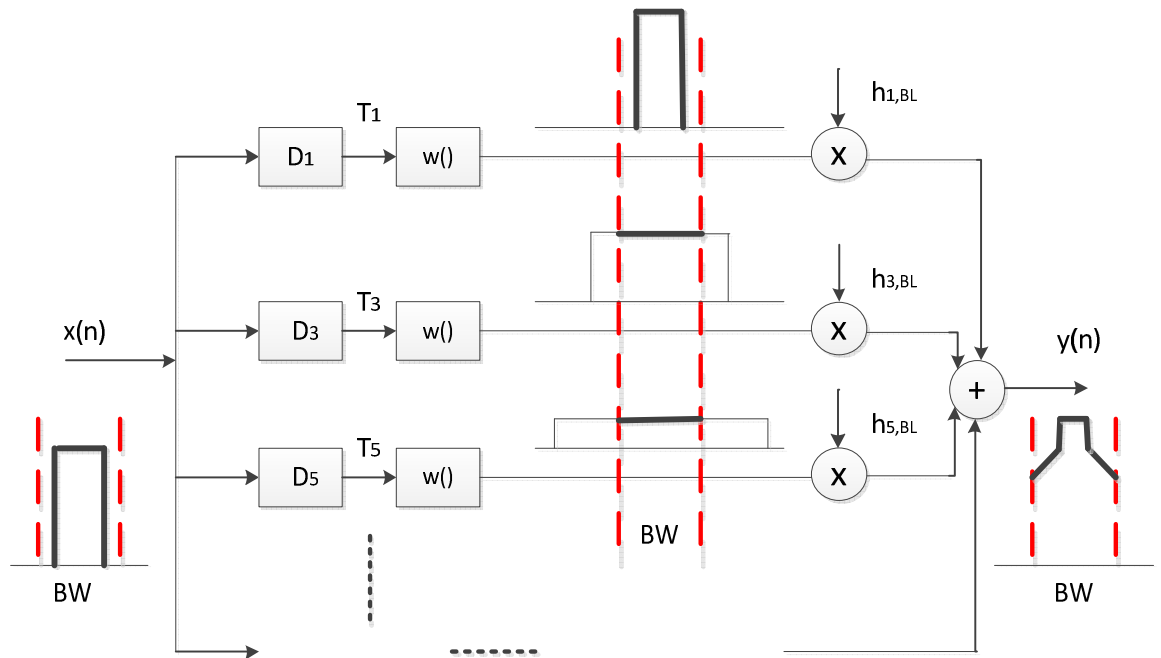


**Figure 3-13:** Band-limited Volterra series model

It was mentioned previously that the conventional Volterra model is represented as:

$$y(n) = \sum_{p=1}^{\infty} \sum_{i_1=0}^{\infty} \cdots \sum_{i_p=0}^{\infty} h_p(i_1, \dots, i_p) D_p[x(n)] \quad (3.92)$$

where

$$D_p[x(n)] = \prod_{j=1}^p x(n - i_j) \quad (3.93)$$

The band-limiting function can be a linear filter, and it can be predesigned in the frequency domain with an effective bandwidth chosen according to the bandwidth requirement of the system output. It is then converted into the time domain and represented by a finite impulse response. The  $p$ th-order band-limited Volterra operator can be represented by

$$T_p[x(n)] = D_p[x(n)] * w(n) \quad (3.94)$$

where  $*$  represents the convolution operation. The general Volterra series can thus be transformed into a band-limited version as

$$\begin{aligned} y(n) &= \sum_{p=1}^{\infty} \sum_{i_1=0}^{\infty} \cdots \sum_{i_p=0}^{\infty} h_{p,BL}(i_1, \dots, i_p) T_p[x(n)] = \\ &= \sum_{p=1}^{\infty} \sum_{i_1=0}^{\infty} \cdots \sum_{i_p=0}^{\infty} h_{p,BL}(i_1, \dots, i_p) \{D_p[x(n)] * w(n)\} = \\ &= \sum_{p=1}^{\infty} \sum_{i_1=0}^{\infty} \cdots \sum_{i_p=0}^{\infty} h_{p,BL}(i_1, \dots, i_p) \\ &\quad \times \left\{ \sum_{k=0}^K \left[ \prod_{j=1}^p x(n - i_j - k) w(k) \right] \right\} \end{aligned} \quad (3.95),$$

where  $T_p$  is the  $p$ th-order band-limited Volterra operator,  $w(n)$  is the band-limiting function with length  $K$ ,  $h_{p,BL}(i_1, \dots, i_p)$  is the  $p$ th-order band-limited Volterra kernel, and  $x(n)$  and  $y(n)$  represent the input and output signals, respectively. Due to the fact that the signal is filtered by the band-limiting function after it passes each Volterra operator, the bandwidth of the output from each Volterra operator is limited within a certain frequency range (BW in Figure 3-13). After being linearly scaled by the coefficients and recombined together, the final output is logically band-limited to BW [3.53].

### 3.9. Conclusion

First of all, an overview of existing PA behavioural models and DPD techniques based on these models has been presented in this Chapter. In fact, the previously proposed DPDs do not require additional RF components and can be considered as being simple in implementation and integration. However, these Volterra, LUT, polynomial and ANN-based DPD techniques have high DSP computational complexity as well as high complexity and numerical instability of DPD model identification. Second, the DPD techniques applicable in dual-input MIMO transmitters as well as in concurrent-dual band transmitters were described. The complexity of these DPDs is additionally increased and their implementation in real transmitters is impractical. A high bandwidth constraints problem was discussed and band-limited DPD used to mitigate these constraints was presented. This thesis is focused on overcoming numerous problems of existing DPD solutions in modern wireless transmitters' applications.

### 3.10. References

- [3.1] L. Ding, G. T. Zhou, D. R. Morgan, Z. Ma, J. S. Kenney, J. Kim, and C. R. Giardina, "A robust digital baseband predistorter constructed using memory polynomials," *IEEE Trans. Commun.*, vol. 52, no. 1, pp. 159–165, Jan. 2004.
- [3.2] S. Hong, Y. Y. Woo, J. Kim, I. Kim, J. Cha, I. Kim, J. Moon, J. Yi, and B. Kim, "Weighted polynomial digital predistortion for low memory effect Doherty power amplifier," *IEEE Trans. Microw. Theory Tech.*, vol. 55, no. 5, pp. 925–931, May 2007.
- [3.3] J. Kim, Y. Y. Woo, J. Moon, and B. Kim, "A new wideband adaptive digital predistortion technique employing feedback linearization," *IEEE Trans. Microw. Theory Tech.*, vol. 56, no. 2, pp. 385–392, Feb. 2008.

- [3.4] C. Eun and E. J. Powers, "A new Volterra predistorter based on the indirect learning architecture," *IEEE Trans. Signal Process.*, vol. 45, no. 1, pp. 223–227, Jan. 1997.
- [3.5] A. Zhu, J. C. Pedro, and T. J. Brazil, "Dynamic deviation reduction-based behavioral modeling of RF power amplifiers," *IEEE Trans. Microw. Theory Tech.*, vol. 54, no. 12, pp. 4323–4332, Dec. 2006.
- [3.6] D. Morgan, Z. Ma, J. Kim, M. Zierdt, and J. Pastalan, "A generalized memory polynomial model for digital predistortion of RF power amplifiers," *IEEE Trans. Signal Process.*, vol. 54, pp. 3852–3860, Oct. 2006.
- [3.7] J. Kim and K. Konstantinou, "Digital predistortion of wideband signals based on power amplifier model with memory," *Electron. Lett.*, vol. 37, no. 23, pp. 1417–1418, Nov. 2001.
- [3.8] A. Zhu, P. J. Draxler, J. J. Yan, T. J. Brazil, D. F. Kimball, and P. M. Asbeck, "Open-loop digital predistorter for RF power amplifiers using dynamic deviation reduction-based Volterra series," *IEEE Trans. Microw. Theory Tech.*, vol. 56, no. 7, pp. 1524–1534, July 2008.
- [3.9] F. M. Ghannouchi, and O. Hammi, „Behavioral modeling and predistortion," *IEEE Microw. Mag.*, vol.10, no.7, pp.52-64, Dec. 2009.
- [3.10] D. Schreurs, M. O’Droma, A. A. Goacher, and M. Gadringer, "RF Power Amplifier Behavioral Modeling", New York, NY: Cambridge Univ. Press, 2008.
- [3.11] H. Ku and I. S. Kenney, „Behavioral Modeling of Nonlinear RF Power Amplifiers Considering Memory Effects," *IEEE Trans. Microwave Theory Tech.*, vol. 51, pp. 2495-2504, 2003.
- [3.12] M. Isaksson, D. Wisell, and D. Rönnow, „A Comparative Analysis of Behavioral Models for RF Power Amplifiers," *IEEE Trans. Microw. Theory Tech.*, vol. 54, no. 1, Jan. 2006.

- [3.13] J. C. Pedro and S. A. Maas, "A comparative overview of microwave and wireless power-amplifier behavioral modeling approaches," *IEEE Trans. Microw. Theory Tech.*, vol. 53, no. 4, pp. 1150–1163, Apr. 2005.
- [3.14] J. K. Cavers, "Amplifier linearization using a digital predistorter with fast adaptation and low memory requirements," *IEEE Trans. Veh. Technol.*, vol. 39, no. 4, pp. 374–382, Nov. 1990.
- [3.15] A. Zhu, J. Pedro, and T. Cunha, "Pruning the Volterra series for behavioral modeling of power amplifiers using physical knowledge," *IEEE Trans. Microw. Theory Tech.*, vol. 55, no. 5, pp. 813–821, May 2007.
- [3.16] R. Raich, H. Qian, and G. T. Zhou, "Orthogonal polynomials for power amplifier modeling and predistorter design," *IEEE Trans. Veh. Technol.*, vol. 53, pp. 1468–1479, Sept. 2004.
- [3.17] Haiying Cao "Linearization of High Efficiency Transmitters for wireless Communications", PhD thesis, Chalmers University of Technology, 2009.
- [3.18] A. Bernardini and S. D. Fina, "Analysis of different optimization criteria for IF predistortion in digital radio links with nonlinear amplifiers," *IEEE Trans. Commun.*, vol. 45, no. 4, pp. 421-428, Apr. 1997.
- [3.19] G. Lazzarin, S. Pupolin, and A. Sarti, "Nonlinearity compensation in digital radio systems," *IEEE Trans. Commun.*, vol. 42, no. 2, pp. 988-999, Feb. 1994.
- [3.20] Y. H. Lim, Y. S. Cho, I. W. Cha, and D. H. Youn, "An adaptive nonlinear prefilter for compensation of distortion in nonlinear systems," *IEEE Trans. Signal Process.*, vol. 46, no. 6, pp. 1726-1730, Jun. 1998.
- [3.21] D. Zhou and V. E. DeBrunner, "Novel adaptive nonlinear predistorters based on the direct learning algorithm," *IEEE Trans. Signal Process.*, vol. 55, no. 1, pp. 120–133, Jan. 2007.
- [3.22] H. Paaso and A. Mammela, "Comparison of Direct Learning and Indirect Learning Predistortion Architectures", in *IEEE Int. Symp. on Wireless Commun. Systems*, pp. 309-313, Oct. 2008.

- [3.23] R. Marsalek, P. Jardin, and G. Baudoin, "From post-distortion to predistortion for power amplifiers linearization," *IEEE Commun. Lett.*, vol. 7, no. 7, pp. 308–310, Jul. 2003.
- [3.24] M. Abi Hussein, V. A. Bohara, and O. Venard, "On the system level convergence of ila and dla for digital predistortion," in *2012 Intern. Symp. on Wireless Commun. Systems (ISWCS)*, pp. 870–874, Aug. 2012.
- [3.25] L. Anttila, P. Handel, and M. Valkama, "Joint mitigation of power amplifier and I/Q modulator impairments in broadband direct-conversion transmitters," *IEEE Trans. Microw. Theory Tech.*, vol. 58, no. 4, pp. 730–739, Apr. 2010.
- [3.26] S. Haykin, "Neural Networks: A Comprehensive Foundation." Upper Saddle River, NJ: Prentice-Hall, 1999.
- [3.27] M. H. Hassoun, "Fundamentals of Artificial Neural Networks", MIT Press, 1995.
- [3.28] M. Rawat, K. Rawat, and F. M. Ghannouchi, "Adaptive digital predistortion of wireless power amplifiers/transmitters using dynamic real-valued focused time-delay line neural networks," *IEEE Trans. Microw. Theory Tech.*, vol. 58, no. 1, pp. 95–104, Jan. 2010.
- [3.29] F. Mkadem and S. Boumaiza, "Physically inspired neural network model for RF power amplifier behavioral modeling and digital pre-distortion," *IEEE Trans. Microw. Theory Tech.*, vol. 59, no. 4, pp. 913–923, Apr. 2011.
- [3.30] Y.-D. Kim, E.-R. Jeong and Y. H. Lee, "Adaptive Compensation for Power Amplifier Nonlinearity in the Presence of Quadrature Modulation/Demodulation Errors," *IEEE Trans. Signal Process.*, vol. 55, no. 9, pp. 4717–4721, Sep. 2007.
- [3.31] S. Ahn, S. Choi, E. Jeong, and Y. Lee, "Compensation for Power Amplifier Nonlinearity in the Presence of Local Oscillator Coupling Effects," *IEEE Commun. Lett.*, vol. 16, no. 5, pp. 600–603, May 2012.
- [3.32] S.A. Bassam, M. Helaoui, and F.M. Ghannouchi, "Crossover Digital Predistorter for the Compensation of Crosstalk and Nonlinearity in MIMO

- Transmitters," *IEEE Trans. Microw. Theory Tech.*, vol. 57, no. 5, pp. 1119-1128, May 2009.
- [3.33] T. Sadeghpour, R.A. Alhameed, N.T. Ali, I. T. E. Elfergani, Y. Dama, and O. O. Anoh, "Linear and nonlinear crosstalk in MIMO OFDM transceivers," in *Proc. IEEE 18th Int. Conf. on Electronics, Circuits and Systems (ICECS)*, vol., no., pp.504-507, Dec. 2011.
- [3.34] S. Choi, and E. Jeong, "Digital Predistortion Based on Combined Feedback for MIMO transmitters," *IEEE Commun. Lett.*, vol. 16, no. 10, pp. 1572-1575, Oct. 2012.
- [3.35] **M. Cabarkapa**, M. Bozic, N. Neskovic, A. Neskovic and D. Budimir, "Compensation of Undesired Effects in MIMO Wireless Transceivers", *IEEE International Symposium on Antennas and Propagation and CNC/USNC/URSI National Radio Science Meeting (APS2012)*, pp. 1-2, July 8-14, 2012, Chicago, Illinois, USA.
- [3.36] **M. Cabarkapa**, N. Neskovic, and D. Budimir, "Crosstalk Suppression in Spatially Multiplexed MIMO OFDM Wireless Transmitters", [*in preparation*].
- [3.37] N. Mizusawa, and S. Kusunoki, "Third- and fifth-order baseband component injection for linearization of the power amplifier in a cellular phone," *IEEE Trans. Microw. Theory Tech.*, vol. 53, no. 4, pp. 3327-3334, April 2005.
- [3.38] G. H. Golub and C. F. Van Loan, "Matrix Computations," 3rd ed. London, U.K.: The Johns Hopkins Univ. Press, 1996.
- [3.39] S. Haykin, "Adaptive Filter Theory," 4th ed. Upper Saddle River, NJ: Prentice-Hall, 2002.
- [3.40] M. Helaoui, S. Boumaiza, A. Ghazel, and F. M. Ghannouchi, "Power and efficiency enhancement of 3G multi-carrier amplifiers using digital signal processing with experimental validation," *IEEE Trans. Microw. Theory Tech.*, vol. 54, no. 4, pp. 1396-1404, Apr. 2006.

- [3.41] S.A. Bassam, M. Helaoui, and F.M. Ghannouchi, "2-D digital predistortion (2-D-DPD) architecture for concurrent dual-band transmitters," *IEEE Trans. Microw. Theory Tech.*, vol.59, no.10, pp.2547-2553, Oct. 2011.
- [3.42] J. Kim, P. Roblin, D. Chaillot, and Z. Xie, "A generalized architecture for the frequency-selective digital predistortion linearization technique," *IEEE Trans. Microw. Theory Tech.*, vol.61, no.1, pp.596-605, Jan. 2013.
- [3.43] A. Cidronali, I. Magrini, R. Fagotti, and G. Manes, "A new approach for concurrent dual-band IF digital predistortion: System design and analysis," in *Proc. Integr. Nonlinear Microw. Millimetre-Wave Circ. Workshop*, Malaga, Spain, pp. 127–130, Nov. 2008.
- [3.44] R. N. Braithwaite, "Digital predistortion of a power amplifier for signals comprising widely spaced carriers," in *Proc. 78th Microw. Meas. Symp.*, pp. 1–4, 2011.
- [3.45] S.A. Bassam, W. Chen; M. Helaoui, F.M. Ghannouchi , and Z. Feng, "Linearization of concurrent dual-band power amplifier based on 2D-DPD technique," *IEEE Microw. Wireless Comp. Lett.*, vol.21, no.12, pp.685-687, Dec. 2011.
- [3.46] S. A. Bassam, A. Kwan, W. Chen, M. Helaoui, and F. M. Ghannouchi, "Subsampling feedback loop applicable to concurrent dual-band linearization architecture," *IEEE Trans. Microw. Theory Tech.*, vol. 60, no. 6, pp. 1990–1999, Jun. 2012.
- [3.47] Y.-J. Liu, J. Zhou, W. Chen, B. Zhou, and F.M. Ghannouchi, "Low-complexity 2D behavioural model for concurrent dual-band power amplifiers," *Electron. Lett.*, vol.48, no.11, pp.620-621, May 2012.
- [3.48] Y.-Jiang Liu, W. Chen, J. Zhou, B.-Hua Zhou, and F. Ghannouchi, "Digital predistortion for concurrent dual-band transmitters using 2-D modified memory polynomials," *IEEE Trans. Microw. Theory Tech.*, vol.61, no.1, pp.281-290, Jan. 2013.

- [3.49] Y.-J. Liu, W. Chen, B. Zhou, J. Zhou, and F.M. Ghannouchi, "2D augmented Hammerstein model for concurrent dual-band power amplifiers," *Electron. Lett.*, vol.48, no.19, pp.1214-1216, Sept. 2012.
- [3.50] J. Moon, P. Saad, J. Son, C. Fager, and B. Kim "2-D enhanced Hammerstein behavior model for concurrent dual-band power amplifiers", in *Proc. 42th Eur. Microw. Conf.*, pp. 1249-1252, Oct. 2012.
- [3.51] L. Ding, Z. G. Yang, and H. Gandhi, "Concurrent dual-band digital predistortion", in *IEEE MTT-S Int. Microw. Symp. Dig.*, pp.1-3, June 2012.
- [3.52] Z. Huang, W. Chen, Z. Feng, and F.M. Ghannouchi, "Forward behavioral modeling of concurrent dual-band power amplifiers using extended real valued time delay neural networks," in *Int. Microw. Millim. Wave Tech. (ICMMT) Conf.*, pp.1-4, May 2012.
- [3.53] C. Yu, L. Guan, E. Zhu, and A. Zhu, "Band-limited volterra series based predistortion for wideband RF power amplifiers," *IEEE Trans. Microw. Theory Tech.*, vol. 60, no. 12, pp. 4198–4208, Dec. 2012.

## 4. Injection-based Linearisation Techniques

### 4.1. Introduction

The linearisation methods based on injection were developed in [4.1]-[4.10]. For injection-based RF predistortion methods, the authors used second harmonic injection [4.1]- [4.3], frequency difference injection [4.2], [4.4], [4.5], low-frequency even-order intermodulation (IM) components injection [4.6], a combined second harmonic and frequency difference injection [4.7], a combined IM3 and envelope injection [4.8], a combined low frequency difference and third harmonic injection [4.9] or a combined RF-baseband injection [4.10]. The shortcoming of [4.1]-[4.10] is the adding of additional RF hardware components. Quite the opposite, the third-order IM component injection [4.11], the third- and fifth- order IM components injection [4.12], a brick wall injection [4.13], a combined LUT-injection [4.14] or an iterative injection [4.15] were proposed to be implemented as DPD. In general, these predistorters have significantly lower computational complexity in comparison with other DPD approaches based on Volterra, LUT, polynomials or ANN described in previous Chapter.

Nonetheless, they usually suffer from compensation limit introduced by new components that appear after injections [4.12]. Moreover, the existing injection-based techniques were tested in open loop and due to that fact, are not adaptive and have limited usage in real transmitters. In addition, there was no experimental proof of how these techniques behave with 4G signals which have very variable amplitude. Furthermore, as will be shown in this thesis, the mentioned injection-based DPDs cannot be used in concurrent dual-band transmitters because of their impractical sampling rate requirements for the digital-to-analogue convertors (DAC). Also, all they have limited error vector magnitude (EVM) and power spectrum density (PSD) performance due to the fact that the distortion caused by cross-modulation (CM) products is not taken into consideration.

To sum up, the injection-based DPD methodology has a potential of achieving high linearising performance, while maintaining relatively low complexity. For this

reason, this methodology is assumed as a basis for the advanced DPD techniques for modern wireless transmitters developed in this thesis.

## 4.2. RF Injection Techniques

The mostly used RF injection techniques use an injection of the distortion products generated by the second-order nonlinearity of the PA, which are either the difference frequency component or the second harmonic of the nonlinear PA output [4.1]-[4.5]. If these products are mixed with the initial signal, they can improve the intermodulation distortion (IMD) of the PA. Under a two-tone test, the difference frequency component is the one containing  $\cos(\omega_1 - \omega_2) t$ , which after being mixed with the fundamental-frequency signal at  $\cos(\omega_1 t)$  produces an additional IMD component at  $\cos(2\omega_1 - \omega_2) t$ . If the phase shift is carefully selected, this added IMD component can decrease the initial one, and hence improve PA linearity. Similarly, the second harmonic at  $\cos(2\omega_1 t)$  after mixing with the fundamental harmonic at  $\cos(\omega_2 t)$  generates an IMD term at  $\cos(2\omega_1 - \omega_2) t$ . This component interferes with the IMD term produced by the amplifier's nonlinearity, and, if the phase is adjusted properly, decreases it. Consequently, the second-order products injection techniques are divided into two groups: second-harmonic and difference-frequency injection techniques.

### 4.2.1. Second Harmonic Injection

The general block diagram illustrating operation of the second-order products injection technique is presented in Figure 4-1.

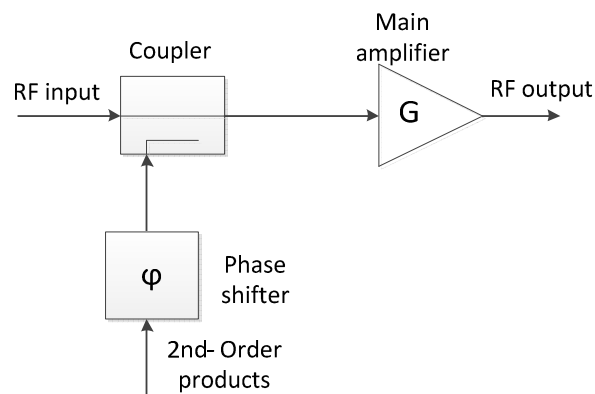


**Figure 4-1:** Second-order products injection system

The output voltage  $V_{out}(t)$  of the PA can be represented by the power series of the input voltage  $V_{IN}(t)$ :

$$V_{out}(t) = g_1 V_{IN}(t) + g_2 V_{IN}^2(t) + g_3 V_{IN}^3. \quad (4.1)$$

For a two-tone input signal, given by

$$V_{IN}(t) = V \cdot (\cos(\omega_1 t) + \cos(\omega_2 t)), \quad (4.2)$$

the analytical expression for the IM3 component, obtained by substituting of (4.2) into (4.1) and completing trigonometric transformations, looks like:

$$V_{IM3}(t) = \frac{3}{4} g_3 V^3 [(\cos(2\omega_1 - \omega_2) t) + (\cos(2\omega_2 - \omega_1) t)] \quad (4.3)$$

In the obtained expression each summand represents an IM3 component placed on either side of the output signal. If second harmonics at  $2\omega_2$  and  $2\omega_1$  are injected, the input signal may be re-written as:

$$V_{IN}(t) = V_1 \cdot (\cos(\omega_1 t) + \cos(\omega_2 t)) + V_2 (\cos(2\omega_1 t + \varphi_1) + \cos(2\omega_2 t + \varphi_2)) \quad (4.4)$$

where  $\varphi_1$  and  $\varphi_2$  are the corresponding phase shifts. By substituting (4.4) into the expression (4.1), the new IM3 is obtained:

$$\begin{aligned} V_{IM3}(t) = & \frac{3}{4} \cdot g_3 \cdot V_1^3 [(\cos((2\omega_1 - \omega_2) t) + (\cos((2\omega_2 - \omega_1) t))] \\ & + g_2 V_1 \cdot V_2 [(\cos((2\omega_1 - \omega_2) t + \varphi_1) + (\cos((2\omega_2 - \omega_1) t + \varphi_2))] \\ & + \frac{3}{2} \cdot g_3 \cdot V_1 \cdot V_2^2 [(\cos((2\omega_1 - \omega_2) t + \varphi_1 - \varphi_2) + (\cos((2\omega_2 - \omega_1) t + \varphi_2 - \varphi_1))] \end{aligned} \quad (4.5)$$

The derived expression contains the new IM3 components, which can influence the original one. If the phase shifts are  $\varphi_1 = \varphi_2 = 180^\circ$  and the magnitude of the injected second harmonic is adjusted as:

$$V_2 = \frac{3g_3}{4g_2} V_1^2 \quad (4.6),$$

the IM3 is reduced. The linearisation performances are limited by the third term in (4.5) as well as the accuracy of practical gain and phase adjustments that are done into RF. The source of the second-order injected products can be a feedback chain of the PA [4.16], as shown in Figure 4-2.

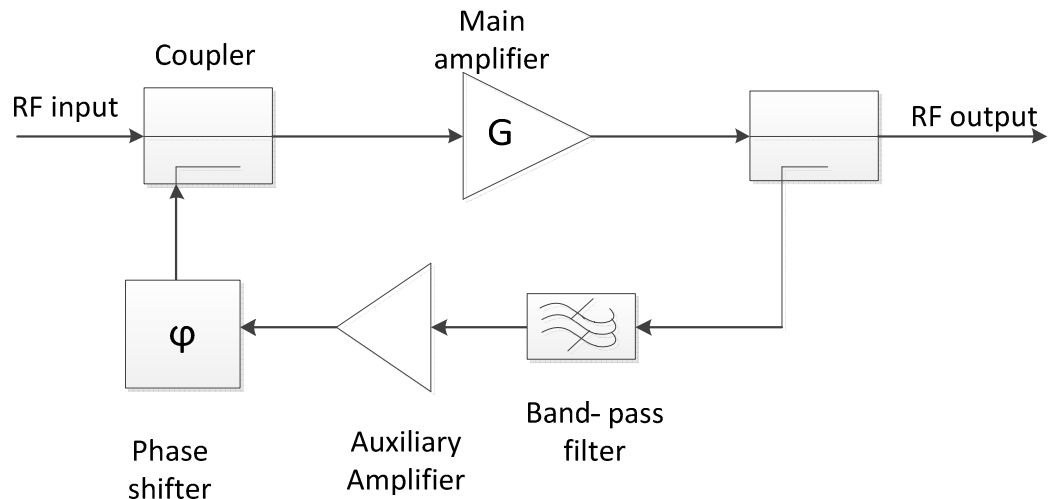


**Figure 4-2:** Feedback-based second-order products injection circuit

In Figure 4-2, the band-pass filter is used to select the necessary injected component, auxiliary amplifier acts as a gain controller in order to achieve the proper relation between the amplitudes of the fundamental signal and the injected signal, and the phase shifter controls the phase of the injected IM3 to be opposite to the original one produced by the main PA. The benefit of using such a system is its simplicity of implementation. In contrast, the inability to linearise a wideband PA is its main disadvantage [4.16]. This is because the signals with large frequency differences cause large phase differences in the created IMD products. Consequently, it is difficult to adjust the phase of the injected signals and the injected IMD components do not have a 180-degree phase shift. In order to avoid the mentioned problem, the injected signals can be obtained from other external resource instead from a feedback loop. For instance, they can be generated by another nonlinear component, which precedes the PA [4.3], [4.16].

#### 4.2.2. Frequency Deference Injection

If a difference-frequency component at  $\omega_1 - \omega_2$  is injected into the fundamental one, the input signal may be written as:

$$V_{IN}(t) = V_1 \cdot (\cos(\omega_1 t) + \cos(\omega_2 t)) + V_2 \cdot (\cos(\omega_2 - \omega_1)t + \varphi) \quad (4.7)$$

where  $\varphi$  is the phase of the phase shifter. Substituting of (4.7) into (4.1) and completing trigonometric transformations gives the expression for the new IM3 products:

$$\begin{aligned} V_{IM3}(t) = & \frac{3}{4} \cdot g_3 \cdot V_1^3 [\cos((2\omega_1 - \omega_2)t) + \cos((2\omega_2 - \omega_1)t)] \\ & + g_2 \cdot V_1 \cdot V_2 [\cos((2\omega_1 - \omega_2)t - \varphi) + \cos((2\omega_2 - \omega_1)t + \varphi)] \\ & + \frac{3}{2} \cdot g_3 \cdot V_1 \cdot V_2^2 [\cos((2\omega_1 - \omega_2)t - 2\varphi) + \cos((2\omega_2 - \omega_1)t + 2\varphi)]. \end{aligned} \quad (4.8)$$

From the obtained expression one can see that the injected difference-frequency component results in the appearance of the new IM3 terms at the output. In (4.8), the first line represents the primary IM3 produced by the PA whereas the second line represents the additional IM3 components obtained as a result of mixing the initial signal with the difference-frequency distortion product. If the phase of the phase shift are  $\varphi = 180^\circ$ , and the magnitude of the injected component is adjusted as

$$V_2 = \frac{3g_3}{4g_2} V_1^2, \quad (4.9)$$

the terms in the first and second line of (4.8) will compensate each other. One can see this is the same expression of adjusted amplitude as in (4.6) for second harmonic injection. However, the last line in (4.8) contains the components which limit the performance of this frequency deference predistortion system. They are smaller than the original IMD and have a minor effect when the PA works into high back-off region. However, they significantly degrade the difference-frequency predistortion performance when the PA operates into high compression region [4.2], [4.16]. Moreover, the practical implementation has a problem to control the magnitude and phase adjustments, and thus the overall expected linearity is deteriorated. This is a result of the imperfections of the circuits' realisation.

### 4.2.3. Combined Frequency Deference and Second Harmonic Injection

Figure 4-3 shows the block diagram of the approach used in [4.7]. The predistorter consists of three paths: linear path, nonlinear path I and nonlinear path II. When two signals at frequencies  $\omega_1$  and  $\omega_2$ , with respective amplitudes  $A_1$  and  $A_2$ , is applied at the input of the RF predistorter, the output signal can be written as shown in (4.10)

$$x_1(t) = A_1 \cos(\omega_1 t + \phi_1) + A_2 \cos(\omega_2 t + \phi_2) \quad (4.10)$$

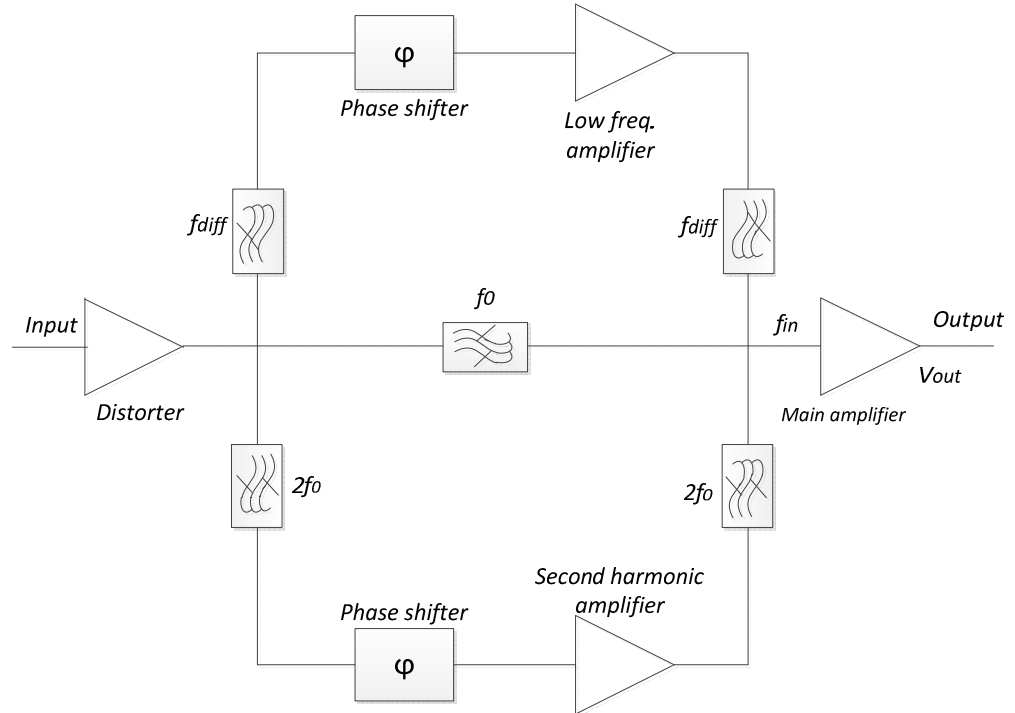


**Figure 4-3:** RF injection technique using second harmonic and frequency difference

The output signal in the nonlinear path I can be expressed by

$$b(t) = A_{11} \cos(2\omega_1 t + 2\phi_1) + A_{22} \cos(2\omega_2 t + 2\phi_2) \quad (4.11)$$

where  $A_{11} = (1/2)A_1^2$ ,  $A_{22} = (1/2)A_2^2$ . The output signal in the nonlinear path II can be expressed as

$$c(t) = A_{33} + A_{33} \cos(2\omega_2 t - 2\omega_1 t + \phi_3) \quad (4.12)$$

where  $A_{33} = (1/2)A_1^2A_2^2$ . The input signal of the main amplifier becomes

$$p(t) = x_1(t) + b(t) + c(t) . \quad (4.13)$$

Finally, if the PA is modelled as power series:

$$y(t) = h_1p(t) + h_2p(t)^2 + h_3p(t)^3 \quad (4.14),$$

and if (4.13) is substituted into (4.14), the obtained third-order IMD products can be written as

$$\begin{aligned} & h_2A_1A_{22} \cos(2\omega_2t - \omega_1t + 2\phi_2) \\ & + \frac{3}{4}h_3A_1A_2^2 \cos(2\omega_2t - \omega_1t) \\ & + \frac{3}{2}A_2A_{22}A_{33}h_3 \cos(2\omega_2t - \omega_1t + \phi_2 - \phi_1) \end{aligned} \quad (4.15)$$

$$\begin{aligned} & h_2A_2A_{11} \cos(2\omega_2t - \omega_1t + 2\phi_1) \\ & + \frac{3}{4}h_3A_2A_1^2 \cos(2\omega_1t - \omega_2t) \\ & + \frac{3}{2}A_1A_{11}A_{33}h_3 \cos(2\omega_1t - \omega_2t + \phi_1 - \phi_2) , \end{aligned} \quad (4.16)$$

while the obtained fifth-order IMD products can be written as

$$\begin{aligned} & \frac{1}{2}h_2A_1A_{33} \cos(2\omega_2t - 3\omega_1t + \phi_3) \\ & + \frac{5}{8}h_5A_1^3A_2^2 \cos(2\omega_2t - 3\omega_1t) \end{aligned} \quad (4.17)$$

$$\begin{aligned} & \frac{1}{2}h_2A_2A_{33} \cos(2\omega_1t - 3\omega_2t + \phi_3) \\ & + \frac{5}{8}h_5A_2^3A_1^2 \cos(2\omega_1t - 3\omega_2t). \end{aligned} \quad (4.18)$$

The third terms in (4.15) and (4.16) are small in comparison to the others and can be omitted. When

$$|\phi_1| = |\phi_2| = 90^\circ \quad (4.19),$$

the 3<sup>rd</sup>-order IMD products are cancelled. The 5<sup>th</sup>-order IMD products cancellation can also be achieved by the condition

$$|\phi_3| = 180^\circ \quad (4.20).$$

#### 4.2.4. Combined Frequency Deference and Third Harmonic Injection

It is assumed again that the main amplifier is related to its input through a power series as follows:

$$V_{out} = aV_{in} + bV_{in}^2 + cV_{in}^3 + dV_{in}^4 + eV_{in}^5 \dots \quad (4.21)$$

The distorter in Figure 4-4 has the purpose of creating signals at both the frequency difference and triple frequency, from the fundamental frequencies [4.9]. The  $f_1$  and  $f_2$  are the fundamental frequencies,  $f_{diff} = f_2 - f_1$  is the frequency difference,  $V_{diff}$  is the amplitude of frequency difference signal and  $V_{triple}$  is the amplitude of the triple frequency signal.

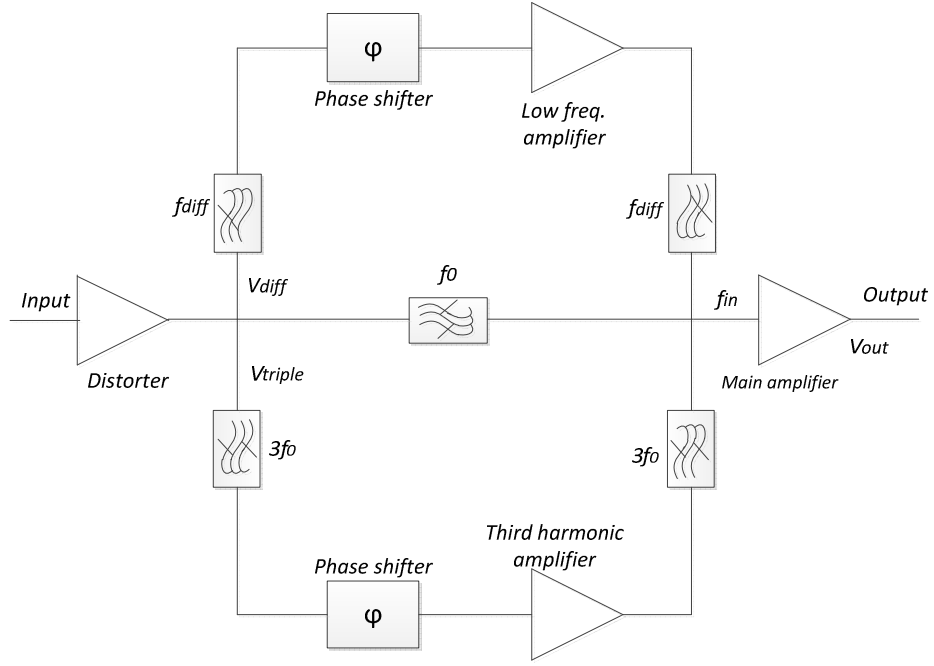


**Figure 4-4:** RF injection technique using third harmonic and frequency difference

The amplitudes of the difference and triple frequency signals at the input of the main amplifier are:

$$V_{main\_diff} = \alpha V_{diff} e^{j\phi_{diff}} \quad (4.22)$$

and

$$V_{main\_triple\_i} = \beta V_{triple\_i} e^{j\phi_{triple}} \quad (4.23)$$

where  $\alpha$  and  $\beta$  are the variable gain of the difference and triple frequency phasors,  $\phi_{diff}$  and  $\phi_{triple}$  are the variable phase shifts of the difference and triple frequency signals, respectively. Symbol  $i = 1,2$  in (4.23) refers to one of the two triple frequency signals. If the fundamental frequency signals are assumed to have amplitudes  $V_{main\_fund\_i}$ , then the signal at the input of the main amplifier can be expressed as

$$\begin{aligned} V_{in} = & V_{main\_fund\_1} \cos(2\pi f_1 t) + V_{main\_fund\_2} \cos(2\pi f_2 t) \\ & + \alpha V_{diff} \cos [(2\pi(f_2 - f_1)t + \phi_{diff}] \\ & + \beta V_{triple\_1} \cos [(2\pi(3f_1)t + \phi_{triple}] \\ & + \beta V_{triple\_2} \cos [(2\pi(3f_2)t + \phi_{triple}] \end{aligned} \quad (4.24)$$

where  $f_2 > f_1$ . When the expression (4.24) is inserted in (4.21), two conclusions can be derived. First, the IM3 component due to the fundamental frequency mixing can be compensated by the second order mixing of the low frequency injected signal with the fundamental frequency signals. By assuming that the fundamental frequency signals have the same amplitude  $V_{main\_fund}$ , the condition for zero IM3 is

$$\alpha = \frac{3c(V_{main\_fund})^2}{2bV_{diff}} \text{ and } \phi_{diff} = 180^\circ \quad (4.25)$$

The second conclusion is that the injection of the difference frequency signal also produces some unwanted signals which fall at the frequency of IM5. The condition for total IM5 cancellation is

$$\beta = \frac{|3c\alpha^2V_{diff}^2 - 12d\alpha^2V_{main\_fund}^2V_{diff} + 10eV_{main\_fund}^4|}{3cV_{main\_fund}V_{triple}} \quad (4.26)$$

and

$$\phi_{triple} = 180^\circ \text{ or } 0 \quad (4.27)$$

where  $\phi_{triple}$  is selected depending on the sign of the nominator in (4.23).

To summarise, if conditions (4.25) and (4.26, 4.27) are met, both IM3 and IM5 can be eliminated theoretically. Condition (4.25) can be met independent of condition expressed in (4.26) and (4.27). In other words, when (4.26) and (4.27) are adjusted by the triple frequency signal, it does not affect IM3 cancellation.

### 4.3. Baseband Components Injection Digital Predistortion

The baseband components injection is a relatively novel DPD methodology initially proposed in [4.12] where the idea of injecting of the third- and fifth-order in-band distortion components in a baseband block is proposed and investigated for a hardware implementation. This technique is described in this Section.

The PA nonlinearity is modelled by a fifth-order polynomial expression as follows:

$$V_{out}(t) = g_1 V_{IN}(t) + g_2 V_{IN}^2 + g_3 V_{IN}^3 + g_4 V_{IN}^4 + g_5 V_{IN}^5, \quad (4.28)$$

where  $V_{IN}(t)$  is the input voltage of the PA and  $g_1, g_2, g_3, g_4, g_5$  are coefficients of the nonlinear polynomial function. A cosine input signal with the amplitude  $V_s(t)$  and phase  $\varphi(t)$  looks like:

$$V_{IN}(t) = V_s(t) \cos(\omega t + \varphi(t)) \quad (4.29)$$

The input signal (4.29) can be re-written into the Cartesian form as follows:

$$V_{IN}(t) = V(I(t) \cos \omega t - Q(t) \sin \omega t) \quad (4.30)$$

where  $V = |\overline{V_s(t)}|$ ,  $I(t) = \frac{V_s(t)}{V} \cos(\varphi(t))$ ,  $Q(t) = \frac{V_s(t)}{V} \sin(\varphi(t))$ , and  $\overline{I(t)^2 + Q(t)^2} = 1$ . After substituting (4.30) into (4.28) and completing trigonometric transformations, the fundamental-frequency part of the output signal can be written:

$$\begin{aligned} V_{OUT}^{FUND}(t) = & g_1 V_{in}(t) + \frac{3V^2 g_3 (I^2(t) + Q^2(t))}{4} V_{IN}(t) \\ & + \frac{5V^4 g_5 (I^2(t) + Q^2(t))^2}{8} V_{IN}(t) \end{aligned} \quad (4.31)$$

In the obtained expression, the first summand is the linear amplified input signal, whereas the second and the third terms are the in-band distortion components produced by the 3<sup>rd</sup>- and 5<sup>th</sup>-order nonlinearity, respectively. The main idea of this approach is to inject those components in the baseband block with the same amplitude and 180° phase shift in order to compensate for the in-band distortion of the PA. For a baseband DPD system injecting the 3<sup>rd</sup>-order distortion component, the input signal can be written as:

$$V_{IN}^{DPD}(t) = V \cdot \{1 + a(I^2(t) + Q^2(t))\} \cdot [I(t) \cos(\omega t) - Q(t) \sin(\omega t)] \quad (4.32)$$

Figure 4-5 shows the schematic of the predistorter based on injecting the 3<sup>rd</sup>-order distortion component [4.12]. The  $I$ ,  $Q$ , and  $I^2+Q^2$  signals are generated in the baseband block and used for creating the predistorted signal according to (4.32). The amplitude and phase of the injected component can be obtained by the amplitude adjustment blocks  $a$  and phase shifters  $\varphi$  correspondingly. The predistorted signal is then up-converted and passed through the PA. After substituting (4.32) into (4.28), the new fundamental-frequency output signal can be written as:

$$\begin{aligned} V_{OUT}^{FUND}(t) &= g_1 V_{IN}(t) + g_1 a [I^2(t) + Q^2(t)] V_{IN}(t) \\ &\quad + \frac{3}{4} \cdot g_3 \cdot V^2 [I^2(t) + Q^2(t)] \cdot V_{IN}(t) \\ &\quad + \frac{9}{4} \cdot g_3 \cdot a \cdot V^2 [I^2(t) + Q^2(t)] \cdot V_{IN}(t) \\ &\quad + \frac{9}{4} \cdot g_3 \cdot a^2 \cdot V^2 [I^2(t) + Q^2(t)] \cdot V_{IN}(t) \end{aligned} \quad (4.33)$$

where  $a$  should be adjusted as

$$a = -\frac{3V^2 g_3}{4g_1} \quad (4.34)$$

in order to compensate for the IM3 distortion.

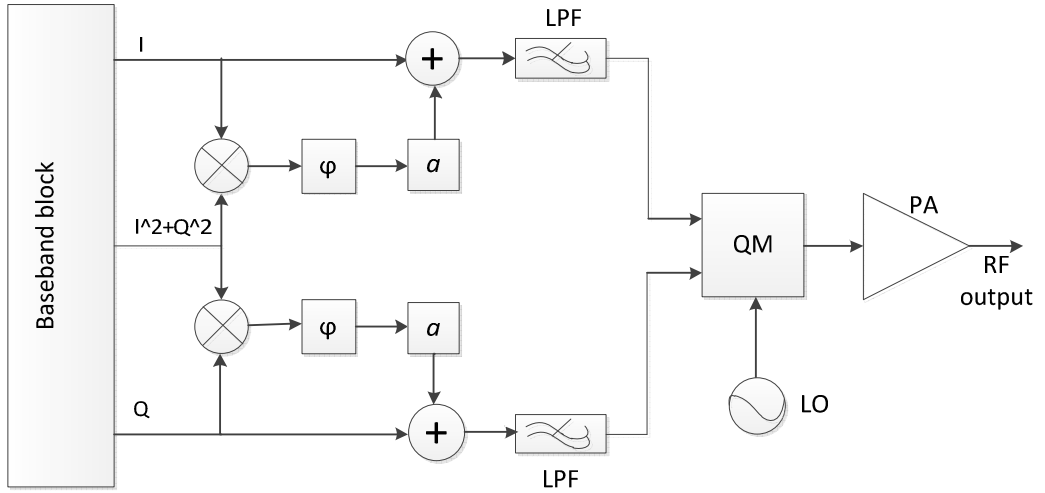


**Figure 4-5:** Block diagram of a third-order baseband component injection

In (4.33), the second and third terms compensate each other, whereas the fourth and fifth terms appear as the new distortion introduced by the injection. These new distortion components are smaller than the original distortion. However, they limit the potential linearisation performance of this technique especially in case of highly nonlinear PA. This phenomenon is known as the distortion compensation limit [4.12], [4.15], [4.16].

The advantages of the described method are small size and low computational complexity as well as simple integration and practical realisation compared to the Volterra-based, ANN-based, LUT-based and polynomial-based DPD. The main disadvantage is limited linearising performance due to the distortion compensation limit and memory effects. Moreover, due to the fact that the technique is implemented in open-loop, an adaptation algorithm should be developed in such a way, that it will not dramatically increase the overall complexity of realisation.

#### 4.4. Iterative Injection Digital Predistortion

This method was developed with the idea to overcome previously described distortion compensation limit of injection [4.15], [4.16]. Non-linearity of a power amplifier (PA) is expressed in a polynomial form:

$$V_{OUT}(t) = \sum_{k=1}^{2p+1} g_k V_{IN}^k(t) \quad (4.35)$$

where  $V_{IN}(t)$  is the input voltage of PA written in Cartesian form (4.30). After substituting (4.30) into (4.35), the distorted output signal at the fundamental frequency can be expressed as:

$$V_{OUT}^{FUND}(t) = g_1 \cdot V_{IN}(t) + \left[ \sum_{k=1}^p b_{2k+1} V^{2k} g_{2k+1} [I^2(t) + Q^2(t)]^k \right] \cdot V_{IN}(t) \quad (4.36)$$

where  $2p + 1$  is the order of the polynomial model (4.35);  $b_{2k+1}$  is an element of the mathematical series described in [4.15]. The first summand in (4.36) is the desired linear signal, whereas the second one is the sum of the in-band distortion components produced by the odd-order polynomial terms. In order to compensate for the nonlinearity, the in-band distortion components are injected into the input signal with the same amplitude, but out of phase:

$$V_{IN}^{(1)}(t) = V_{IN}(t) - \frac{\sum_{k=1}^p G_{2k+1}(t)}{g_1} \cdot V_{IN}(t) \quad (4.37)$$

where  $V_{IN}^{(1)}(t)$  is the input signal predistorted with one injection of the in-band distortion components, and  $G_{2k+1}(t)$  is defined as:

$$G_{2k+1}(t) = b_{2k+1} V^{2k} g_{2k+1} [I^2(t) + Q^2(t)]^k \quad (4.38)$$

After substituting (4.37) into the general  $2p + 1$ -order nonlinear model (4.35), the output signal can be written as:

$$\begin{aligned} V_{OUT}^{(1)} = & g_1 \cdot V_{IN}(t) - \sum_{k=1}^p G_{2k+1}(t) \cdot V_{IN}(t) + g_2 \cdot \left( 1 - \frac{\sum_{k=1}^p G_{2k+1}(t)}{g_1} \right)^2 V_{IN}^2(t) + g_3 \\ & \cdot \left( 1 - \frac{\sum_{k=1}^p G_{2k+1}(t)}{g_1} \right)^3 \cdot V_{IN}^3(t) + g_4 \cdot \left( 1 - \frac{\sum_{k=1}^p G_{2k+1}(t)}{g_1} \right)^4 \cdot V_{IN}^4(t) \\ & + g_5 \cdot \left( 1 - \frac{\sum_{k=1}^p G_{2k+1}(t)}{g_1} \right)^5 \cdot V_{IN}^5(t) + \dots \end{aligned} \quad (4.39)$$

where  $V_{OUT}^{(1)}$  is the total output signal after predistortion of the input signal with one injection of the in-band distortion components. The even-order terms of the polynomial model do not produce in-band distortions. In contrast, the odd-order terms generate in-band distortions components at the fundamental frequency, which are described analytically as the following mathematical operator:

$$g_{2k+1}V_{IN}^{2k+1}(t) \rightarrow G_{2k+1}(t)V_{IN}(t) \quad (4.40)$$

This notation indicates that the in-band distortion component  $G_{2k+1}(t)V_{IN}(t)$  is produced by the odd-order polynomial term  $g_{2k+1}V_{IN}^{2k+1}(t)$ . In other words,  $G_{2k+1}(t)V_{IN}(t)$  has a one-to-one correspondence with the term  $g_{2k+1}V_{IN}^{2k+1}(t)$ . Therefore, each odd-order term of (4.35) produces the corresponding distortion component at the fundamental frequency:

$$(g_{2k+1}V_{IN}^{2k+1}(t))^{FUND} = G_{2k+1}(t)V_{IN}(t) \quad (4.41)$$

Using (4.37), the output signal at the fundamental frequency after predistortion of the input signal with one injection of the in-band distortion components can be expressed:

$$\begin{aligned} V_{OUT}^{(1)FUND} &= g_1 \cdot V_{IN}(t) - \sum_{k=1}^p G_{2k+1}(t) \cdot V_{IN}(t) \\ &+ G_3(t) \cdot \left(1 - \frac{\sum_{k=1}^p G_{2k+1}(t)}{g_1}\right)^3 V_{IN}(t) \\ &+ G_5(t) \cdot \left(1 - \frac{\sum_{k=1}^p G_{2k+1}(t)}{g_1}\right)^5 V_{IN}(t) \end{aligned} \quad (4.42)$$

As can be seen from (4.42), after completing one injection, the original distortion components are compensated for. Indeed, the obtained expression can be re-written as:

$$\begin{aligned} V_{OUT}^{(1)FUND} &= g_1 \cdot V_{IN}(t) + G_3(t) \cdot \left[-1 + \left(1 - \frac{\sum_{k=1}^p G_{2k+1}(t)}{g_1}\right)^3\right] V_{IN}(t) \\ &+ G_5(t) \cdot \left[-1 + \left(1 - \frac{\sum_{k=1}^p G_{2k+1}(t)}{g_1}\right)^5\right] V_{IN}(t) \dots \end{aligned} \quad (4.43)$$

After expanding the brackets in (4.43), it can be easily shown that the initial distortion components are compensated for. However, the new distortion components caused by the initially injected signal appear. Therefore, it is necessary to recalculate the new in-band distortion components and to compensate for them during the next iteration. The new predistorted input signal at the second iteration looks like:

$$V_{IN}^{(2)}(t) = V_{IN}(t) - \frac{\sum_{k=1}^p G_{2k+1}^{(1)}(t)}{g_1} \cdot V_{IN}(t) \quad (4.44)$$

where  $G_{2k+1}^{(1)}(t)$  is the magnitude factor of the  $(2k + 1)$ -order in-band distortion component after the first iteration. It is obtained from (4.43) as follows:

$$G_{2k+1}^{(1)}(t) = G_{2k+1}(t) \cdot \left[ -1 + \left( 1 - \frac{\sum_{i=1}^p G_{2i+1}(t)}{g_1} \right)^{2k+1} \right] \quad (4.45)$$

When the procedure is repeated once again, the new in-band distortion components are calculated and the expressions for the injected signals in next iteration are obtained. Deductively, on the  $m$ -th iteration, the predistorted input and the corresponding output signals can be written as:

$$V_{IN}^{(m)}(t) = V_{IN}(t) - \frac{\sum_{k=1}^p G_{2k+1}^{(m-1)}(t)}{g_1} \cdot V_{IN}(t), \quad (4.46)$$

$$V_{OUT}^{(m)FUND} = g_1 \cdot V_{IN}(t) + \left( \sum_{k=1}^p G_{2k+1}^{(m)} \right) \cdot V_{IN}(t), \quad (4.47)$$

$$G_{2k+1}^{(m)}(t) = G_{2k+1}^{(m-1)}(t) \cdot \left[ -1 + \left( 1 - \frac{\sum_{i=1}^p G_{2i+1}^{(m-1)}(t)}{g_1} \right)^{2k+1} \right] \quad (4.48)$$

where  $n = 2p + 1$  – is the order of the polynomial model and  $G_{2k+1}^{(m)}(t)$  is the magnitude factor of an odd in-band distortion component at the  $m$ -th iteration. Equations (4.46)-(4.48) represent the general mathematical model for the proposed baseband iterative injection DPD technique for  $n$ -order polynomial model and  $m$  iterations [4.15], [4.16].

The described baseband digital predistorter incorporates iterative injection of the in-band distortion components, which are generated using the following parameters: number of iterations  $m$ , polynomial coefficients  $g_{2k+1}$ , of the  $n$ -order nonlinear model, and derived coefficients  $b_{2k+1}$ . The latter is fixed, whereas the parameters  $m$  and  $g_{2k+1}$  depend on the particular PA and can be adjusted. The proposed DPD requires iterative updates of the magnitude factors of the injected signals for each injection, which can be accomplished in a DSP block.

Figure 4-6 illustrates the operation of the proposed digital baseband predistorter with iterative injection algorithm [4.15], [4.16]. The signal source generates input data, which are mapped to the required modulation type and divided into the  $I$  and  $Q$  components. These  $I$  and  $Q$  signals are used to calculate the mean value  $V$  of the input signal magnitude. The  $I$  and  $Q$  are then multiplied by  $1/V$  for normalisation. This procedure is done in order to achieve  $V = |\overline{V_s(t)}|$  and not to affect the mean power level by predistortion. The proposed baseband predistortion described in (4.46)-(4.48) are applied to the normalised signal components  $I^{norm}$  and  $Q^{norm}$ . After this step, the signals are multiplied by  $V$  for de-normalisation, filtered with low-pass raised-cosine filters, and transferred to the I/Q modulator. Finally, the obtained RF signal is passed through the PA to the output of the transmitter.

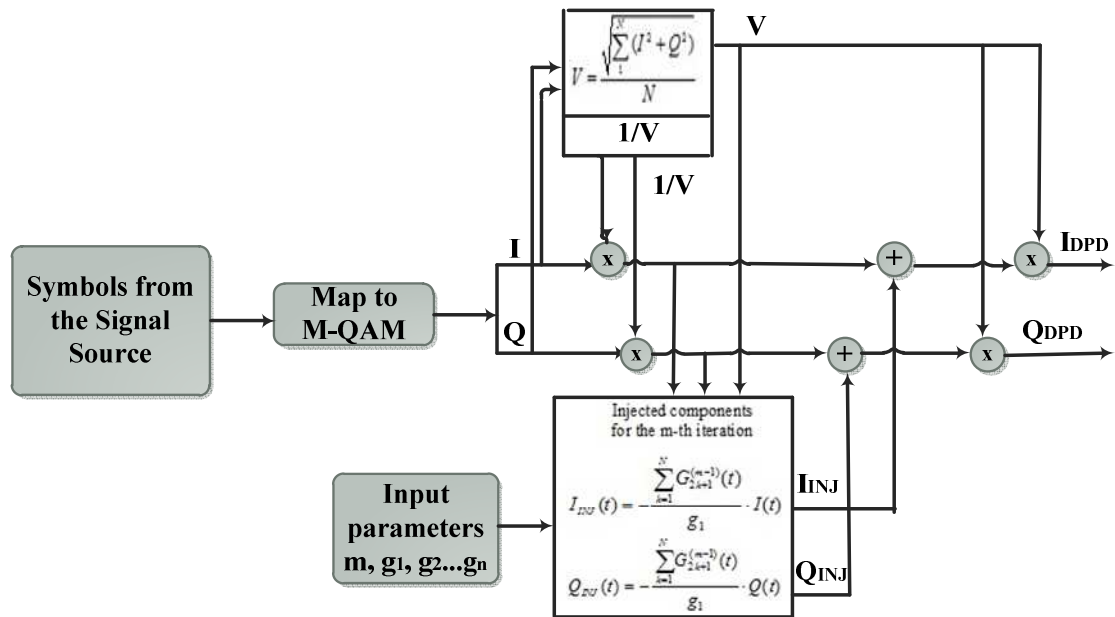


**Figure 4-6:** Block diagram of the digital predistorter using iterative injection of the in-band distortion components

## 4.5. Conclusion

The injection-based linearisation approaches were described in this Chapter. Firstly, the initially proposed solutions implemented in RF were depicted. Secondly, a description of the injection-based techniques implemented as DPD was given. In general, linearisation methods based on injection approach have smaller complexity compared with the other proposed techniques for nonlinearity compensation purposes. Due to this fact, these techniques are used as a basis for developing of advanced DPD linearisation methods and this separated Chapter is dedicated to them. However, there are number of problems that seriously deteriorate the practical implementation of these techniques in modern wireless transmitters. The existing injection-based techniques were tested in open loop and due to that fact, are not adaptive and have limited usage in real transmitters. In addition to this, there was no experimental evidence how these techniques behave with 4G signals having very variable amplitudes. Also, there are no injection-based solutions for multi-frequency and multi-branch MIMO transmitters. As will be shown later, the application of the previous solutions in these transmitters is impractical for several reasons. The advanced solutions that overcome these problems will be presented in the following Chapters.

## 4.6. References

- [4.1] S. M. Li, D. Jing, and W. S. Chan, "Verification of practicality of using the second harmonic for reducing IMD," *Electron. Lett.*, vol.34, no.11, pp.1097-1098, May 1998.
- [4.2] C.S. Aitchison, M. Mbabele, M.R. Moazzam, D. Budimir, and F. Ali, "Improvement of third-order intermodulation product of RF and microwave amplifiers by injection," *IEEE Trans. Microw. Theory Tech.*, vol.49, no.6, pp.1148-1154, June 2001.
- [4.3] A. Dani, M. Roberg, and Z. Popovic, "PA efficiency and linearity enhancement using external harmonic injection," *IEEE Trans. Microw. Theory Tech.*, vol.60, no.12, pp. 4097-4106, Dec. 2012.
- [4.4] M. Modeste, D. Budimir, M.R. Moazzam, and C.S. Aitchison, "Analysis and practical performance of a difference frequency technique for improving the multicarrier IMD performance of RF amplifiers," in *IEEE MTT-S Symp. Techn. for Wireless Applic.*, pp.53-56, Feb. 1999.
- [4.5] Y.P. Kwon; Y.C. Jeong; Y. Kim, and C.D. Kim, "A design of predistortion linearizer using 2<sup>nd</sup> order low frequency intermodulation signal injection," in *Proc. 33rd Eur. Microw. Conf*, pp. 249-252, Oct. 2003.
- [4.6] Y. Yang, Y. Y. Woo., and B. Kim, "New predistortion linearizer using low-frequency even-order intermodulation components," *IEEE Trans. Microw. Theory Tech.*, vol.50, no.2, pp.446-452, Feb 2002.
- [4.7] K.J. Cho, D.H. Jang, S.H. Kim, J.H. Kim, B. Lee, N.Y. Kim, J.C. Lee, and S.P. Stapleton, "Multi-order predistortion of power amplifiers using a second harmonic based technique," *IEEE Microw. Wireless Comp. Lett.*, vol.13, no.10, pp.452-454, Oct. 2003.

- [4.8] K.J. Cho, D.H. Jang, S.H. Kim, J.Y. Kim, J.H. Kim, and S.P. Stapleton, "An analog compensation method for asymmetric IMD characteristics of power amplifier," *IEEE Microw. Wireless Comp. Lett.*, vol.14, no.4, pp. 153-155, April 2004.
- [4.9] S. Bulja, and D. Mirshekar-Syahkal, "Combined low frequency and third harmonic injection in power amplifier linearization," *IEEE Microw. Wireless Comp. Lett.*, vol.19, no.9, pp.584-586, Sept. 2009.
- [4.10] F. Chun-Wah, and K.-K.M. Cheng, "Theoretical and experimental study of amplifier linearization based on harmonic and baseband signal injection technique," *IEEE Trans. Microw. Theory Tech.*, vol.50, no.7, pp.1801-1806, July 2002.
- [4.11] M. Xiao, and P. Gardner, "Characterisation, analysis and injection of two-tone third-order intermodulation products in an amplifier," *IET Microw., Antennas. & Propag.*, vol.3, no.3, pp.443-455, April 2009.
- [4.12] N. Mizusawa, and S. Kusunoki, "Third- and fifth-order baseband component injection for linearization of the power amplifier in a cellular phone," *IEEE Trans. Microw. Theory Tech.*, vol. 53, no. 4, pp. 3327-3334, April 2005.
- [4.13] M. Xiao, and P. Gardner, "Digital baseband injection techniques to reduce spectral regrowth in power amplifier," in *IEEE MTT-S Int. Microw. Symp. Dig.*, pp.1513-1516, 2008.
- [4.14] M. Thian, M. Xiao, and P. Gardner, "Digital baseband predistortion based linearized broadband inverse Class-E power amplifier," *IEEE Trans. Microw. Theory Tech.*, vol.57, no.2, pp.323-328, Feb. 2009.
- [4.15] D. Bondar, and D. Budimir, "A digital predistorter for wireless transmitters", *Int. J. of RF and Microw. Comput.-Aided Eng.*, vol. 19, no 4, pp. 453-459, April 2009.
- [4.16] D. Bondar, "Advanced Digital Predistortion of Power Amplifiers for Mobile and Wireless Communications", PhD Thesis, University of Westminster, London, UK, 2009.

## 5. Adaptive DPD for 4G Wireless Transmitters

### 5.1. Introduction

A new adaptive DPD technique for 4G SISO wireless transmitters is described in this Chapter [5.1]. The technique is based on adaptive iterative injections of the in-band distortion components. In comparison with the previously proposed DPDs, this method has two important advantages. First, it uses real multiplications and real additions only and avoids complex Volterra, LUT or polynomials [5.2]-[5.4] for nonlinearity compensation. Secondly, in contrast with existing injection-based DPD [5.5]-[5.7], the technique uses adaptive architecture [5.3], and therefore, is adaptive to the variation of PA nonlinear transfer function in real environmental conditions. The proposed DPD is verified experimentally using more than 10 dB peak-to-average power ratio (PAPR) 5-MHz downlink Long Term Evolution (LTE) signal. This is the first injection-based technique experimentally verified utilising high PAPR signal such as LTE.

### 5.2. Proposed Approach

The nonlinear behaviour of a PA is modelled by a polynomial expression [5.7]:

$$V_{OUT}(t) = \sum_{k=1}^M g_k V_{IN}^k(t) \quad (5.1)$$

where  $V_{IN}(t)$  is the input voltage,  $g_1, g_2, g_3, \dots$  are polynomial coefficients, and  $M$  is the order of the polynomial model. For a digitally modulated signal with variable amplitude  $V_S(t)$  and phase  $\varphi(t)$ , the input signal can be written using the in-phase  $I(t)$  and quadrature  $Q(t)$  components:

$$V_{IN}(t) = V_S(t) \cos(\omega t + \varphi(t)) = V(I(t) \cos \omega t - Q(t) \sin \omega t) \quad (5.2)$$

where the average value of the amplitude is  $V = \sqrt{\overline{V_S(t)^2}}$ , and  $\overline{I(t)^2 + Q(t)^2} = 1$ .

The total output signal is obtained after substituting (5.2) into (5.1). It can be written as a sum of  $\cos(i \cdot \omega t)$  terms, where  $i = 0, 1, 2, \dots$ . The term containing  $\cos(\omega t)$  is the fundamental-frequency part of the output signal, derived as follows:

$$V_{OUT}^{FUND}(t) = \left( g_1 + \sum_{k=1}^p b_{2k+1} V^{2k} g_{2k+1} (I^2(t) + Q^2(t))^k \right) V_{IN}(t) \quad (5.3)$$

where  $b_{2k+1}$  are the mathematical series of the in-band distortion coefficients presented in [5.7] and  $2p+1$  is polynomial order of PA. Apart from the desired linear part  $g_1 V_{IN}(t)$ , the output signal (5.3) contains in-band distortion components from all the odd-order terms of the polynomial model. To compensate for these distortions, an injection of the odd-order distortion components with opposite phases is used here. The injected components generate new distortion products while compensating for the initial distortion. That new distortion is suppressed by the following steps:

1. injecting the opposite odd-order distortion components into the initial input signal at baseband;
2. re-calculating the new in-band distortions;
3. repeating injection until the specified linearisation degree is achieved.

The steps mentioned previously can be applied to any order of PA nonlinearity and injections' number depends on required performances. The mathematical model of the proposed iterative predistortion technique for  $(2p+1)$ -order nonlinearity and  $m$  iterations is given by the following equations:

$$V_{IN}^{(m)}(t) = V_{IN}(t) \left( 1 - \frac{1}{g_1} \sum_{k=1}^p G_{2k+1}^{(m-1)}(t) \right) \quad (5.4)$$

$$G_{2k+1}^{(m-1)}(t) = G_{2k+1}^{(m-2)}(t) \left[ -1 + \left( 1 - \frac{1}{g_1} \sum_{i=1}^p G_{2i+1}^{(m-2)}(t) \right)^{2k+1} \right] \quad (5.5)$$

where

$$G_{2k+1}(t) = b_{2k+1} \cdot g_{2k+1} |V_s(t)|^{2k} \quad (5.6)$$

represents the magnitude factor of a  $(2k+1)$ -order in-band distortion component and  $G_{2k+1}^{(m)}(t)$  is the value of  $G_{2k+1}(t)$  on the  $m$ -th iteration. The proposed predistorter shown in Figure 5-1 consists of two parts: feedback (FB) and feedforward (FF). The coefficients of PA transfer function are extracted in FB block using least square regression (LSR) methodology [5.8]-[5.10]. An initial DPD signal and down-converted PA output signal are used as LSR input and LSR target, respectively.

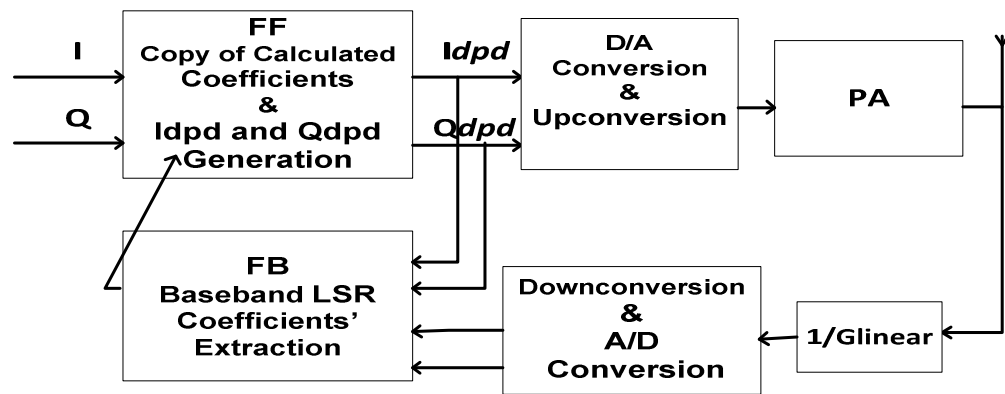


**Figure 5-1:** Functional block diagram of the proposed predistorter

After that, the obtained coefficients are copied to FF block and used for generation of predistorted  $Idpd$  and  $Qdpd$  signal components which are baseband equivalent of (5.4)-(5.6). Therefore, the proposed predistorter is based on adaptive architecture [5.3] and as such is adaptable to instantaneous variations of PA transfer function. It should be noted that the direct learning based adaptive architecture [5.3] is used here only for the extraction of the PA's polynomial coefficients. In other words, the calculation of the digitally predistorted signal is independent of the adaptive direct learning architecture. Therefore, it can be concluded that the used adaptive DPD is based on simplified direct learning architecture. As can be observed from (5.4)-(5.6), the mathematical operations are restricted to real multiplications and additions only which is significant DPD complexity reduction in comparison with using complex Volterra, LUT, or polynomials for nonlinearity compensation purposes.

### 5.3. Least Square Regression (LSR)

The LSR approximation can be described as follows. Let us suppose that a set of experimental data is obtained as  $n$  pairs of an input  $x_i$  and the corresponding output  $y_i$  variables:  $(x_1, y_1), (x_2, y_2), (x_3, y_3), \dots, (x_n, y_n)$ , where  $n$  is number of samples.

Then, the sum of squared residuals between the measured and modelled down-converted data samples can be written as:

$$S = \sum_{i=1}^n [y_i - \tilde{y}_i]^2 \quad (5.7)$$

where  $\{y_i\}$  and  $\{\tilde{y}_i\}$  are the measured and modelled output data respectively. In relation (5.7), the approximating function is given in the form of:

$$y_i = \sum_{k=0}^M a_{2k+1} x_i^{2k+1} \quad (5.8)$$

An example of the measured set of data  $\{x_i, y_i\}$  for a ZFL-500 PA is illustrated in Figure 5-2.

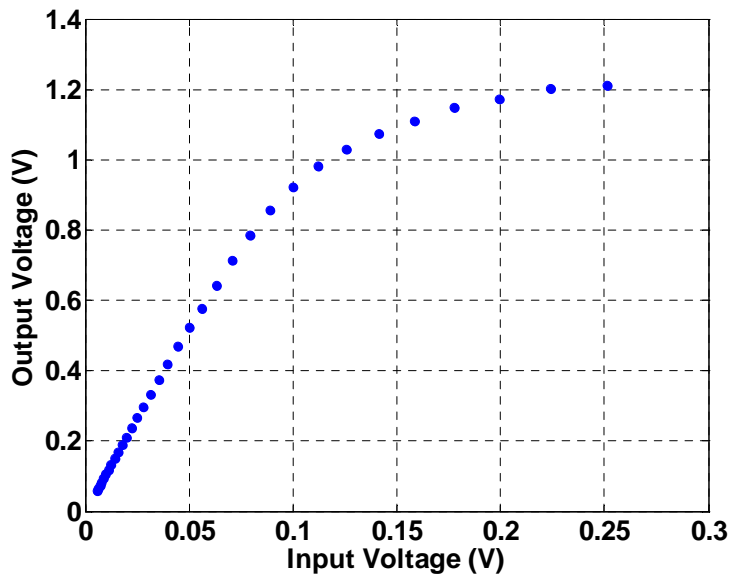


**Figure 5-2:** AM/AM characteristic used to extract the memoryless model for ZFL-500 PA

Then, (5.8) can be re-written as:

$$S = \sum_{i=1}^n [y_i - (a_1 x_i + a_3 x_i^3 + a_5 x_i^5 + \dots + a_M x_i^M)]^2 \quad (5.9)$$

or

$$\begin{aligned} S = & [y_1 - (a_1 x_1 + a_3 x_1^3 + a_5 x_1^5 + \dots + a_M x_1^M)]^2 \\ & + [y_2 - (a_1 x_2 + a_3 x_2^3 + a_5 x_2^5 + \dots + a_M x_2^M)]^2 \\ & + [y_3 - (a_1 x_3 + a_3 x_3^3 + a_5 x_3^5 + \dots + a_M x_3^M)]^2 + \dots \\ & + [y_n - (a_1 x_n + a_3 x_n^3 + a_5 x_n^5 + \dots + a_M x_n^M)]^2 \end{aligned} \quad (5.10)$$

The partial derivatives of  $S$  with respect to  $a_{2k+1}$  look like:

$$\begin{aligned} \frac{dS}{da_1} = & 2x_1 [y_1 - (a_1 x_1 + a_3 x_1^3 + a_5 x_1^5 + \dots + a_M x_1^M)] \\ & + 2x_2 [y_2 - (a_1 x_2 + a_3 x_2^3 + a_5 x_2^5 + \dots + a_M x_2^M)] \dots \\ & + 2x_n [y_n - (a_1 x_n + a_3 x_n^3 + a_5 x_n^5 + \dots + a_m x_n^m)] \end{aligned} \quad (5.11)$$

$$\begin{aligned} \frac{dS}{da_3} = & 2x_1^3 [y_1 - (a_1 x_1 + a_3 x_1^3 + a_5 x_1^5 + \dots + a_M x_1^M)] \\ & + 2x_2^3 [y_2 - (a_1 x_2 + a_3 x_2^3 + a_5 x_2^5 + \dots + a_M x_2^M)] \dots \\ & + 2x_n^3 [y_n - (a_1 x_n + a_3 x_n^3 + a_5 x_n^5 + \dots + a_M x_n^M)] \end{aligned} \quad (5.12)$$

.....

$$\begin{aligned} \frac{dS}{da_M} = & 2x_1^M [y_1 - (a_1 x_1 + a_3 x_1^3 + a_5 x_1^5 + \dots + a_M x_1^M)] \\ & + 2x_2^M [y_2 - (a_1 x_2 + a_3 x_2^3 + a_5 x_2^5 + \dots + a_M x_2^M)] \dots \\ & + 2x_n^M [y_n - (a_1 x_n + a_3 x_n^3 + a_5 x_n^5 + \dots + a_M x_n^M)] \end{aligned} \quad (5.13)$$



$$s_j = \sum_{i=1}^n x_i \quad (5.20)$$

$$t_j = \sum_{i=1}^n y_i x_i \quad (5.21)$$

In the system (5.17)-(5.19), the number of equations corresponds to the degree of the model. After solving this system, the values  $a_{2k+1}$  are obtained. Then,  $g_{2k+1}$  are calculated as:

$$g_{2k+1} = \frac{a_{2k+1}}{b_{2k+1}} \quad (5.22)$$

The method of extracting  $g$ -coefficients described above offers an excellent accuracy of approximation, which will be verified experimentally.

## 5.4. Experimental Results

Experimental setup used in this work is shown in Figure 5-3. At first, 5-MHz downlink LTE signal with 300 data subcarriers and FFT size 512 was created in Matlab. Created signal was download to the Agilent MXG N5182A signal generator via General Purpose Interface Bus (GPIB) where it was up-converted to RF (downloading process was performed by Agilent Signal Studio Toolkit assistance). MXG RF output signal is passed through Device Under Test (DUT) Mini-Circuits ZFL-500 PA (21 dB gain, output P1dB +10 dBm, IP3 +19 dBm) which was driven in hard compression region. Finally, signal is down-converted by Agilent Vector Signal Analyser and captured on PC by Agilent Distortion Suite software. Following that, the captured signal was used for further processing and analysis. MXG Event 1 out and 10 MHz reference were used for VSA analyser synchronisation with MXG signal source. The described DPD

approach has been implemented in Matlab. After each iteration, the predistorted I and Q signal components were downloaded to MXG signal generator again and whole experimental process was repeated until transmitter reached the specified performance.

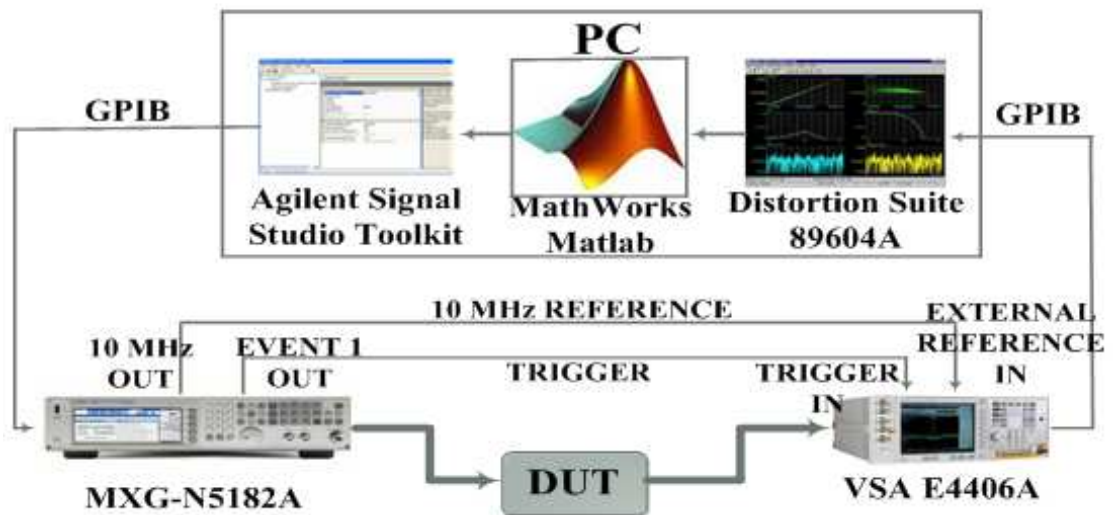


**Figure 5-3:** Experimental setup

The spectrums of linear PA output signal, PA output signal without DPD and PA output signal obtained after using three iterations of  $7^{th}$ -order polynomial adaptive baseband iterative injections DPD are shown in Figure 5-4. As can be seen, the spectrum regrowth suppression of about 10 dB was achieved. The PA output spectrum in case of using proposed DPD technique is almost the same as linear PA output spectrum whereas the measurement system noise level is achieved. Also, the measured Error Vector Magnitude (EVM) is significantly reduced from 7.4% to 0.8%.

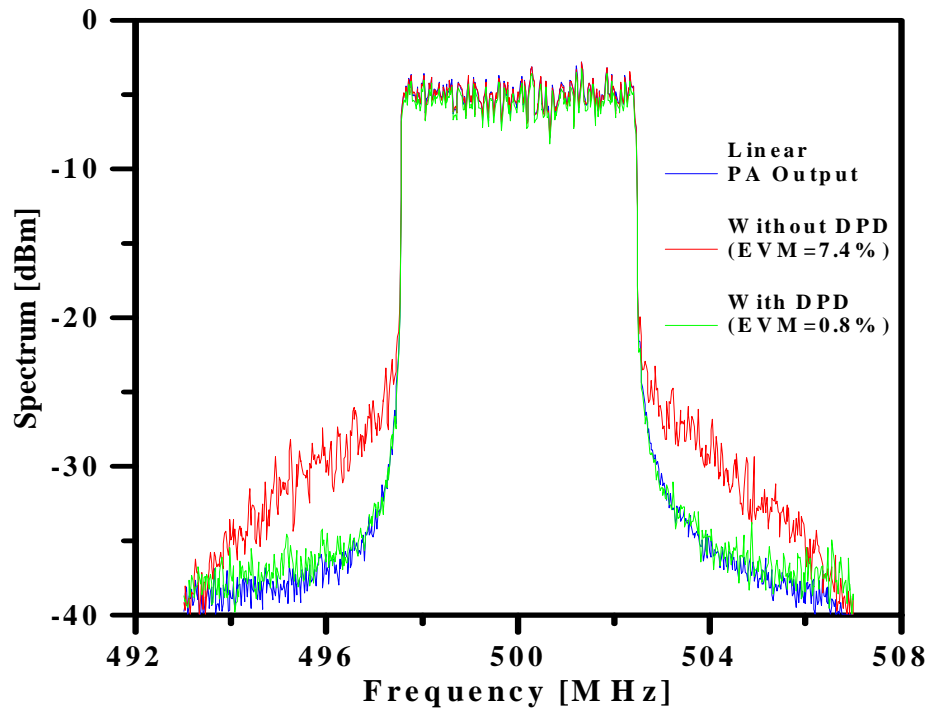


Figure 5-4: Spectrum regrowth improvement of PA downlink LTE signal

## 5.5. Conclusion

The proposed nonlinearity compensation technique based on iterative injection approach has been successfully attested by means of experiments. This is the first time that injection-based DPD technique is experimentally corroborated with very high peak-to-average ratio 4G LTE signal. Furthermore, compared to previously introduced open-loop injection methods, this technique uses adaptive closed-loop DPD architecture. The proposed DPD approach has low memory requirements and computational complexity. Therefore, it should be considered as a serious candidate to become a predistorter part for nonlinearity compensation in modern wireless transmitter applications.

## 5.6. References

- [5.1] M. Cabarkapa, N. Neskovic, A. Neskovic, and D. Budimir, "Adaptive nonlinearity compensation technique for 4G wireless transmitters," *Electron. Lett.*, vol.48, no.20, pp.1308-1309, Sept. 2012.

- [5.2] D. Ronnow, and M. Isaksson, 'Digital predistortion of radio frequency power amplifiers using Kautz-Volterra model', *Electron. Lett.*, vol. 42, no. 13, pp. 780–782., July 2006.
- [5.3] F. Li, B. Feuvrie, Y. Wang, and W. Chen, "MP/LUT baseband digital predistorter for wideband linearisation," *Electron. Lett.*, vol. 47, no. 19, pp.1096-1098, Oct. 2011.
- [5.4] J. Kim, and K. Konstantinou, 'Digital predistortion of wideband signals based on power amplifier model with memory', *Electron. Lett.*, vol. 37, no. 23, pp. 1417– 1418, Dec. 2001.
- [5.5] N. Mizusawa, and S. Kusunoki, "Third- and fifth-order baseband component injection for linearization of the power amplifier in a cellular phone," *IEEE Trans. Microw. Theory Tech.*, vol. 53, no. 4, pp. 3327-3334, April 2005.
- [5.6] M. Thian, M. Xiao, and P. Gardner, "Digital baseband predistortion based linearized broadband inverse Class-E power amplifier," *IEEE Trans. Microw. Theory Tech.*, vol.57, no.2, pp.323-328, Feb. 2009.
- [5.7] D. Bondar, and D. Budimir, "A digital predistorter for wireless transmitters", *Int. J. of RF and Microw. Comput.-Aided Eng.*, vol. 19, no 4, pp. 453-459, April 2009.
- [5.8] S. Haykin, "Adaptive Filter Theory," 4th ed. Upper Saddle River, NJ: Prentice-Hall, 2002.
- [5.9] D. Bondar, „Advanced Digital Predistortion of Power Amplifiers for Mobile and Wireless Communications”, PhD Thesis, University of Westminster, London, UK, 2009.
- [5.10] S. Haykin, "Neural Networks: A Comprehensive Foundation" Upper Saddle River, NJ: Prentice-Hall, 1999.

## 6. 2-D DPD for Concurrent Dual-band Transmitters

### 6.1. Introduction

In this Chapter, a new memoryless two-dimensional (2-D) DPD technique for concurrent dual-band wireless transmitters is explained [6.1]. As will be shown, the existing injection-based techniques [6.2]-[6.8] cannot be used in concurrent dual-band wireless transmitters. For that reason, the injection-based DPD theory is expanded to be applicable in concurrent dual-band transmitters. The proposed DPD approach is based on simultaneous injection of the in-band IM and CM products, and intentionally avoiding using complex polynomials, LUTs, Volterra, or ANN approaches for nonlinearity compensation purposes [6.9]-[6.14]. The advantage of the proposed approach lies in its simplicity in comparison with state-of-the-art approaches. Furthermore, the performances of the proposed DPD architecture do not depend on frequency separation between bands in concurrent dual-band transmitter. The proposed DPD is experimentally verified using ZFL-500 PA as DUT. The real WCDMA signal at 400 MHz and 3-MHz LTE signal at 500 MHz are used as testing signals in experimentally emulated concurrent dual-band transmitter. The technique presented in this Chapter presents an excellent basis for developed complete, general DPD approach described in Chapter 7.

### 6.2. Proposed 2-D DPD

The nonlinear behaviour of a PA is modelled by a polynomial expression in both frequency bands of concurrent dual-band transmitter:

$$V_{OUT}^{(1)}(t) = \sum_{k=1}^N g_k^{(1)} V_{IN}^k(t) \quad (6.1)$$

$$V_{OUT}^{(2)}(t) = \sum_{k=1}^M g_k^{(2)} V_{IN}^k(t) \quad (6.2)$$

where  $V_{IN}(t)$  is the PA input signal,  $g_k^{(1)}$  and  $g_k^{(2)}$  are the coefficients of the polynomial models with  $N$  and  $M$  order in each band, respectively. The PA input signal can be represented as a sum of digitally modulated signals in each band:

$$V_{IN}(t) = V_{IN}^{(1)}(t) + V_{IN}^{(2)}(t) = V_{S1}(t) \cos(\omega_1 t + \varphi_1(t)) + V_{S2}(t) \cos(\omega_2 t + \varphi_2(t)) \quad (6.3)$$

For these digitally modulated signals with variable amplitudes  $V_{S1}(t)$  and  $V_{S2}(t)$  and variable phases  $\varphi_1(t)$  and  $\varphi_2(t)$ , the input signal can be written using the in-phase  $I_1(t)$  and  $I_2(t)$  and quadrature  $Q_1(t)$  and  $Q_2(t)$  components:

$$V_{IN}(t) = V_1(I_1(t) \cos \omega_1 t - Q_1(t) \sin \omega_1 t) + V_2(I_2(t) \cos \omega_2 t - Q_2(t) \sin \omega_2 t) \quad (6.4)$$

where the average value of the amplitudes are  $V_1 = \sqrt{\overline{V_{S1}(t)^2}}$ ,  $V_2 = \sqrt{\overline{V_{S2}(t)^2}}$ , and  $\overline{I_1(t)^2 + Q_1(t)^2} = 1$ ,  $\overline{I_2(t)^2 + Q_2(t)^2} = 1$ .

The total output signal is obtained after substituting (6.4) into (6.1) and (6.2) with  $N = M = 5$ . It can be written as a sum of  $\cos(i\omega_1 \pm j\omega_2)t$  terms, where  $i, j = 0, 1, 2, \dots$ . The terms containing  $\cos(\omega_1 t)$  and  $\cos(\omega_2 t)$  are the unwanted fundamental-frequency parts of the output signal related to each band. The other terms are considered to be far enough from the concurrent operating bands, and therefore can be easily filtered out. The fundamental-frequency parts of the output signal related to each band are:

$$V_{OUT}^{FUND(1)}(t) = V_{IN}^{(1)}(t) [g_1^{(1)} + \frac{3}{4}g_3^{(1)}V_1^2(I_1^2 + Q_1^2) + \frac{5}{8}g_5^{(1)}V_1^4(I_1^2 + Q_1^2)^2 + \frac{3}{2}g_3^{(1)}V_2^2(I_2^2 + Q_2^2) + \frac{15}{8}g_5^{(1)}V_2^4(I_2^2 + Q_2^2)^2 + \frac{15}{4}g_5^{(1)}V_1^2V_2^2(I_1^2 + Q_1^2)(I_2^2 + Q_2^2)] \quad (6.5)$$

and

$$\begin{aligned}
 V_{OUT}^{FUND(2)}(t) = & V_{IN}^{(2)}(t)[g_1^{(2)} + \frac{3}{4}g_3^{(2)}V_2^2(I_2^2 + Q_2^2) + \\
 & \frac{5}{8}g_5^{(2)}V_2^4(I_2^2 + Q_2^2)^2 + \frac{3}{2}g_3^{(1)}V_1^2(I_1^2 + Q_1^2) + \\
 & \frac{15}{8}g_5^{(2)}V_1^4(I_1^2 + Q_1^2)^2 + \frac{15}{4}g_5^{(2)}V_1^2V_2^2(I_1^2 + Q_1^2)(I_2^2 + Q_2^2)] \quad (6.6).
 \end{aligned}$$

Apart from the desired linear parts  $g_1^{(1)}V_{IN}^{(1)}(t)$  and  $g_1^{(2)}V_{IN}^{(2)}(t)$ , the fundamental-frequency output signals (6.5) and (6.6) contain distortion components from all the odd-order terms of the polynomial models. In addition to IM distortion specific for the conventional transmitters, the (6.5) and (6.6) contain CM products caused by interaction between frequency bands in concurrent dual-band transmitters. To explain, the second and third terms in (6.5) and (6.6) are related to third- and fifth-order in-band IM products (IM3 and IM5), the fourth term is related to third-order CM product (CM3) and fifth and sixth terms are related to fifth-order CM products (CM5). In order to compensate for these distortions, a simultaneous injection of the in-band IM3 and IM5 together with CM3 and two CM5 products, all with opposite phases, is proposed for both frequency bands in concurrent dual-band transmitter. The total predistorter output signal with injected in-band IM and CM distortion components consists of the two terms related to each frequency band:

$$V_{DPD}(t) = V_{DPD}^{(1)}(t) + V_{DPD}^{(2)}(t) \quad (6.7)$$

where

$$\begin{aligned}
 V_{DPD}^{(1)}(t) = & V_{IN}^{(1)}(t)[1 + a_1(I_1^2 + Q_1^2) + b_1(I_1^2 + Q_1^2)^2 + \\
 & c_1(I_2^2 + Q_2^2) + d_1(I_2^2 + Q_2^2)^2 + e_1(I_1^2 + Q_1^2)(I_2^2 + Q_2^2)] \quad (6.8)
 \end{aligned}$$

and

$$\begin{aligned}
 V_{DPD}^{(2)}(t) = & V_{IN}^{(2)}(t)[1 + a_2(I_2^2 + Q_2^2) + b_2(I_2^2 + Q_2^2)^2 + \\
 & c_2(I_1^2 + Q_1^2) + d_2(I_1^2 + Q_1^2)^2 + e_2(I_1^2 + Q_1^2)(I_2^2 + Q_2^2)] \quad (6.9)
 \end{aligned}$$

When substituting (6.7) instead of (6.4) in (6.1) and (6.2), the new fundamental-frequency signals, in addition to in-band IM and CM terms from (6.5) and (6.6), contain the same in-band IM and CM components with coefficients  $a_1, b_1, c_1, d_1, e_1$  and  $a_2, b_2, c_2, d_2, e_2$ , for each band, respectively. Therefore, the initial distortion from (6.5) and (6.6) can be suppressed by proper tuning of the mentioned coefficients. If the coefficients are set as follows:

$$\begin{aligned} a_1 &= -\frac{3g_3^{(1)}}{4g_1^{(1)}}V_1^2, b_1 = -\frac{5g_5^{(1)}}{8g_1^{(1)}}V_1^4, c_1 = -\frac{3g_3^{(1)}}{2g_1^{(1)}}V_2^2 \\ d_1 &= -\frac{15g_5^{(1)}}{8g_1^{(1)}}V_2^4, e_1 = -\frac{15g_5^{(1)}}{4g_1^{(1)}}V_1^2V_2^2 \end{aligned} \quad (6.10),$$

$$\begin{aligned} a_2 &= -\frac{3g_3^{(2)}}{4g_1^{(2)}}V_2^2, b_2 = -\frac{5g_5^{(2)}}{8g_1^{(2)}}V_2^4, c_2 = -\frac{3g_3^{(2)}}{2g_1^{(2)}}V_1^2 \\ d_2 &= -\frac{15g_5^{(2)}}{8g_1^{(2)}}V_1^4, e_2 = -\frac{15g_5^{(2)}}{4g_1^{(2)}}V_1^2V_2^2 \end{aligned} \quad (6.11),$$

the initial distortion from (6.5) and (6.6) will be compensated for, and  $V_{OUT}^{(1)}(t) \rightarrow g_1^{(1)}V_{IN}^{(1)}(t)$ ,  $V_{OUT}^{(2)}(t) \rightarrow g_1^{(2)}V_{IN}^{(2)}(t)$ . The described simultaneous injection DPD architecture is shown in Figure 6-1. The predistorted  $I_{DPD}^{(1)}, Q_{DPD}^{(1)}, I_{DPD}^{(2)}$  and  $Q_{DPD}^{(2)}$  signals' components are the baseband equivalent of (6.8) and (6.9). The mathematical operations in these equations are restricted to real multiplications and additions only which is significant DPD complexity reduction in comparison with state-of-the-art. Also, the proposed approach requires memory for only six PA polynomial coefficients, three for each frequency band in case of using odd-order polynomial terms. One can see that the technique is derived here for fifth-order polynomial model. In case of using third-order polynomials, it will be only two polynomial coefficients to be adjusted during the characterisation procedure and the performance of PA modelling will be seriously degraded. This was proved in experiments (Section 6.4). It should be noted that even-order polynomial terms can be used in order to increase PA behavioural modelling performances and they do not have a direct impact on fundamental frequency response of the PA. Also, the proposed theory can be extended to be applied for any degree of nonlinearity as will be discussed in Chapter 7.

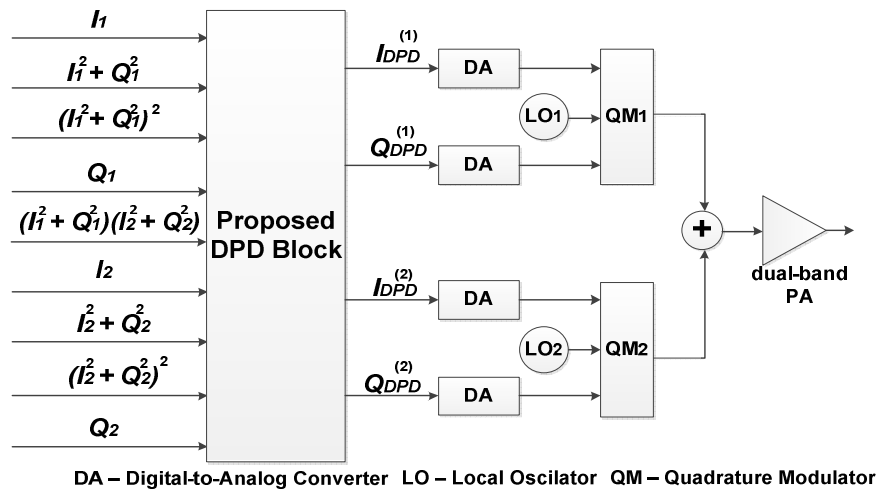


**Figure 6-1:** Functional block diagram of proposed predistorter as a part of concurrent dual-band transmitter

### 6.3. Experimental Setup of Concurrent Dual-band Transmitter

The experimental setup is shown in Figure 6-2. It is consisted of the two signal generators, ESG E4433B and MXG N5182A, used to emulate concurrent dual-band transmitter. The 5-MHz wideband code division multiple access (WCDMA) and 3-MHz long term evolution (LTE) signals were created in Matlab and downloaded to ESG by using Advanced Design System (ADS) and to MXG by using Agilent Signal Studio Toolkit. The combiner was utilised to combine the signals on different frequencies ( $f_1 = 400\text{MHz}$ ,  $f_2 = 500\text{MHz}$ ). The combined signals were passed through Device Under Test (DUT) Mini-Circuits ZFL-500 PA (21 dB gain, P1dB +10 dBm, IP3 +19 dBm) which was driven in hard compression region. The PA output signals were down-converted with Vector Signal Analyzer (VSA) and captured on PC by 89600 VSA software in two steps, one for each band separately. These signals were then time-aligned with corresponding input signals.

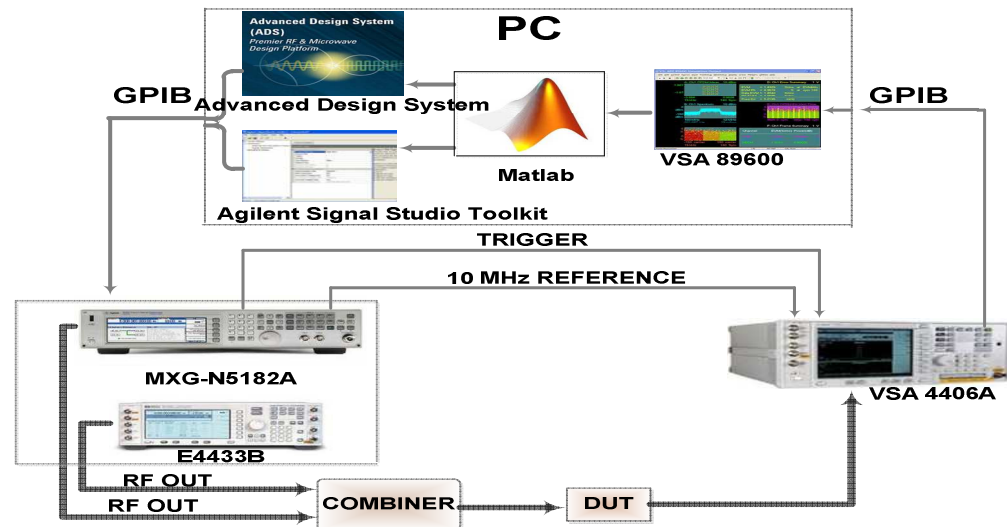
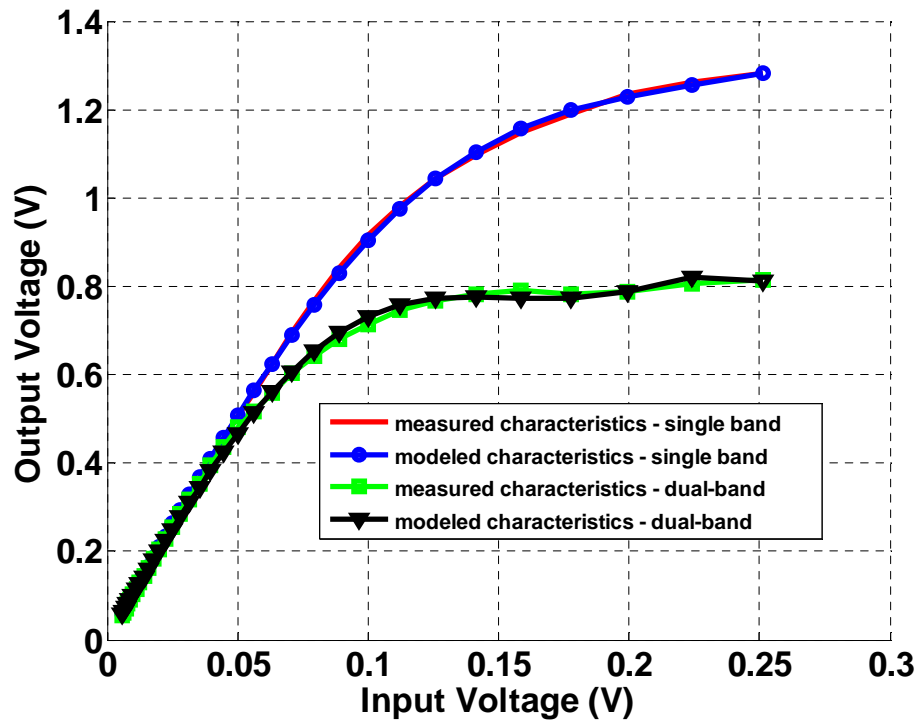


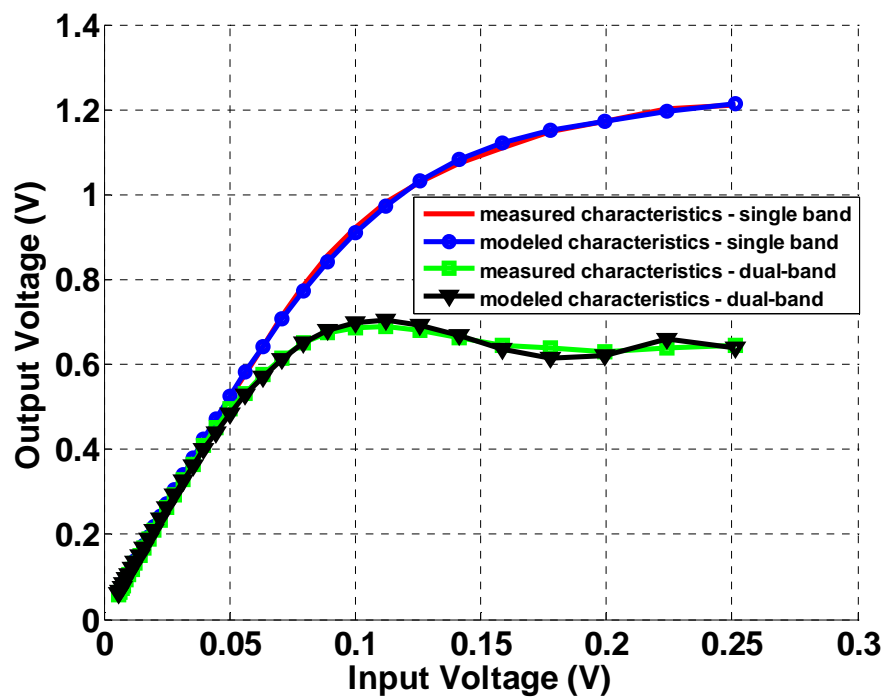
Figure 6-2: Measurement setup of concurrent dual-band transmitter

## 6.4. Proposed Dual-band PA Characterisation

The polynomial models (6.1) and (6.2) of considered DUT were obtained for both frequency bands using continuous wave (CW) measurement procedure. To show difference in nonlinear characteristic, the procedure is applied in both, single and concurrent dual-band transmitter mode. To clarify, when both generators are ON, an experimentally emulated transmitter operates in concurrent dual-band mode. A least square regression (LSR) is used for polynomial fitting of measured data. In case of using third-order polynomials for ZFL-500 PA modelling, mean square error (MSE) was above -30 dB in both frequency bands. These unacceptable PA modelling performances lead to poor DPD performances at the output of concurrent dual-band transmitter. Therefore, the fifth-order polynomials were used in order to decrease MSE below -40 dB. The measured and modelled transfer characteristics as well as measured and modelled PA gain in single band and concurrent dual-band modes are compared in Figure 6-3 and Figure 6-4, respectively. As can be seen, when the PA operates in dual-band mode, the P1dB compression point is notably decreased. In other words, PA nonlinear behaviour will be significantly stronger in dual-band mode. Therefore, PA must be characterised in dual-band mode. Otherwise, using of standard CW characterisation for both bands separately will seriously degrade the performances of proposed DPD. The obtained polynomial coefficients of PA extracted in transmitter dual-band mode were then used for calculating of coefficients of injected IMs and CMs.

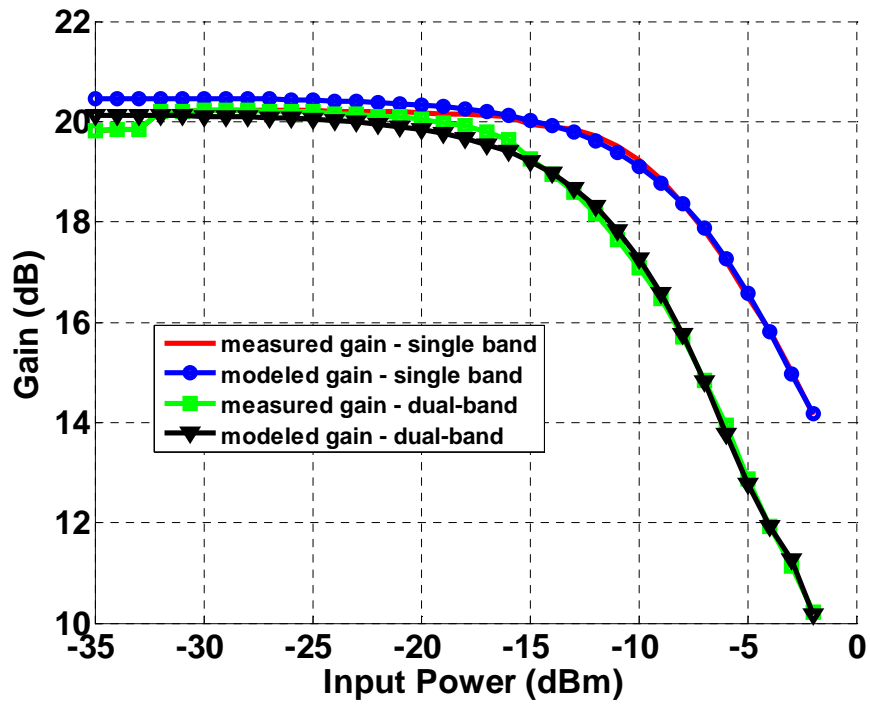


(a)

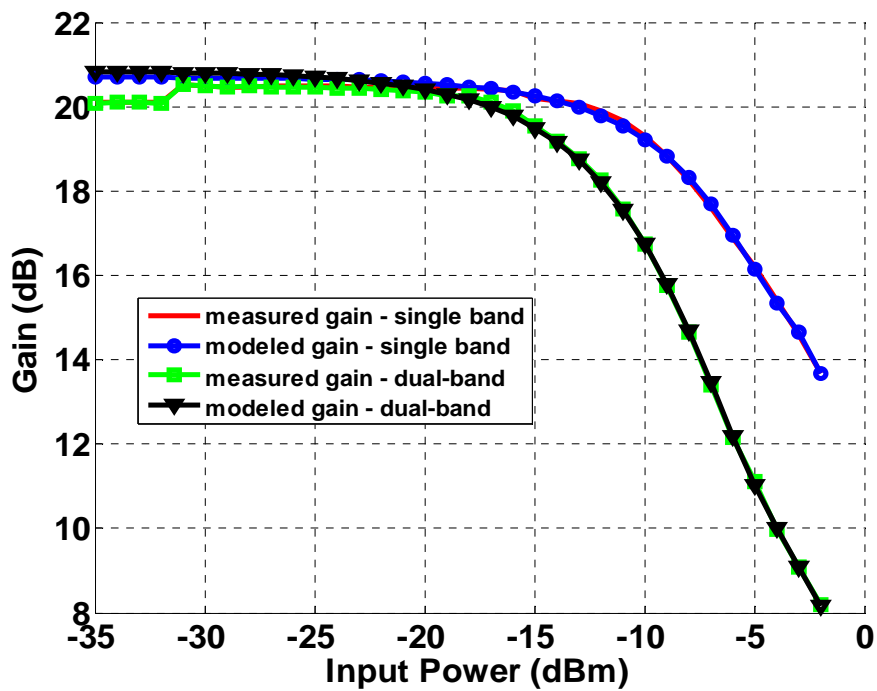


(b)

**Figure 6-3:** Comparisons of measured and modelled ZFL-500 PA transfer characteristics in single and dual-band transmitter mode: (a) operating frequency 400 MHz (b) operating frequency 500 MHz



(a)

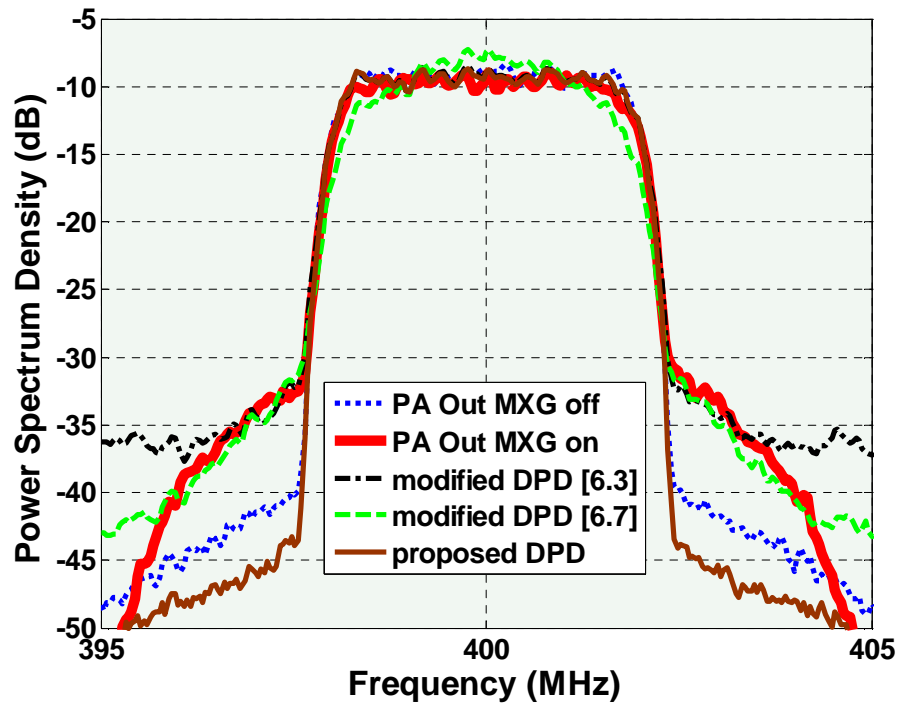


(b)

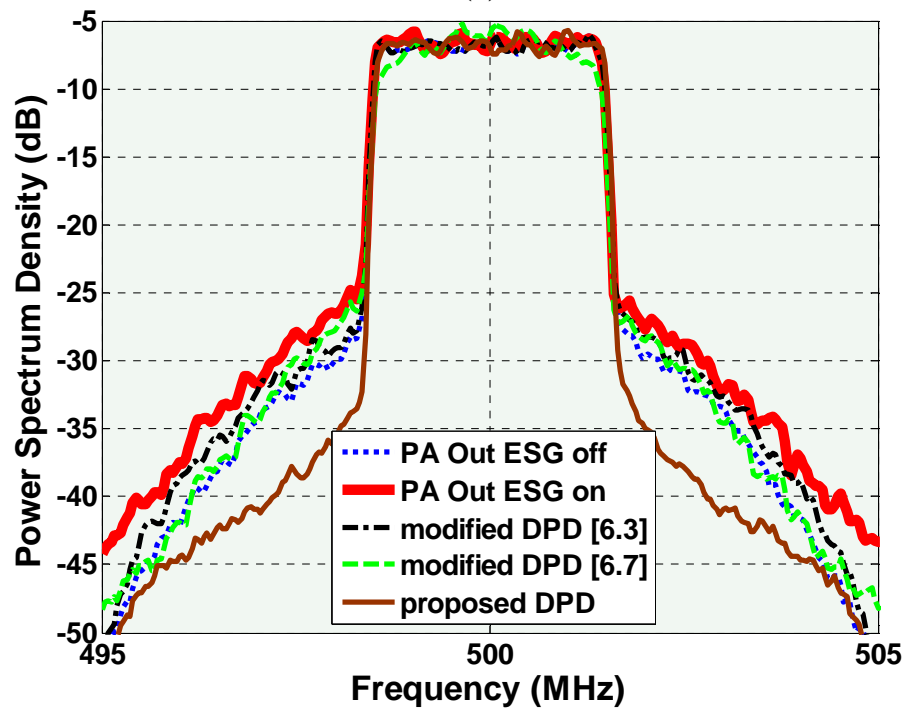
**Figure 6-4:** Comparisons of measured and modelled Gain in single and dual-band transmitter mode: (a) operating frequency 400 MHz (b) operating frequency 500 MHz

## 6.5. Experimental 2-D DPD Results

The described DPD approach has been implemented in Matlab. The predistorted I and Q components for each signal were downloaded to ESG and MXG signal generators. In order to show the effectiveness of the proposed simultaneous injection approach, the existing injection-based DPDs [6.3], [6.7] are also considered. These techniques have not been tested in their original forms due to impractical sampling rate requirements for the DA convertors. In other words, their sampling rates depend on frequency separation in concurrent dual-band transmitter. However, for the testing purpose in this type of transmitter, the approaches [6.3], [6.7] were modified in such a way that they were applied in each band separately. The spectrums of PA output in single-band case without DPD (short dash blue), PA output in concurrent dual-band case without DPD (thicker solid red), and PA output after using modified DPD [6.3] (dash dotted black), modified DPD [6.7] (long dash green) and proposed simultaneous injection DPD (solid brown) are shown in Figure 6-5. As can be seen, the distortion level is significantly higher in concurrent case (both generators ON) in comparison with conventional single-band (one generator OFF). This CM distortion caused by interaction between frequency bands, does not allow using of modified [6.3] and [6.7] in concurrent dual-band transmitters. They cannot compensate for even in-band IM distortion and, worse yet, can degrade performances in some cases. The proposed simultaneous injection of in-band IM and CM distortion products approach improves EVM more than 17 dB and spectrum regrowth more than 10 dB in both operating frequency bands of concurrent dual-band transmitter.



(a)



(b)

**Figure 6-5:** The PSD responses in both operating frequencies of concurrent dual-band transmitter:

(a)  $f_{lower} = 400\text{MHz}$ , (b)  $f_{upper} = 500\text{MHz}$

## 6.6. Conclusion

A new 2-D DPD based on simultaneous injection of the in-band IM and CM distortion components was presented and verified through experiments. To the best knowledge of the author, this is the first 2-D injection-based DPD technique. It has been clearly shown that the technique outperforms conventional injection-based techniques in terms of EVM and PSD performances when they were tested in emulated concurrent dual-band transmitter. The proposed technique does not depend on frequency separation between bands and has low complexity in comparison with state-of-the-art techniques. According to the obtained results, the method can be a serious candidate to be utilised for nonlinearity compensation in modern concurrent dual-band wireless transmitters.

## 6.7. References

- [6.1] **M. Cabarkapa**, N. Neskovic, and D. Budimir, "2-D Nonlinearity Compensation Technique for Concurrent Dual-Band Wireless Transmitters," *IEEE International Microwave Symposium 2013, Seattle, WC, USA*, pp. 1–3, June 2013.
- [6.2] F. Chun-Wah, and K.-K.M. Cheng, "Theoretical and experimental study of amplifier linearization based on harmonic and baseband signal injection technique," *IEEE Trans. Microw. Theory Tech.*, vol.50, no.7, pp.1801-1806, July 2002.
- [6.3] N. Mizusawa, and S. Kusunoki, "Third and fifth order base-band component injection for linearization of the power amplifier in a cellular phone," in *IEEE MTT-S Int. Microw. Symp. Dig.*, pp. 1-4, June 2005.
- [6.4] N. Mizusawa, and S. Kusunoki, "Third- and fifth-order baseband component injection for linearization of the power amplifier in a cellular phone," *IEEE Trans. Microw. Theory Tech.*, vol. 53, no. 4, pp. 3327-3334, April 2005.

- [6.5] M. Xiao, and P. Gardner, "Digital baseband injection techniques to reduce spectral regrowth in power amplifier," in *IEEE MTT-S Int. Microw. Symp. Dig.*, pp.1513-1516, 2008.
- [6.6] M. Thian, M. Xiao, and P. Gardner, "Digital Baseband Predistortion Based Linearized Broadband Inverse Class-E Power Amplifier," *IEEE Trans. Microw. Theory Tech.*, vol.57, no.2, pp.323-328, Feb. 2009.
- [6.7] D. Bondar, and D. Budimir, "A Digital Predistorter for Wireless Transmitters", *Int. J. of RF and Microw. Comput.-Aided Eng.*, vol. 19, no 4, pp. 453 – 459, April 2009.
- [6.8] **M. Cabarkapa**, N. Neskovic, A. Neskovic, and D. Budimir, "Adaptive nonlinearity compensation technique for 4G wireless transmitters," *Electron. Lett.*, vol.48, no.20, pp.1308-1309, Sept. 2012.
- [6.9] S.A. Bassam, M. Helaoui, and F.M. Ghannouchi, "2-D Digital Predistortion (2-D-DPD) Architecture for Concurrent Dual-Band Transmitters," *IEEE Trans. Microw. Theory Tech.*, vol.59, no.10, pp.2547-2553, Oct. 2011.
- [6.10] S.A. Bassam, W. Chen; M. Helaoui, F.M. Ghannouchi , and Z. Feng, "Linearization of Concurrent Dual-Band Power Amplifier Based on 2D-DPD Technique," *IEEE Microw. Wireless Comp. Lett.*, vol.21, no.12, pp.685-687, Dec. 2011.
- [6.11] Y.-J. Liu, J. Zhou, W. Chen, B. Zhou, and F.M. Ghannouchi, "Low-complexity 2D behavioural model for concurrent dual-band power amplifiers," *Electron. Lett.*, vol.48, no.11, pp.620-621, May 2012.
- [6.12] Y.-J. Liu, W. Chen, B. Zhou, J. Zhou, and F.M. Ghannouchi, "2D augmented Hammerstein model for concurrent dual-band power amplifiers," *Electron. Lett.* , vol.48, no.19, pp.1214-1216, Sept. 2012.
- [6.13] J. Moon, P.Saad, J. Son, C. Fager, and B. Kim "2-D Enhanced Hammerstein Behavior Model for Concurrent Dual-Band Power Amplifiers", in *Proc. 42th Eur. Microw. Conf.*, pp. 1249-1252, Oct. 2012.

- [6.14] Z. Huang, W. Chen, Z. Feng, and F.M. Ghannouchi, "Forward behavioral modeling of concurrent dual-band power amplifiers using extended real valued time delay neural networks," in *Int. Microw. Millim. Wave Tech. (ICMMT) Conf.*, pp.1-4, May 2012.

## 7. A Generalised Linearity Enhancement Architecture for Concurrent Dual-band Transmitters

### 7.1. Introduction

A novel generalised iterative 2-D DPD architecture for concurrent dual-band wireless transmitters is described in this Chapter. This generalised injection-based linearisation solution for concurrent dual-band transmitters represents the main contribution of the thesis and was published in [7.1]. This methodology is an extension of the technique described in Chapter 6. The technique is further generalised to any degree of nonlinearity and iterations' number. More specifically, an initial injection approach presented in Chapter 6 is extended here to generalised iterative injection approach, which is used to overcome distortion compensation limit phenomena in concurrent dual-band wireless transmitters caused by initial injection. In other words, the proposed approach is based on simultaneous iterative injection of the in-band IM and CM products. Moreover, in comparison with previously tested memoryless ZFL-500 PA, it has been shown in the experiments that CFH 2162-P3 PA (14 dB gain, P1dB +37 dBm) exhibits memory effects that degrade the performances of the proposed DPD at the output of concurrent dual-band transmitter. The presence of memory effects are detected by concurrent two-tone test and it is reflected as an imbalance between lower and upper third-order in-band IM, near CM and far CM distortion components in both frequency bands. These memory effects caused by frequency dependent behaviour of PA are minimised in frequency domain by using baseband symbol adjustable normalised inverse  $S_{21}$ -parameter parallel multiplication. This procedure is performed separately for both bands of concurrent dual-band transmitter.

The advantages of the proposed linearity enhancement architecture are:

1. simplicity in comparison with state-of-the-art solutions because the proposed one intentionally avoids using of complex polynomials, LUTs, Volterra, or ANN approaches for nonlinearity compensation purposes;

2. capability to deal with distortion compensation limit caused by an initial injection;
3. capability to deal with memory effects;
4. independency on frequency separation between bands.

This Chapter is organised as follows. For the first time, a general fundamental-frequency model for concurrent dual-transmitter was analytically derived and the impact of each distortion component at transmitter output was discussed and demonstrated through baseband equivalent simulations. Next, this chapter describes in detail the proposed linearity enhancement architecture. It explains simultaneous injection of IM and CM distortion products for nonlinearity compensation purposes, overcoming distortion compensation limit phenomena by iterative simultaneous injection of IMs and CMs, as well as memory effects' mitigation part of the proposed 2-D DPD. The experimental results verifying the proposed linearity enhancement architecture are then presented. Finally, the numerous advantages of this 2-D DPD in comparison with the existing 2-D DPD solutions are summarised and discussed.

## 7.2. Fundamental Frequency Model for Concurrent Dual-band Transmitters

The nonlinear behaviour of a PA is modeled by a polynomial expression in both frequency bands of concurrent dual-band transmitter:

$$V_{OUT}^{(1)}(t) = \sum_{k=1}^N g_k^{(1)} V_{IN}^k(t) \quad (7.1)$$

$$V_{OUT}^{(2)}(t) = \sum_{k=1}^M g_k^{(2)} V_{IN}^k(t) \quad (7.2)$$

where  $V_{IN}(t)$  is the PA input signal,  $g_k^{(1)}$  and  $g_k^{(2)}$  are the coefficients of the polynomial models with  $N$  and  $M$  orders in each band, respectively. The PA input signal can be represented as a sum of digitally modulated signals in each band:

$$V_{IN}(t) = V_{IN}^{(1)}(t) + V_{IN}^{(2)}(t) = V_{S1}(t) \cos(\omega_1 t + \varphi_1(t)) + V_{S2}(t) \cos(\omega_2 t + \varphi_2(t)) \quad (7.3)$$

For these digitally modulated signals with variable amplitudes  $V_{S1}(t)$  and  $V_{S2}(t)$  and variable phases  $\varphi_1(t)$  and  $\varphi_2(t)$ , the input signal can be written using the in-phase  $I_1(t)$  and  $I_2(t)$  and quadrature  $Q_1(t)$  and  $Q_2(t)$  components:

$$V_{IN}(t) = \underbrace{V_1(I_1(t) \cos \omega_1 t - Q_1(t) \sin \omega_1 t)}_x + \underbrace{V_2(I_2(t) \cos \omega_2 t - Q_2(t) \sin \omega_2 t)}_y \quad (7.4)$$

where the average value of the amplitudes are  $V_1 = \sqrt{\overline{V_{S1}^2(t)}}$ ,  $V_2 = \sqrt{\overline{V_{S2}^2(t)}}$ , and  $\overline{I_1(t)^2 + Q_1(t)^2} = 1$ ,  $\overline{I_2(t)^2 + Q_2(t)^2} = 1$ .

The total output signal is obtained after substituting (7.4) into (7.1) and (7.2) and applying binomial formula and trigonometric transformations. It can be written as a sum of  $\cos(i\omega_1 \pm j\omega_2)t$  terms, where  $i, j = 0, 1, 2, \dots$ . The terms containing  $\cos(\omega_1 t)$  and  $\cos(\omega_2 t)$  are the undesired fundamental-frequency parts of the output signal related to each band. The other terms are considered to be far enough from the concurrent operating bands, and therefore can be easily filtered out. An analytical form of the each term containing  $\cos(\omega_1 t)$  and  $\cos(\omega_2 t)$  caused by PA nonlinearity up to order 9 is given in Table 7-1. To demonstrate which term after applying binomial expansion is cause of each distortion component, the graphical representation in Figure 7-1 is used. The first triangle is a Pascal triangle of binomial coefficients. The nonlinear terms after algebraic expansion of powers of a binomial are given in second triangle. Finally, the third triangle gives position of each distortion component in terms of its cause. For instance, term  $1 \cdot x^3$  causes third-order IM component in first band ( $IM_3^{(1)}$ ), while  $3 \cdot xy^2$  causes third-order CM component ( $CM_{31}^{(1)}$ ). Apart from the desired linear parts  $g_1^{(1)} V_{IN}^{(1)}(t)$  and  $g_1^{(2)} V_{IN}^{(2)}(t)$ , the fundamental-frequency output signals contain sum of distortion components from all the odd-order terms of the polynomial models. In addition to IM distortion specific for the conventional transmitters, they contain CM products caused by interaction between frequency bands in concurrent dual-band transmitters. A general fundamental frequency model for concurrent dual-band transmitter can be derived deductively from Table I.

**TABLE 7-1:** Analytical forms of IM and CM distortion components

Distortion Component	Analytical Form (RF)
$IM_3^{(1)}$	$\frac{3}{4}g_3^{(1)}V_1^2(I_1^2 + Q_1^2)V_{IN}^{(1)}(t)$
$IM_3^{(2)}$	$\frac{3}{4}g_3^{(2)}V_2^2(I_2^2 + Q_2^2)V_{IN}^{(2)}(t)$
$CM_{31}^{(1)}$	$\frac{3}{2}g_3^{(1)}V_2^2(I_2^2 + Q_2^2)V_{IN}^{(1)}(t)$
$CM_{31}^{(2)}$	$\frac{3}{2}g_3^{(2)}V_1^2(I_1^2 + Q_1^2)V_{IN}^{(2)}(t)$
$IM_5^{(1)}$	$\frac{5}{8}g_5^{(1)}V_1^4(I_1^2 + Q_1^2)^2V_{IN}^{(1)}(t)$
$IM_5^{(2)}$	$\frac{5}{8}g_5^{(2)}V_2^4(I_2^2 + Q_2^2)^2V_{IN}^{(2)}(t)$
$CM_{51}^{(1)}$	$\frac{15}{4}g_5^{(1)}V_1^2V_2^2(I_1^2 + Q_1^2)(I_2^2 + Q_2^2)V_{IN}^{(1)}(t)$
$CM_{52}^{(1)}$	$\frac{15}{8}g_5^{(1)}V_2^4(I_2^2 + Q_2^2)^2V_{IN}^{(1)}(t)$
$CM_{51}^{(2)}$	$\frac{15}{4}g_5^{(2)}V_1^2V_2^2(I_1^2 + Q_1^2)(I_2^2 + Q_2^2)V_{IN}^{(2)}(t)$
$CM_{52}^{(2)}$	$\frac{15}{8}g_5^{(2)}V_1^4(I_1^2 + Q_1^2)^2V_{IN}^{(2)}(t)$
$IM_7^{(1)}$	$\frac{35}{64}g_7^{(1)}V_1^6(I_1^2 + Q_1^2)^3V_{IN}^{(1)}(t)$
$IM_7^{(2)}$	$\frac{35}{64}g_7^{(2)}V_2^6(I_2^2 + Q_2^2)^3V_{IN}^{(2)}(t)$
$CM_{71}^{(1)}$	$\frac{105}{8}g_7^{(1)}V_1^4V_2^2(I_1^2 + Q_1^2)^2(I_2^2 + Q_2^2)V_{IN}^{(1)}(t)$
$CM_{72}^{(1)}$	$\frac{105}{4}g_7^{(1)}V_1^2V_2^4(I_1^2 + Q_1^2)(I_2^2 + Q_2^2)^2V_{IN}^{(1)}(t)$
$CM_{73}^{(1)}$	$\frac{35}{16}g_7^{(1)}V_2^6(I_2^2 + Q_2^2)^3V_{IN}^{(1)}(t)$
$CM_{71}^{(2)}$	$\frac{105}{8}g_7^{(2)}V_1^2V_2^4(I_1^2 + Q_1^2)(I_2^2 + Q_2^2)^2V_{IN}^{(2)}(t)$
$CM_{72}^{(2)}$	$\frac{105}{4}g_7^{(2)}V_1^4V_2^2(I_1^2 + Q_1^2)^2(I_2^2 + Q_2^2)V_{IN}^{(2)}(t)$
$CM_{73}^{(2)}$	$\frac{35}{16}g_7^{(2)}V_1^6(I_1^2 + Q_1^2)^3V_{IN}^{(2)}(t)$
$IM_9^{(1)}$	$\frac{63}{128}g_9^{(1)}V_1^8(I_1^2 + Q_1^2)^4V_{IN}^{(1)}(t)$
$IM_9^{(2)}$	$\frac{63}{128}g_9^{(2)}V_2^8(I_2^2 + Q_2^2)^4V_{IN}^{(2)}(t)$
$CM_{91}^{(1)}$	$\frac{315}{32}g_9^{(1)}V_1^6V_2^2(I_1^2 + Q_1^2)^3(I_2^2 + Q_2^2)V_{IN}^{(1)}(t)$
$CM_{92}^{(1)}$	$\frac{945}{32}g_9^{(1)}V_1^4V_2^4(I_1^2 + Q_1^2)^2(I_2^2 + Q_2^2)^2V_{IN}^{(1)}(t)$
$CM_{93}^{(1)}$	$\frac{315}{16}g_9^{(1)}V_1^2V_2^6(I_1^2 + Q_1^2)(I_2^2 + Q_2^2)^3V_{IN}^{(1)}(t)$
$CM_{94}^{(1)}$	$\frac{207}{128}g_9^{(1)}V_2^8(I_2^2 + Q_2^2)^4V_{IN}^{(1)}(t)$
$CM_{91}^{(2)}$	$\frac{315}{32}g_9^{(2)}V_1^2V_2^6(I_1^2 + Q_1^2)(I_2^2 + Q_2^2)^3V_{IN}^{(2)}(t)$
$CM_{92}^{(2)}$	$\frac{945}{32}g_9^{(2)}V_1^4V_2^4(I_1^2 + Q_1^2)^2(I_2^2 + Q_2^2)^2V_{IN}^{(2)}(t)$
$CM_{93}^{(2)}$	$\frac{315}{16}g_9^{(2)}V_1^6V_2^2(I_1^2 + Q_1^2)^3(I_2^2 + Q_2^2)V_{IN}^{(2)}(t)$
$CM_{94}^{(2)}$	$\frac{207}{128}g_9^{(2)}V_1^8(I_1^2 + Q_1^2)^4V_{IN}^{(2)}(t)$

It looks as follows:

$$\begin{aligned}
 V_{OUT}^{FUND(1)}(t) = & g_1^{(1)} V_{IN}^{(1)}(t) + \left( \sum_{k=1}^{\lfloor N/2 \rfloor} a_{2k+1}^{(1)} V_1^{2k} g_{2k+1}^{(1)} (I_1^2 + Q_1^2)^k \right) V_{IN}^{(1)}(t) \\
 & + \left( \sum_{k=1}^{\lfloor N/2 \rfloor} \sum_{l=1}^k b_{2k+1,l}^{(1)} V_1^{2(k-l)} V_2^{2l} (I_1^2 + Q_1^2)^{k-l} (I_2^2 + Q_2^2)^l \right) V_{IN}^{(1)}(t)
 \end{aligned} \tag{7.5}$$

and

$$\begin{aligned}
 V_{OUT}^{FUND(2)}(t) = & g_1^{(2)} V_{IN}^{(2)}(t) + \left( \sum_{k=1}^{\lfloor M/2 \rfloor} a_{2k+1}^{(2)} V_2^{2k} g_{2k+1}^{(2)} (I_2^2 + Q_2^2)^k \right) V_{IN}^{(2)}(t) \\
 & + \left( \sum_{k=1}^{\lfloor M/2 \rfloor} \sum_{l=1}^k b_{2k+1,l}^{(2)} V_2^{2(k-l)} V_1^{2l} (I_2^2 + Q_2^2)^{k-l} (I_1^2 + Q_1^2)^l \right) V_{IN}^{(2)}(t)
 \end{aligned} \tag{7.6}$$

To explain, the second terms in (7.5) and (7.6) are a sum of in-band IM products up to order  $N$  and  $M$ , whereas the third terms are a sum of CM products also up to order  $N$  and  $M$ , for each band respectively. The coefficients near IMs ( $a_{2k+1}^{(1)}$  and  $a_{2k+1}^{(2)}$ ) and CMs ( $b_{2k+1,l}^{(1)}$  and  $b_{2k+1,l}^{(2)}$ ) can be calculated as a multiplication of related binomial coefficient (see Pascal triangle in Figure 7-1) and rational number appeared after trigonometric transformations.

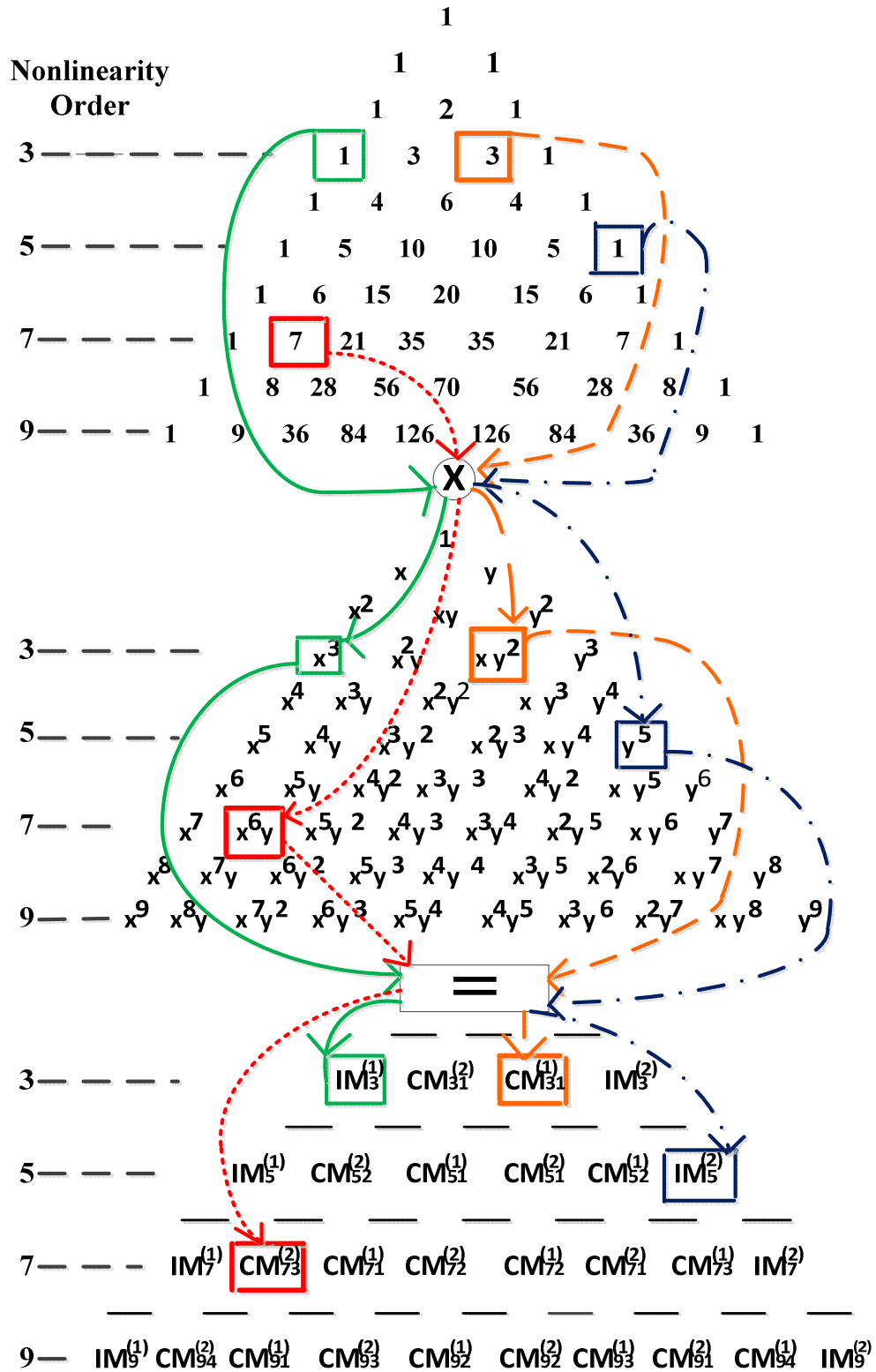
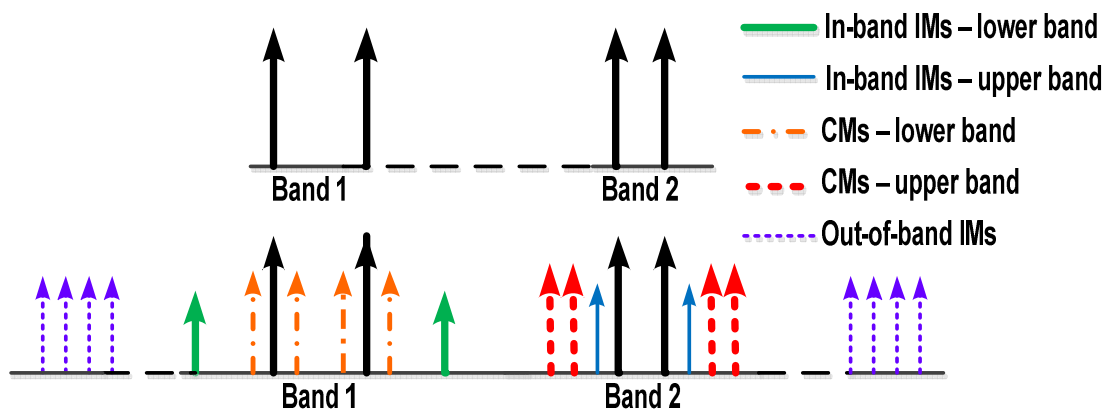


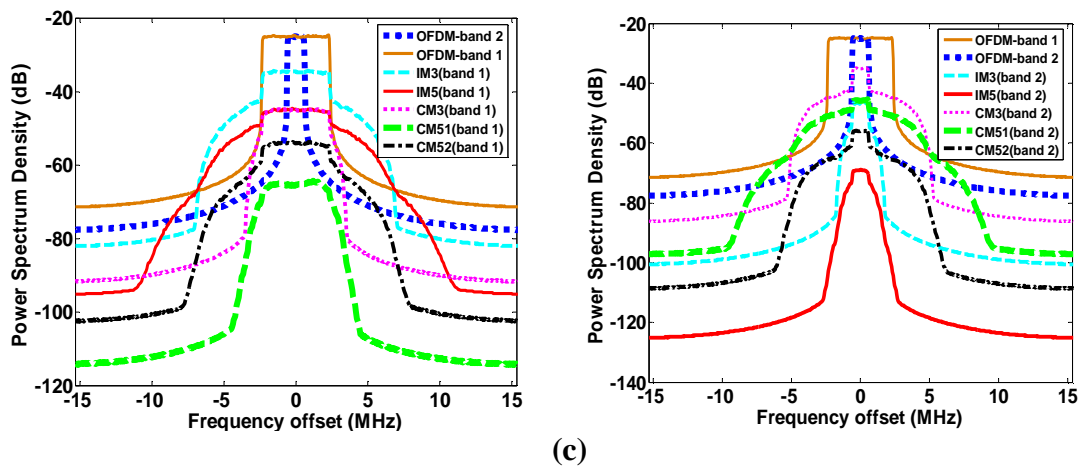
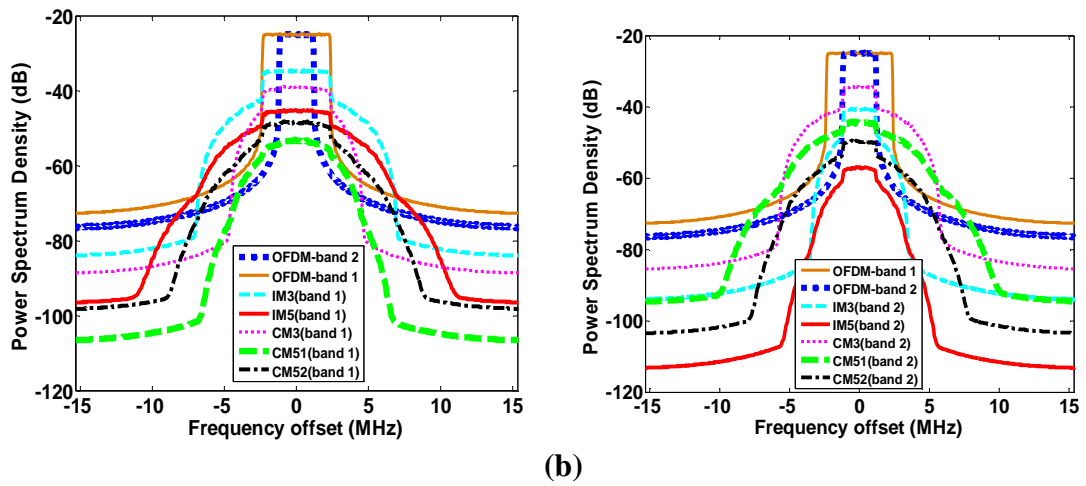
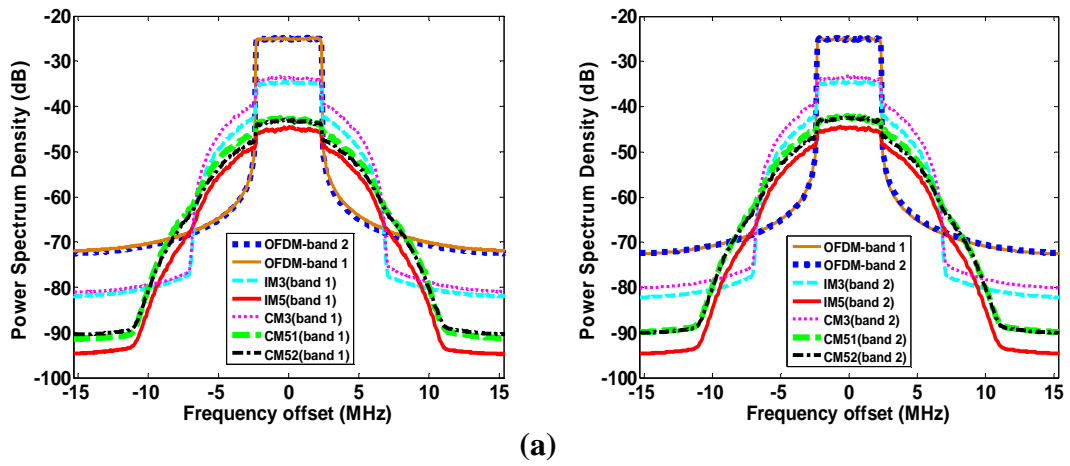
Figure 7-1: The cause of IM and CM distortion components

### 7.3. Baseband Simulation Analysis

The two-tone stimulus and response in concurrent dual-band transmitter are given in Figure 7-2. As can be seen, there are four types of undesired distortion products on discrete frequencies: in-band IM and CM distortion in lower and upper band, respectively. However, an analysis of undesired distortion products in case of two digitally modulated signals is much more complex. An in-band and out-of-band impacts of each distortion component can be determined using baseband analysis in frequency domain. For comparison, PSDs of third- and fifth- order distortion components from Table 7-1 are calculated. Baseband simulations for four different signal sets with variable ratio between occupied bandwidths of signals (BW1 and BW2) and their powers (PW1 and PW2) are performed. The calculated PSDs are shown in Figure 7-3. As can be seen, the CM distortion products are dominant for the signals with narrower bandwidth and lower power, and vice versa, in-band IM distortion products are dominant for the signals with wider bandwidth and higher power. In other words, an increase of bandwidth or power of signal in one frequency band is reflected as an increase of CMs impact in another one. Additionally, it is noted during the simulations that an increase of bandwidth dominantly rise an out-of-band impact of CMs whereas an increase of power dominantly rise an in-band impact of CMs. It is interesting that when two signals with equal bandwidth and power are transmitted (Figure 7-3a), CM components have a greater impact than IM components in the output signals of concurrent dual-band transmitters. This analysis can be very useful in order to simplify design of predistorter for each band of concurrent dual-band transmitter.



**Figure 7-2:** Power spectrum at the input and output of a dual-band transmitter (concurrent two-tone test)



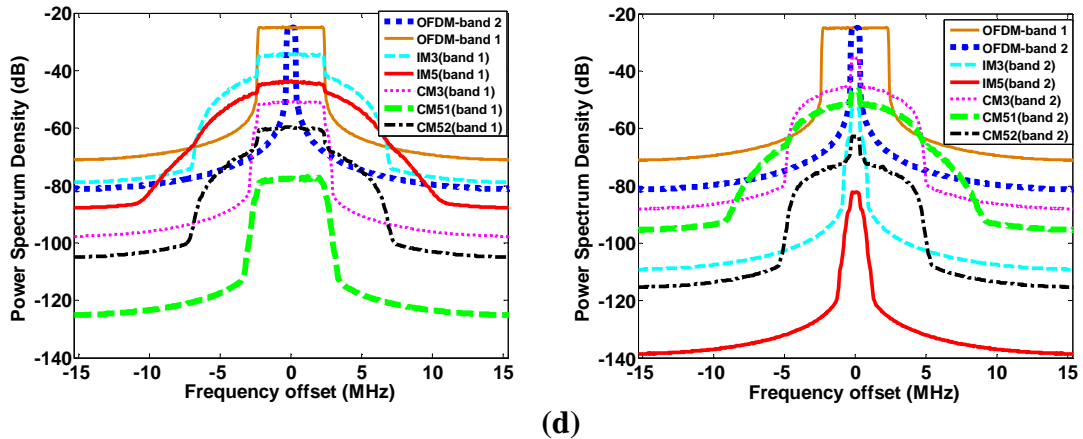


**Figure 7-3:** Comparisons of simulated IM and CM distortion components for OFDM signals with variable ratio between occupied bandwidths of signals (BW1 and BW2) and their powers (PW1 and PW2): (a)  $BW1/BW2 = 1, PW1/PW2 = 1$  (b)  $BW1/BW2 = 2, PW1/PW2 = 2$  (c)  $BW1/BW2 = 4, PW1/PW2 = 4$  (d)  $BW1/BW2 = 8, PW1/PW2 = 8$ .

### 7.4. Proposed Generalised DPD System

The proposed DPD system implies a separate compensation of nonlinear distortion and memory effects. In this paper, the presented predistorter is designed according to Wiener structure where memory mitigation block is in front of nonlinearity compensation (Figure 7-4).

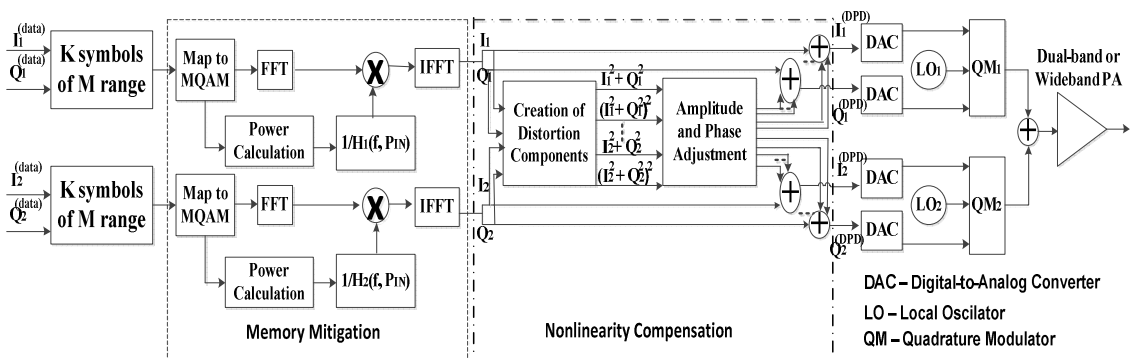


**Figure 7-4:** Functional block diagram of proposed predistorter as a part of concurrent dual-band transmitter

### 7.4.1. Nonlinearity Compensation by Simultaneous Injection

In order to compensate for these distortions, a simultaneous injection of the in-band IM together with CM products, all with opposite phases, is proposed for both frequency bands in concurrent dual-band transmitter. The total predistorter output signal with injected in-band IM and CM distortion components consists of the two terms related to each frequency band:

$$V_{DPD}(t) = V_{DPD}^{(1)}(t) + V_{DPD}^{(2)}(t) \quad (7.7)$$

where

$$V_{DPD}^{(1)}(t) = V_{IN}^{(1)}(t) \left( 1 + \sum_{k=1}^{\lfloor N/2 \rfloor} \sum_{l=0}^k c_{2k+1,l}^{(1)} (I_1^2 + Q_1^2)^{k-l} (I_2^2 + Q_2^2)^l \right) \quad (7.8)$$

$$V_{DPD}^{(2)}(t) = V_{IN}^{(2)}(t) \left( 1 + \sum_{k=1}^{\lfloor M/2 \rfloor} \sum_{l=0}^k c_{2k+1,l}^{(2)} (I_2^2 + Q_2^2)^{k-l} (I_1^2 + Q_1^2)^l \right) \quad (7.9)$$

To clarify, the coefficients  $c_{2k+1,0}^{(1)}$  and  $c_{2k+1,0}^{(2)}$  are related to injected in-band IMs while  $c_{2k+1,l}^{(1)}$  and  $c_{2k+1,l}^{(2)}$ , with  $l \neq 0$  are related to injected CMs. When substituting (7.7) instead of (7.4) in (7.1) and (7.2), the new fundamental-frequency signals, in addition to in-band IM and CM terms from (7.5) and (7.6), contain the same in-band IM and CM components with coefficients  $c_{2k+1,l}^{(1)}$  and  $c_{2k+1,l}^{(2)}$  for each band, respectively. Therefore, the initial distortion from (7.5) and (7.6) can be suppressed by proper tuning of the mentioned coefficients. If the coefficients are set as follows:

$$\begin{aligned} c_{2k+1,0}^{(1)} &= -\frac{a_{2k+1}^{(1)} g_{2k+1}^{(1)}}{g_1^{(1)}} V_1^{2k}, & c_{2k+1,0}^{(2)} &= -\frac{a_{2k+1}^{(2)} g_{2k+1}^{(2)}}{g_1^{(2)}} V_2^{2k}, \\ c_{2k+1,l}^{(1)} &= -\frac{b_{2k+1}^{(1)} g_{2k+1}^{(1)}}{g_1^{(1)}} V_1^{2(k-l)} V_2^{2l}, \quad l \neq 0 & c_{2k+1,l}^{(2)} &= -\frac{b_{2k+1}^{(2)} g_{2k+1}^{(2)}}{g_1^{(2)}} V_2^{2(k-l)} V_1^{2l}, \quad l \neq 0 \end{aligned} \quad (7.10)$$

the initial distortion from (7.5) and (7.6) will be compensated for. The described nonlinearity compensation part of the proposed DPD architecture based on simultaneous injection is shown in Figure 7-4. The injected in-band IM and CM distortion components are created and passed to “Amplitude and Phase Adjustment” block where  $c_{2k+1,l}^{(1)}$  and  $c_{2k+1,l}^{(2)}$  are tuned using (7.10). The predistorted  $I_1^{(DPD)}$ ,  $Q_1^{(DPD)}$ ,  $I_2^{(DPD)}$  and  $Q_2^{(DPD)}$  signals’ components are the baseband equivalent of (7.8) and (7.9) and they are created as follows:

$$\begin{aligned}
 I_1^{(DPD)} &= I_1 \left( 1 + \sum_{k=1}^{\lfloor N/2 \rfloor} \sum_{l=0}^k c_{2k+1,l}^{(1)} (I_1^2 + Q_1^2)^{k-l} (I_2^2 + Q_2^2)^l \right) \\
 Q_1^{(DPD)} &= Q_1 \left( 1 + \sum_{k=1}^{\lfloor N/2 \rfloor} \sum_{l=0}^k c_{2k+1,l}^{(1)} (I_1^2 + Q_1^2)^{k-l} (I_2^2 + Q_2^2)^l \right) \\
 I_2^{(DPD)} &= I_2 \left( 1 + \sum_{k=1}^{\lfloor M/2 \rfloor} \sum_{l=0}^k c_{2k+1,l}^{(2)} (I_2^2 + Q_2^2)^{k-l} (I_1^2 + Q_1^2)^l \right) \\
 Q_2^{(DPD)} &= Q_2 \left( 1 + \sum_{k=1}^{\lfloor M/2 \rfloor} \sum_{l=0}^k c_{2k+1,l}^{(2)} (I_2^2 + Q_2^2)^{k-l} (I_1^2 + Q_1^2)^l \right)
 \end{aligned} \tag{7.11}$$

The mathematical operations in these equations are restricted to real multiplications and additions only, which is significant DPD complexity reduction in comparison with state-of-the-art.

#### 7.4.2. Iterative Simultaneous Injection

The injected components generate new distortion products while compensating for the initial distortion. This phenomenon is known as the distortion compensation limit and its impact could degrade performances of injection-based predistorter [7.2]. To demonstrate this phenomenon in concurrent dual-band transmitter, an injection of third-order in-band IM in first band and third-order CM in second band will be applied. The predistorted signals can be written as follows:

$$V_{DPD}^{(1)}(t) = V_{IN}^{(1)}(t)(1 + c_{3,0}^{(1)}(I_1^2 + Q_1^2)) \quad (7.12)$$

and

$$V_{DPD}^{(2)}(t) = V_{IN}^{(2)}(t)(1 + c_{3,1}^{(2)}(I_1^2 + Q_1^2)) \quad (7.13).$$

By substituting (7.12) and (7.13) into (7.7), and (7.7) into (7.1) with  $N=3$ , the distorted PA output at fundamental frequency of first band can be expressed as in (7.14)

$$\begin{aligned} V_{OUT}^{FUND(1)}(t) = & g_1^{(1)}V_{IN}^{(1)}(t) + \left(\frac{3}{4}g_3^{(1)}V_1^2 + g_1^{(1)}c_{3,0}^{(1)}\right)(I_1^2 + Q_1^2)V_{IN}^{(1)}(t) + \frac{3}{2}g_3^{(1)}V_2^2(I_2^2 + \\ & Q_2^2)V_{IN}^{(1)}(t) + \frac{9}{4}g_3^{(1)}V_1^2c_{3,0}^{(1)}(I_1^2 + Q_1^2)^2V_{IN}^{(1)}(t) + 3g_3^{(1)}\left(\frac{1}{2}c_{3,0}^{(1)} + c_{3,1}^{(2)}\right)V_2^2(I_1^2 + Q_1^2)(I_2^2 + \\ & Q_2^2)V_{IN}^{(1)}(t) \end{aligned} \quad (7.14)$$

As can be seen, in addition to third-order IM and CM, two fifth-order distortion components appear. They are results of initial injected signal and have only different coefficients in comparison with fifth-order IM and CM. These two components are distortion compensation limit. To clarify, there are another five distortion components (three seven-order and two nine-order) that are omitted from (7.14) because they have very low amplitudes and their impact is negligible. Therefore, distortion compensation limit in concurrent dual band transmitter can be defined as distortion components of order  $2k+3$ , which are results of initial injection and appear at fundamental frequency, where  $2k+1$  is the order of initially injected components. The main idea of the iterative injection approach is to recalculate new distortion products at fundamental frequency of PA that result from the initial injected signal. After this step, an injection of these products together with initial injected signals is applied. Tuning of the amplitudes and phases of these new injected distortion products depends on coefficients that are tuned in the initial step to compensate for initial distortions that are a result of PA nonlinear behaviour.

As can be seen from (7.14), new distortion components in the first band, which are results of initial injection, depend on injected components in both bands. Therefore,

tuning of the amplitudes and phases of these new distortion products depends on both,  $c_{2k+1,l}^{(1)}$  and  $c_{2k+1,l}^{(2)}$ . The generalised model of the tuned coefficients at first frequency band of concurrent dual-band transmitter in the  $m$ -th iteration,  $c_{2k+1,l,m}^{(1)}$ , in addition to calculated  $a_{2k+1,m}^{(1)}$  and  $b_{2k+1,l,m}^{(1)}$ , is a function of  $c_{2k+1,l,m-1}^{(1)}$  and  $c_{2k+1,l,m-1}^{(2)}$ . To explain, the distortion compensation limit in concurrent dual-band transmitter can be overcome using general iterative procedure described by following steps:

1. injecting the odd-order IM and CM distortion components into the original input signal at baseband and calculate fundamental frequency response in each band;
2. injecting calculated new distortions caused by initial injection together with previously injected one and tuning of their  $c_{2k+1,l,m}^{(1)}$  and  $c_{2k+1,l,m}^{(2)}$  where  $m$  is iteration index;
3. repeating steps 1 and 2 until the performance improvement could be observed.

The steps mentioned previously can be applied to any degree of PA nonlinearity and iterations' number depends on PA model and specified performances in concrete case.

### 7.4.3. Memory Effects Mitigation

For the compensation of memory effects in concurrent dual-band transmitter, the memory mitigation technique in frequency domain is incorporated in the proposed predistorter shown in Figure 7-4. As can be seen, the same procedure is done for both frequency bands separately. The memory effects of concurrent dual-band transmitter are represented by linear filters, which are characterised by the frequency responses  $H_1(f, Pin)$  and  $H_2(f, Pin)$  dependent on the PA instantaneous power level because PAs exhibit different frequency-dependent behaviour at different power levels, which are a direct consequence of memory effects (see [7.3] and references therein). To compensate for this frequency dependent behaviour, the proposed approach uses multiplying the complex baseband symbols by the complex coefficients  $1/H_1(f, Pin)$  and  $1/H_2(f, Pin)$  for each frequency band, respectively. Complex values of the frequency response can be

obtained directly from the gain and phase dependences on the modulation frequency. The PA frequency responses should be normalised in order not to affect the mean power levels. In other words, the mentioned complex coefficients are actually normalised inverse  $S_{21}^{(1)}$  and  $S_{21}^{(2)}$  parameters of PA related to each band of interest and instantaneous PA input power level. That power level depends on baseband power level of modulation point. To make the system adaptive to the input power level, the complex values of the  $1/H_1(f, P_{in})$  and  $1/H_2(f, P_{in})$  at all power levels are calculated:

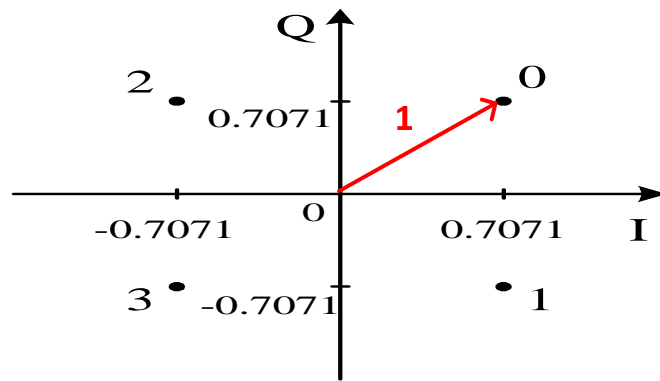
1. For BPSK, the baseband power level is constant, and hence the number of stored coefficients equals to the number of frequency points used for algorithm  $K$ .
2. For QPSK, there is also one power level (Figure 7-5a), and hence the number of stored coefficients also equals to the number of frequency points  $K$ .
3. For 16-QAM, three baseband power levels are utilised (Figure 7-5b), which means the number of stored coefficients equals  $3K$ .
4. For 64-QAM,  $10K$  coefficients are required because 64-QAM has 10 different baseband power levels.

The PA instantaneous input amplitude of each baseband modulation point can be easily determined as follows:

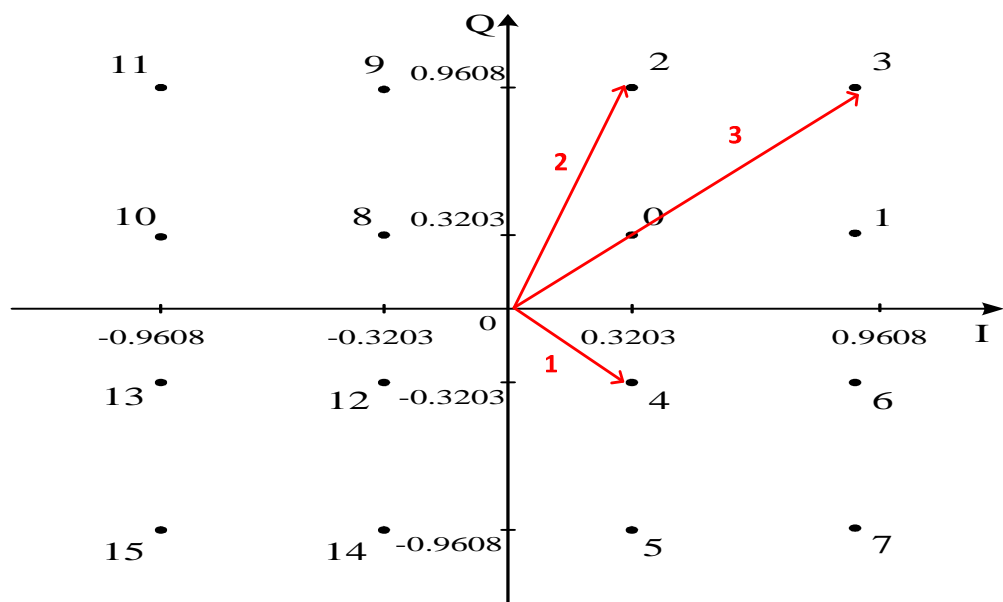
$$V_{IN}(t) = V_{LO}(\sqrt{I^2(t) + Q^2(t)}) \quad (7.15)$$

where  $V_{LO}$  is carrier voltage of local oscillator and average input power of PA depends on its adjustment. The following four tables show the baseband voltage levels of in-phase and quadrature signal components for different modulation mappings [7.4].

In case of BPSK modulation, a single bit is mapped to a complex-valued modulation symbol  $x=I+jQ$  according to Table 7-2.



(a)



(b)

**Figure 7-5:** Baseband voltage levels of I and Q components: (a) QPSK (b) 16-QAM

**TABLE 7-2: BPSK modulation mapping**

$b(i)$	$I$	$Q$
0	$1/\sqrt{2}$	$1/\sqrt{2}$
1	$-1/\sqrt{2}$	$-1/\sqrt{2}$

In case of QPSK modulation, pairs of bits are mapped to complex-valued modulation symbols  $x=I+jQ$  according to Table 7-3.

**TABLE 7-3: QPSK modulation mapping**

$b(i), b(i+1)$	$I$	$Q$
00	$1/\sqrt{2}$	$1/\sqrt{2}$
01	$1/\sqrt{2}$	$-1/\sqrt{2}$
10	$-1/\sqrt{2}$	$1/\sqrt{2}$
11	$-1/\sqrt{2}$	$-1/\sqrt{2}$

In case of 16-QAM modulation, quadruplets of bits are mapped to complex-valued modulation symbols  $x=I+jQ$  according to Table 7-4.

**TABLE 7-4: 16-QAM modulation mapping**

$b(i), b(i+1), b(i+2), b(i+3)$	$I$	$Q$
0000	$1/\sqrt{10}$	$1/\sqrt{10}$
0001	$1/\sqrt{10}$	$3/\sqrt{10}$
0010	$3/\sqrt{10}$	$1/\sqrt{10}$
0011	$3/\sqrt{10}$	$3/\sqrt{10}$
0100	$1/\sqrt{10}$	$-1/\sqrt{10}$
0101	$1/\sqrt{10}$	$-3/\sqrt{10}$
0110	$3/\sqrt{10}$	$-1/\sqrt{10}$
0111	$3/\sqrt{10}$	$-3/\sqrt{10}$
1000	$-1/\sqrt{10}$	$1/\sqrt{10}$
1001	$-1/\sqrt{10}$	$3/\sqrt{10}$
1010	$-3/\sqrt{10}$	$1/\sqrt{10}$
1011	$-3/\sqrt{10}$	$3/\sqrt{10}$
1100	$-1/\sqrt{10}$	$-1/\sqrt{10}$
1101	$-1/\sqrt{10}$	$-3/\sqrt{10}$
1110	$-3/\sqrt{10}$	$-1/\sqrt{10}$
1111	$-3/\sqrt{10}$	$-3/\sqrt{10}$

In case of 64QAM modulation, hexuplets of bits are mapped to complex-valued modulation symbols  $x=I+jQ$  according to Table 7-5.

**TABLE 7-5:** 64-QAM modulation mapping

$b(i), b(i+1), b(i+2), b(i+3), b(i+4), b(i+5)$	$I$	$Q$	$b(i), b(i+1), b(i+2), b(i+3), b(i+4), b(i+5)$	$I$	$Q$
000000	$3/\sqrt{42}$	$3/\sqrt{42}$	100000	$-3/\sqrt{42}$	$3/\sqrt{42}$
000001	$3/\sqrt{42}$	$1/\sqrt{42}$	100001	$-3/\sqrt{42}$	$1/\sqrt{42}$
000010	$1/\sqrt{42}$	$3/\sqrt{42}$	100010	$-1/\sqrt{42}$	$3/\sqrt{42}$
000011	$1/\sqrt{42}$	$1/\sqrt{42}$	100011	$-1/\sqrt{42}$	$1/\sqrt{42}$
000100	$3/\sqrt{42}$	$5/\sqrt{42}$	100100	$-3/\sqrt{42}$	$5/\sqrt{42}$
000101	$3/\sqrt{42}$	$7/\sqrt{42}$	100101	$-3/\sqrt{42}$	$7/\sqrt{42}$
000110	$1/\sqrt{42}$	$5/\sqrt{42}$	100110	$-1/\sqrt{42}$	$5/\sqrt{42}$
000111	$1/\sqrt{42}$	$7/\sqrt{42}$	100111	$-1/\sqrt{42}$	$7/\sqrt{42}$
001000	$5/\sqrt{42}$	$3/\sqrt{42}$	101000	$-5/\sqrt{42}$	$3/\sqrt{42}$
001001	$5/\sqrt{42}$	$1/\sqrt{42}$	101001	$-5/\sqrt{42}$	$1/\sqrt{42}$
001010	$7/\sqrt{42}$	$3/\sqrt{42}$	101010	$-7/\sqrt{42}$	$3/\sqrt{42}$
001011	$7/\sqrt{42}$	$1/\sqrt{42}$	101011	$-7/\sqrt{42}$	$1/\sqrt{42}$
001100	$5/\sqrt{42}$	$5/\sqrt{42}$	101100	$-5/\sqrt{42}$	$5/\sqrt{42}$
001101	$5/\sqrt{42}$	$7/\sqrt{42}$	101101	$-5/\sqrt{42}$	$7/\sqrt{42}$
001110	$7/\sqrt{42}$	$5/\sqrt{42}$	101110	$-7/\sqrt{42}$	$5/\sqrt{42}$
001111	$7/\sqrt{42}$	$7/\sqrt{42}$	101111	$-7/\sqrt{42}$	$7/\sqrt{42}$
010000	$3/\sqrt{42}$	$-3/\sqrt{42}$	110000	$-3/\sqrt{42}$	$-3/\sqrt{42}$
010001	$3/\sqrt{42}$	$-1/\sqrt{42}$	110001	$-3/\sqrt{42}$	$-1/\sqrt{42}$
010010	$1/\sqrt{42}$	$-3/\sqrt{42}$	110010	$-1/\sqrt{42}$	$-3/\sqrt{42}$
010011	$1/\sqrt{42}$	$-1/\sqrt{42}$	110011	$-1/\sqrt{42}$	$-1/\sqrt{42}$
010100	$3/\sqrt{42}$	$-5/\sqrt{42}$	110100	$-3/\sqrt{42}$	$-5/\sqrt{42}$
010101	$3/\sqrt{42}$	$-7/\sqrt{42}$	110101	$-3/\sqrt{42}$	$-7/\sqrt{42}$
010110	$1/\sqrt{42}$	$-5/\sqrt{42}$	110110	$-1/\sqrt{42}$	$-5/\sqrt{42}$
010111	$1/\sqrt{42}$	$-7/\sqrt{42}$	110111	$-1/\sqrt{42}$	$-7/\sqrt{42}$
011000	$5/\sqrt{42}$	$-3/\sqrt{42}$	111000	$-5/\sqrt{42}$	$-3/\sqrt{42}$
011001	$5/\sqrt{42}$	$-1/\sqrt{42}$	111001	$-5/\sqrt{42}$	$-1/\sqrt{42}$
011010	$7/\sqrt{42}$	$-3/\sqrt{42}$	111010	$-7/\sqrt{42}$	$-3/\sqrt{42}$
011011	$7/\sqrt{42}$	$-1/\sqrt{42}$	111011	$-7/\sqrt{42}$	$-1/\sqrt{42}$
011100	$5/\sqrt{42}$	$-5/\sqrt{42}$	111100	$-5/\sqrt{42}$	$-5/\sqrt{42}$
011101	$5/\sqrt{42}$	$-7/\sqrt{42}$	111101	$-5/\sqrt{42}$	$-7/\sqrt{42}$
011110	$7/\sqrt{42}$	$-5/\sqrt{42}$	111110	$-7/\sqrt{42}$	$-5/\sqrt{42}$
011111	$7/\sqrt{42}$	$-7/\sqrt{42}$	111111	$-7/\sqrt{42}$	$-7/\sqrt{42}$

The general memory effects' mitigation procedure is illustrated in Figure 7-4.  $K$  symbols of  $M$ -range are generated for the chosen modulation type and mapped to  $M$ -QAM in both frequency bands. Obtained complex symbols are transformed into the frequency domain using Fast Fourier Transform (FFT). Baseband power calculation is used to determine modulation point in order to find related complex coefficients for that modulation point. After multiplying by  $1/H_1(f, Pin)$  and  $1/H_2(f, Pin)$  for each band respectively, the symbols are subjected to inverse FFT (IFFT). Obtained complex signals are further divided into  $I_1, Q_1$  and  $I_2, Q_2$  components, which are used in the

nonlinearity compensation part of the predistorter. In general case, the mathematical operations required for the proposed method include two  $K$ -points FFT and two  $K$ -points IFFT procedures, and multiplying the frequency points by related complex-valued coefficients in both frequency. Specifically, in case of using orthogonal frequency division multiplex (OFDM) signal, the memory mitigation part of proposed predistorter does not need FFT and IFFT procedures. This is because the IFFT block is a part of OFDM creation, and therefore, the proposed complex multiplication by  $1/H(f, P_{in})$  can be easily incorporated in OFDM creation. As can be seen from Figure 7-6, the proposed procedure is realised as parallel multiplications before OFDM IFFT.

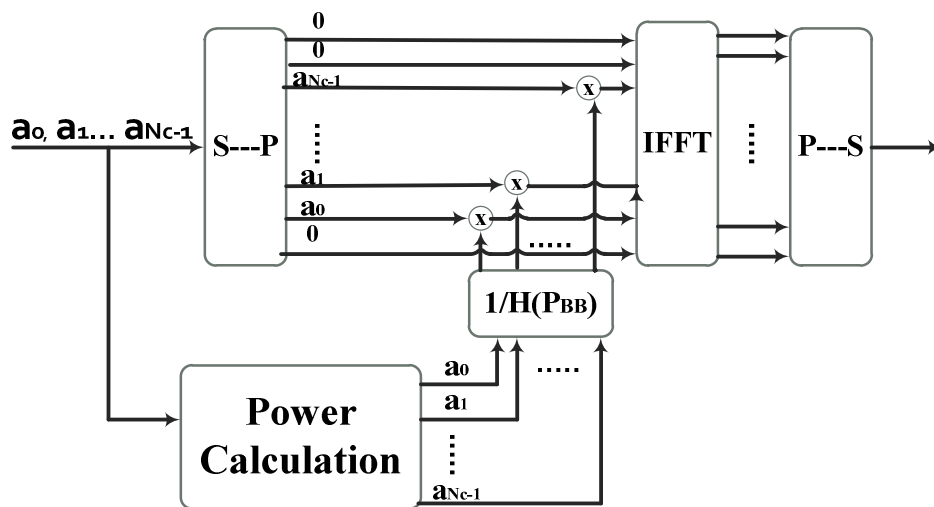


**Figure 7-6:** Proposed memory mitigation in case of OFDM signal

## 7.5. Experimental Setup

The experimental setup is shown in Figure 7-7. It is consisted of two signal generators, ESG E4433B and MXG N5182A, used to emulate concurrent dual-band transmitter. The long term evolution (LTE) signals with various bandwidth (1.4 MHz, 3 MHz and 5 MHz) and 5-MHz wideband code division multiple access (WCDMA) signal were created in Matlab and downloaded to MXG by using Agilent Signal Studio Toolkit and to ESG by using Advanced Design System (ADS). The combiner was utilised to combine the signals on different frequencies ( $f_1 = 880 \text{ MHz}, f_2 = 2.14 \text{ GHz}$ ). The combined signals were passed through the Device Under Test (DUT), which consists of the two-stages driver and CFH 2162-P3 PA (14 dB gain, P1dB +37 dBm) that was driven in a hard compression region. The PA output signals were down-converted with

Vector Signal Analyser (VSA) and captured on PC by 89600 VSA software in two steps, one for each band separately. These signals were then time-aligned with corresponding input signals.

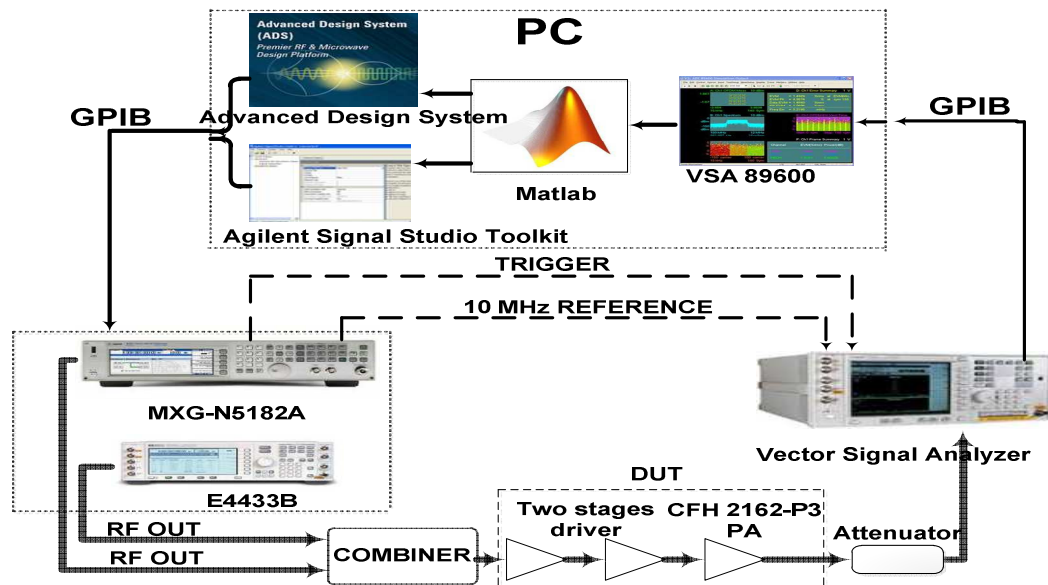


**Figure 7-7:** Measurement setup of concurrent dual-band transmitter (CFH 2162-P3 PA was used as DUT)

## 7.6. PA Characterisation

The polynomial models (7.1) and (7.2) of considered DUT were obtained for both frequency bands using dual-band CW measurement procedure presented in Chapter 6. To show difference in nonlinear characteristic of high power PA, the procedure is applied in both, single and concurrent dual-band transmitter mode. The seventh-order polynomials were used in order to decrease MSE below -40 dB. The measured and modelled transfer characteristics in single band and concurrent dual-band modes are compared in Figure 7-8. As can be seen, when the PA operates in dual-band mode, the P1dB compression point is notably decreased. In other words, PA nonlinear behaviour is significantly stronger in dual-band mode. Therefore, the theory related to dual-band nonlinear PA characterisation was verified here using high power PA as a DUT. To reiterate conclusion from the previous Chapter, PA must be characterised in dual-band mode. Otherwise, using of standard CW characterisation for both bands separately will seriously deteriorate the performances of the proposed DPD. The

obtained polynomial coefficients of CFH 2162-P3 PA extracted in transmitter dual-band mode were then used for calculating of coefficients of injected IMs and CMs.

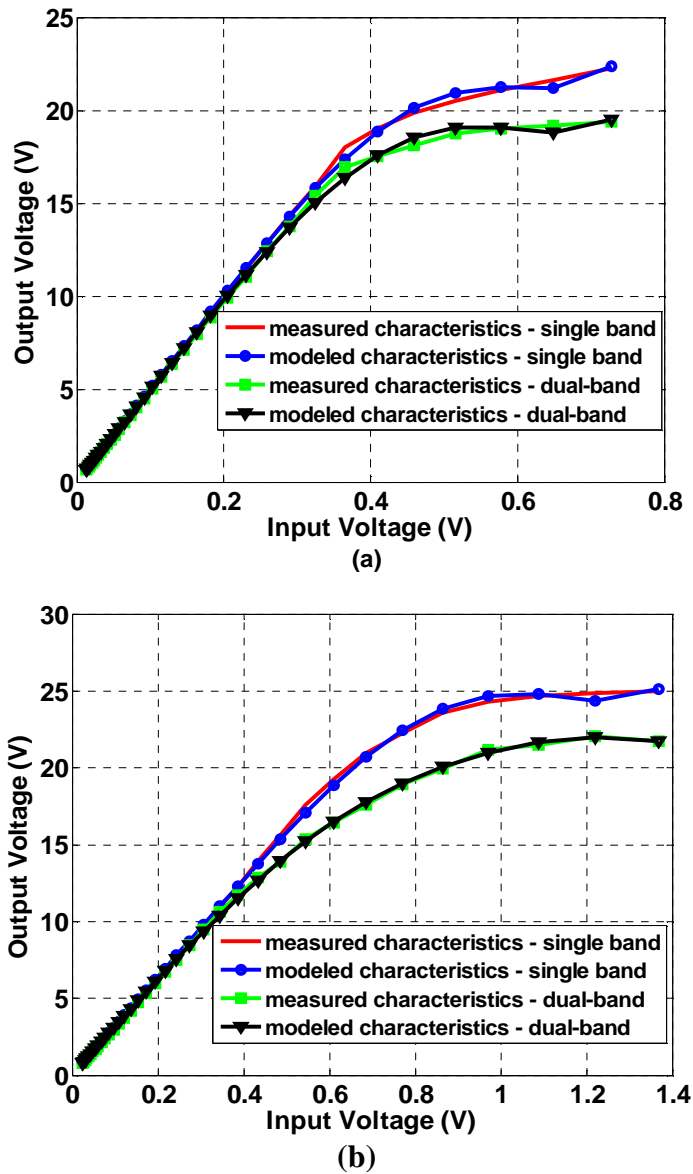


**Figure 7-8:** Comparisons of measured and modelled PA transfer characteristics in single and dual-band transmitter mode: (a) operating frequency 880 MHz (b) operating frequency 2.14 GHz

## 7.7. Concurrent Two-tone Test

To evaluate memory effects in concurrent dual-band transmitter, a concurrent two-tone test is used [7.5]. In this test, the amplitudes of left and right IM3, far CM3

and near CM3 are measured. The frequencies of these components are shown in Table 7-6.

**TABLE 7-6:** The frequencies of intermodulation and cross-modulation products

Modulation Products	Intermodulation	Far Cross-modulation	Near Cross-modulation
Lower Band	$2\omega_{L1} - \omega_{L2}$	$\omega_{L1} - \Delta\omega_U$	$\omega_{L2} - \Delta\omega_U$
	$2\omega_{L2} - \omega_{L1}$	$\omega_{L2} + \Delta\omega_U$	$\omega_{L1} + \Delta\omega_U$
Upper Band	$2\omega_{U1} - \omega_{U2}$	$\omega_{U1} - \Delta\omega_L$	$\omega_{U2} - \Delta\omega_L$
	$2\omega_{U2} - \omega_{U1}$	$\omega_{U2} + \Delta\omega_L$	$\omega_{U1} + \Delta\omega_L$

Memory effects metric was defined as an imbalance between right and left distortion products [7.5]. The tones were swept in one band, and imbalances were measured in both bands. The results shown in Figure 7-9 and Figure 7-10, prove the presence of memory effects.

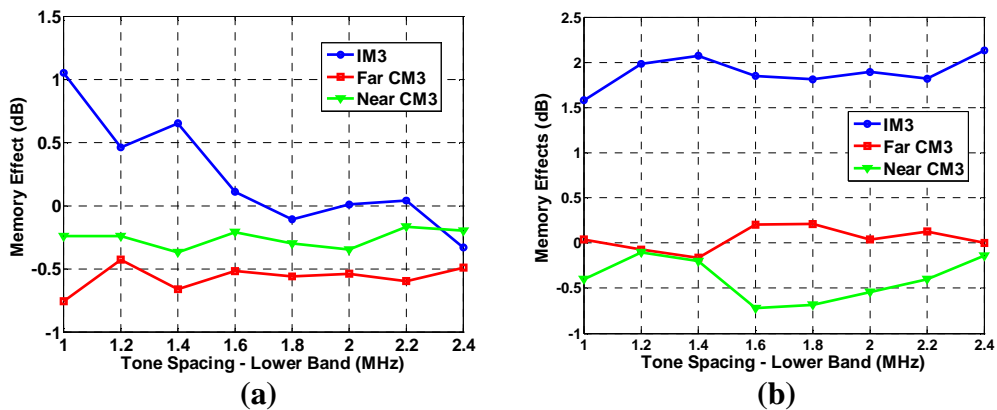


**Figure 7-9:** Memory effects as sweep frequency spacing in lower band (a) lower band, (b) upper band

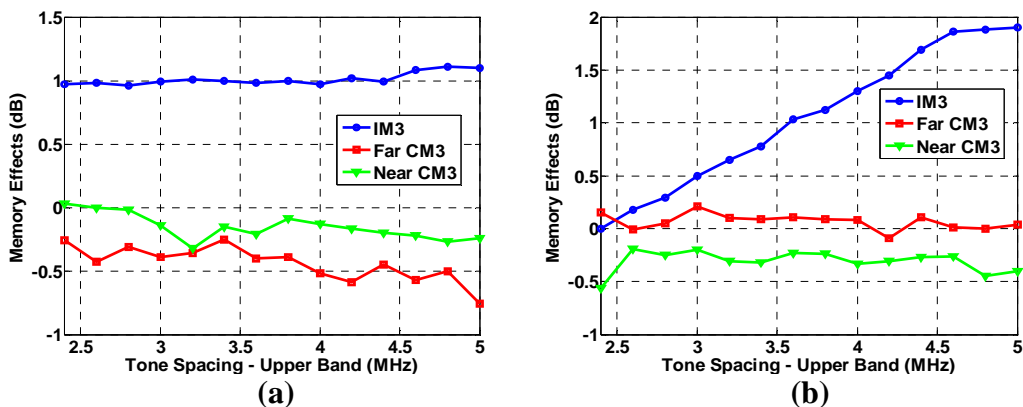


**Figure 7-10:** Memory effects as sweep frequency spacing in upper band (a) lower band, (b) upper band

## 7.8. Experimental Extraction of Memory Mitigation Coefficients

To compensate for PA memory effects,  $1/H_1(f, P_{in})$  and  $1/H_2(f, P_{in})$  need to be extracted. In order to calculate these coefficients, magnitude and phase of  $S_{21}^{(1)}$  and  $S_{21}^{(2)}$  were measured using a vector network analyser (VNA) measurement for different power levels. These levels were determined for each baseband modulation point using (7.15). The normalised frequency responses' magnitude and phase for three power levels in both operating bands are shown in Figure 7-11 and Figure 7-12.

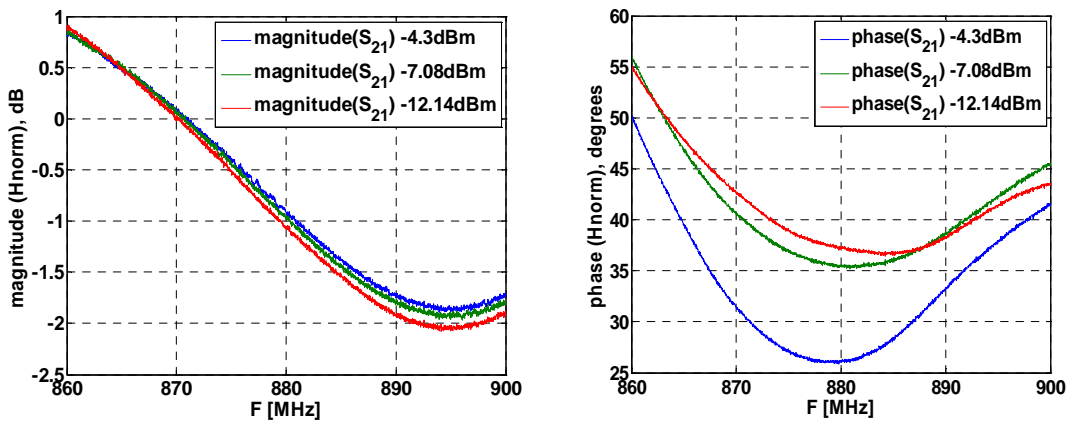


**Figure 7-11:** Magnitude and phase of the normalised frequency response for three power levels (lower band)

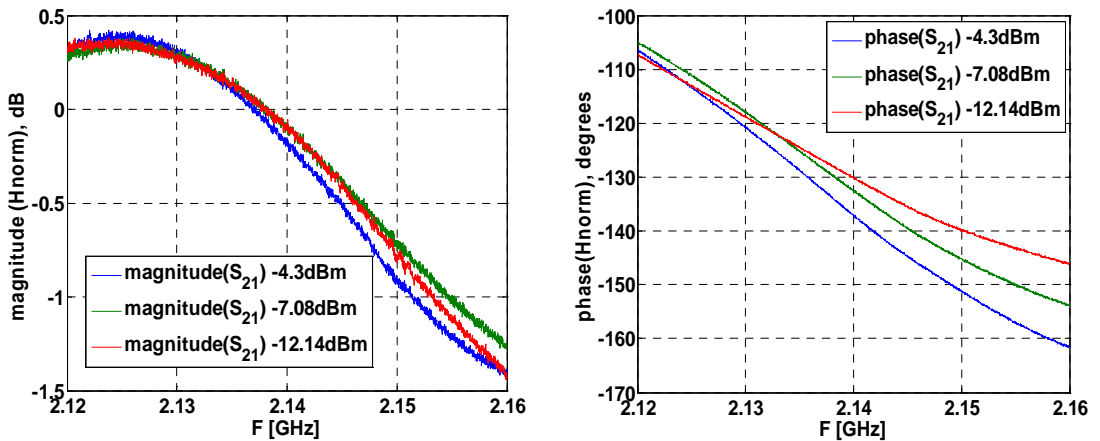


**Figure 7-12:** Magnitude and Phase of the normalised frequency response for three power levels (upper band)

## 7.9. Experimental DPD Results

The described DPD approach has been implemented in Matlab and tested in three different scenarios. The predistorted I and Q components for each signal sets were downloaded to ESG and MXG signal generators. In order to show the effectiveness of the proposed simultaneous injection approach, the existing injection-based DPDs [7.6], [7.7] were also considered. These techniques have not been tested in their original forms due to impractical sampling rate requirements for the DACs. In other words, their sampling rates depend on frequency separation in concurrent dual-band transmitter. However, for the testing purpose in this type of transmitter, the approaches [7.6], [7.7] were modified in such a way that they were applied in each band separately.

The PA output spectra in three different scenarios are shown in Figure 7-13. As can be seen, the distortion level is significantly higher in concurrent case (both generators ON) in comparison with conventional single-band (one generator OFF). The CM distortion components do not allow using modified [7.6] and [7.7], which inject IM distortion components in concurrent dual-band transmitter. In case of LTE at 880 MHz, these approaches have substantially degraded performances at transmitter output. In contrast, the proposed approach can successfully model and reduce the distortion in concurrent dual-band transmitter in every considered scenario.

One can see that performance of initial injection is improved in second iteration. This performance degradation of initial injection is result of distortion compensation limit in concurrent dual-band transmitter. It can be observed from experimental results that additional iteration improves spectrum regrowth 3-5 dB depending on scenario. The calculated EVM for different scenarios is shown in Table 7-7. If memory mitigation technique is incorporated before injection, an additional improvement of about 4 dB in spectrum regrowth and 5 dB in EVM can be observed in most demanding scenario III. An overall EVM improvement of more than 20 dB and spectrum regrowth improvements of more than 10 dB in case of LTE and about 20 dB in case of WCDMA were achieved when proposed approach is fully implemented. Moreover, an adjacent channel leakage ratio (ACLR) is also measured at 5 and 10 MHz frequency offsets in the most demanding scenario III. The 8- and 4-dBc improvements were achieved for LTE at band 1 whereas 9- and 4-dBc improvements were achieved for WCDMA at band 2.

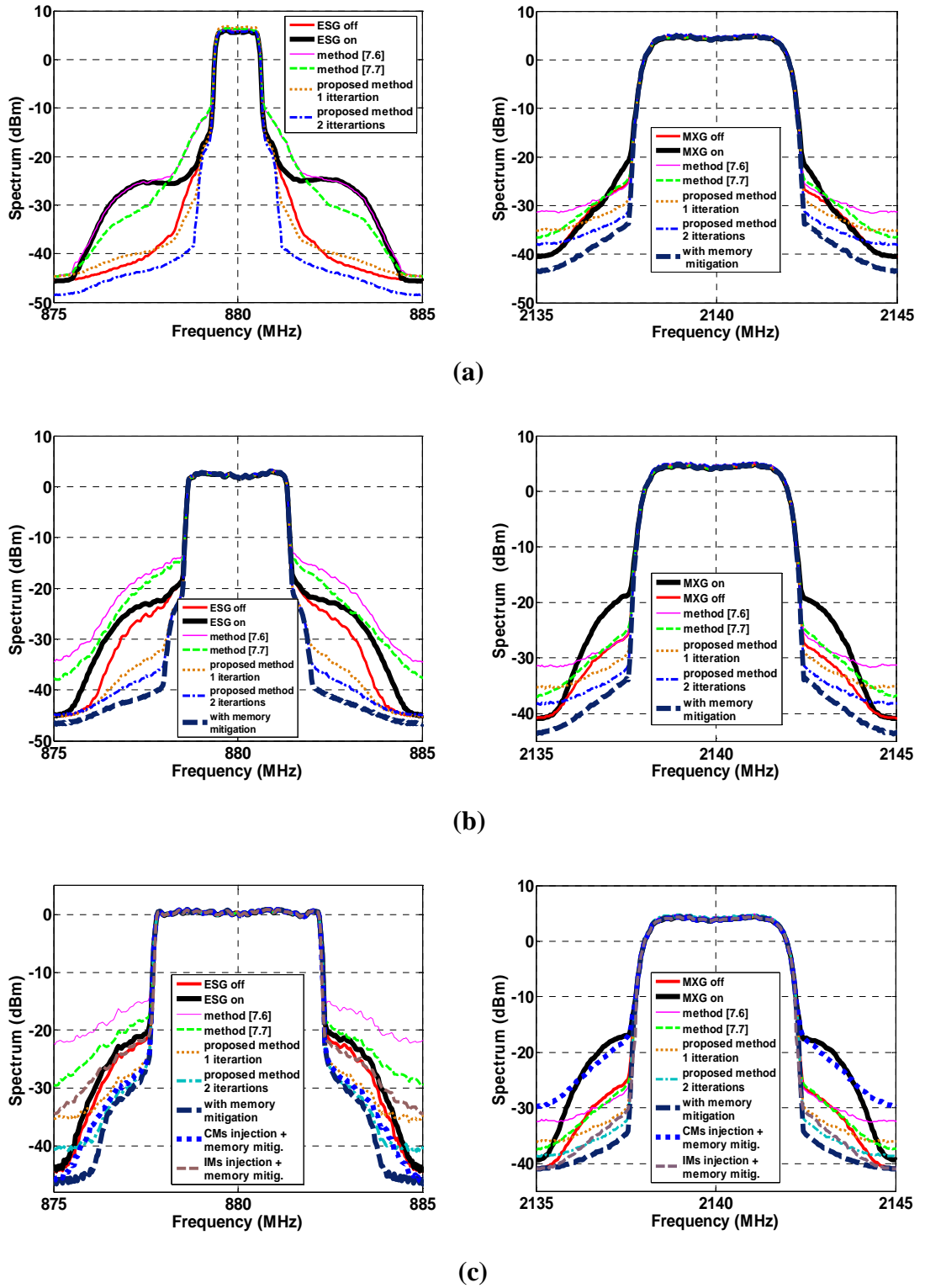


**Figure 7-13:** The PSD responses of concurrent dual-band transmitter (a) Scenario I, LTE 1.4 MHz – lower band, WCDMA – upper band (b) Scenario II, LTE 3 MHz – lower band, WCDMA – upper band (c) Scenario III, LTE 5 MHz – lower band, WCDMA – upper band

The spectrum regrowth and EVM improvements in scenario III have also been tested where either an injection of IMs (IM DPD) or an injection of CMs (CM DPD) was applied together with a memory mitigation procedure. As can be seen in Figure 7-13(c), the different results can be observed at band 1 and at band 2. One can see from the PSD responses that the PA output power at band 2 is higher than the power at band 1. Therefore, the CMs are dominant at band 1 whereas the IMs are dominant at band 2. Due to these facts, the IM DPD notably reduces distortion at band 2 whereas the CM DPD notably reduces distortion at band 1. This is in agreement with the baseband simulation analysis from Section 7-3. The IM DPD and CM DPD can be useful in some cases where a very low DPD computational complexity is required. The detailed investigation related to this will be a part of the author's future work.

**TABLE 7-7: EVM Results**

	Signal	Without Linearisation		With Linearisation	
		single band mode	dual-band mode	without memory mitigation	with memory mitigation
Scenario I	LTE 1.4 MHz	-21.27 dB	-19.49 dB	-40.76 dB	-40.91 dB
	WCDMA	-31.23 dB	-19.44 dB	-37.88 dB	-40.78 dB
Scenario II	LTE 3 MHz	-21.13 dB	-19.23 dB	-37.97 dB	-40.46 dB
	WCDMA	-31.23 dB	-19.09 dB	-37.12 dB	-40.36 dB
Scenario III	LTE 5 MHz	-20.72 dB	-17.75 dB	-33.28 dB	-38.41 dB
	WCDMA	-31.23 dB	-18.66 dB	-36.26 dB	-39.72 dB

## 7.10. Extension of the Proposed DPD for Multi-band Wireless Transmitters

The extension of the fundamental frequency model for the concurrent dual-band transmitter for modelling of the transmitters with more than two concurrent bands is also possible. In the case of tri-band transmitters and third-order PA nonlinearity, there

will be four undesired products in each band: one in-band IM product, two CM products which are the results of signal interactions with other signals separately and one CM product which depends on all three signals as a result of interaction between them. Deductively, in case of quad-band transmitters, there will be  $IM_3^{(1)}$ ,  $CM_{31}^{(12)}$ ,  $CM_{31}^{(13)}$ ,  $CM_{31}^{(14)}$ ,  $CM_{31}^{(123)}$ ,  $CM_{31}^{(124)}$ ,  $CM_{31}^{(134)}$  and  $CM_{31}^{(1234)}$  in the first band. In addition to the in-band IM, for the general  $N$ -band fundamental frequency model, there will be  $\binom{N-1}{1} + \binom{N-1}{2} + \dots + \binom{N-1}{N-1}$  CM undesired products. However, it can be expected that the  $\binom{N-1}{1}$  CMs which are the results of the signal  $N - 1$  interactions with  $N - 1$  other signals will have a dominant impact together with the in-band IM. This is just a brief introduction of the potential extended methodology and the detailed theoretical derivation and verification will be a part of the future work.

## 7.11. Discussion

It was proved by experiments that the concurrent dual-band DPDs [7.8]-[7.17] can successfully model and reduce the distortion in concurrent dual-band transmitters. However, the key features of the proposed approach in comparison with state-of-the-art DPDs for concurrent dual-band transmitters have been highlighted in this Section. This comparative analysis has been summarised in Table 7-8.

**TABLE 7-8:** Comparisons of this work with recent works on concurrent dual-band wireless transmitters

Method	DPD run-time complexity	DPD identification complexity	Dependency on freq. offset	System bandwidth constraints	Adaptive closed-loop	Extension for multi-band
Volterra-based [7.8]-[7.14]	High	High + numerical instability	No	High, can be reduced [7.10], [7.18]	Yes	Very Complex
LUT-based [7.15]	High	High + numerical instability	No	High, can be reduced [7.10], [7.18]	Yes	Very Complex
ANN-based [7.16]	High	Very High	No	High, can be reduced [7.10]	Yes	Very Complex
Freq.-selective DPD [7.17]	High	Moderate	Yes	Moderate	No	Impractical
This Work	Low	Moderate	No	High, can be reduced	No	Moderate

The main advantage of the proposed DPD is low complexity of predistorter. To explain, an overall complexity of DPD is a sum of DPD run-time complexity in transmitter's feedforward path and complexity of DPD estimation performed online or offline. One should keep in mind that DPD estimation of the parameters is occasional and thus, is not a continuous load on the processing unit. Therefore, from the overall transmitter operation point of view, the computations carried out by the feedforward DPD block itself are much more important. In other words, the operations needed per sample are the main source of complexity. The number of floating point operations (FLOPs) is parameter for the DSP computational complexity estimation of DPD. Table 7-9 shows operation-FLOPs conversion for every particular operation performed into DSP [7.18].

**TABLE 7-9:** Number of FLOPs for different operations performed into DSP

Operation	Number of FLOPs
Conjugate	0
Delay	0
Real addition	1
Real multiplication	1
Complex addition	2
Complex-real multiplication	2
$ \cdot ^2$	3
Complex-complex multiplication	6
Square root	7

The proposed 2D-DPD predistorter has significantly lower DSP run-time computational complexity in comparison with existing 2D-DPD predistorters for concurrent dual-band transmitters mainly because the proposed simultaneous injection uses real additions and real multiplications only. To demonstrate the effectiveness of the proposed method in terms of DSP run-time computational complexity, the number of operations and FLOPs number needed for the proposed method and most widely used 2-D DPD based on complex polynomials are calculated. In memoryless case, for the  $N^{\text{th}}$ -order nonlinearity, these methods need the following numbers of operations:

- complex polynomials 2-D DPD:  $N(N + 1)$  complex multiplications;  $N(N + 1) - 2$  complex additions;  $N(N + 1) - 2$  complex-real multiplications;  $N(N + 1) - 6$  real multiplications; 2 square modulus; 2 square roots;
- proposed approach:  $2\lceil N/2 \rceil(\lceil N/2 \rceil + 1) - 4$  real additions;  $4\lceil N/2 \rceil(\lceil N/2 \rceil + 1) - 12$  real multiplications; 2 square modulus.

Using Table 7-9 and these calculated numbers of operations, the number of FLOPs needed for these approaches can be easily calculated. The proposed approach needs  $6\lceil N/2 \rceil(\lceil N/2 \rceil + 1) - 10$  FLOPs whereas the 2-D DPD approach based on complex polynomials needs  $11N(N + 1) + 6$  FLOPs. Therefore, the proposed approach has considerably lower run-time complexity because it requires about 4 times less FLOPs. The same conclusion will be derived after comparison of the proposed approach with other state-of-the-art approaches in terms of run-time complexity. This is mainly because the other approaches have comparable or higher complexity when compared with 2-D DPD complex polynomials [7.11]-[7.16]. Moreover, in memory case, the proposed approach is even less complex than 2-D DPD memory polynomials. To clarify, the number of FLOPs is increased  $M$  times in case of 2-D DPD memory polynomials, where  $M$  is memory depth. In contrast, it should be noticed that memory mitigation part of the proposed method uses complex multiplications, but  $K$  parallel multiplications for  $K$  symbols. In other words, the proposed approach uses only one complex multiplication per sample. Moreover, the additional FFT and IFFT procedures can be omitted in case of OFDM signals.

The approaches [7.8]-[7.16] identify predistortion functions in an adaptive closed-loop online, but suffer from a potential numerical instability of the identification process as demonstrated in [7.19]-[7.21]. The application of the digital predistorter [7.17] is impractical when considering the wide bandwidth of the dual-band signal (the sum of bandwidths of both signals and frequency offset between bands), but this methodology is frequency selective and can be useful for wide-bandwidth signals that do not have large frequency separation. This method also needs offline large-signal-network-analyser (LSNA) measurements, but has a simpler transmitter hardware architecture in comparison with the others. The proposed predistorter is also implemented in open-loop and needs dual-band CW and VNA offline measurements. The presented baseband simultaneous IM and CM injection methodology is much more suitable for extension and application in transmitters with more than two concurrent

bands. The main reason is the fact that the complexity of the extensions of state-of-the-art approaches will be dramatically increased and their application in multi-band transmitters will be impractical. In order to reduce high bandwidth constraints, the band-limited DPD is desirable [7.22]. The proposed approach discriminates an impact of IMs and CMs, and its extension in this direction will probably be simpler than the extensions of state-of-the-art dual-band DPDs. Also, using multi-tone or realistic digitally modulated signals for the dual-band PA characterisation process will increase model accuracy and improve distortion reduction especially in the case of ultra-wideband signals.

## 7.12. Conclusion

A new 2-D linearity enhancement architecture based on simultaneous injection of the in-band IM and CM distortion components together with memory mitigation was presented and verified through experiments. A nonlinear fundamental frequency model was derived for concurrent dual-band transmitter for the first time. It was proved that proposed simultaneous injection of in-band IM and CM distortion products can improve the signals' performances in concurrent dual-band transmitters. Additionally, it was demonstrated that the proposed iterative approach can successfully deal with distortion compensation limit. The proposed technique successfully minimises memory effects, does not depend on frequency separation between bands and has low computational complexity in comparison with previously proposed DPDs for concurrent dual-band transmitters. To the best knowledge of the author, this is the first 2-D injection-based linearisation architecture. It was clearly shown that the technique outperforms conventional injection-based DPDs in terms of EVM and PSD performances when they were tested in emulated concurrent dual-band transmitter. According to the obtained results, the method can be a serious candidate for distortion compensation in modern concurrent dual-band wireless transmitters' applications. Table 7-8 compares the performance of the proposed 2D-DPD with recently reported 2D-DPDs for concurrent dual-band transmitters. Furthermore, the author feels that the presented theory can be very useful for researchers and engineers who design PAs for developing of RF lineariser incorporated in dual-band PA design to achieve high linearity and efficiency of PA.

## 7.13. References

- [7.1] **M. Cabarkapa**, N. Neskovic, and D. Budimir, "A Generalized 2-D Linearity Enhancement Architecture for Concurrent Dual-Band Wireless Transmitters", *IEEE Transactions on Microwave Theory and Techniques*, vol. 61, no.12, pp. 4579-4590. Dec. 2013.
- [7.2] N. Mizusawa, and S. Kusunoki, "Third- and fifth-order baseband component injection for linearization of the power amplifier in a cellular phone," *IEEE Trans. Microw. Theory Tech.*, vol. 53, no. 4, pp. 3327-3334, April 2005.
- [7.3] D. Bondar, and D. Budimir, "A new digital predistortion for linearity improvement and suppression of memory effects", in *Proc. 39th European Microwave Conf.*, pp. 1437-1440, Sept. 2009.
- [7.4] 3GPP TS 36.211 version 8.7.0 Release 8 and ETSI TS 136 211 V8.7.0 (2009-06) Technical Specifications. Available Online:  
[http://www.etsi.org/deliver/etsi\\_ts/136200\\_136299/136211/08.07.00\\_60/ts\\_136211v080700p.pdf](http://www.etsi.org/deliver/etsi_ts/136200_136299/136211/08.07.00_60/ts_136211v080700p.pdf)
- [7.5] W. Chen, S.A Bassam, M. Helaoui, F.M. Ghannouchi, Z. Feng, "Characterization of memory effects in concurrent dual-band PAs," in *Proc. Asia-Pacific Microw. Conf. (APMC)*, pp.1646-1649, 5-8 Dec. 2011.
- [7.6] D. Bondar, and D. Budimir, "A digital predistorter for wireless transmitters", *Int. J. of RF and Microw. Comput.-Aided Eng.*, vol. 19, no 4, pp. 453-459, April 2009.
- [7.7] **M. Cabarkapa**, N. Neskovic, A. Neskovic, and D. Budimir, "Adaptive nonlinearity compensation technique for 4G wireless transmitters," *Electron. Lett.*, vol.48, no.20, pp.1308-1309, Sept. 2012.
- [7.8] S.A. Bassam, M. Helaoui, and F.M. Ghannouchi, "2-D digital predistortion (2-D-DPD) architecture for concurrent dual-band transmitters," *IEEE Trans. Microw. Theory Tech.*, vol.59, no.10, pp.2547-2553, Oct. 2011.

- [7.9] S.A. Bassam, W. Chen; M. Helaoui, F.M. Ghannouchi , and Z. Feng, "Linearization of concurrent dual-band power amplifier based on 2D-DPD technique," *IEEE Microw. Wireless Comp. Lett.*, vol.21, no.12, pp.685-687, Dec. 2011.
- [7.10] S. A. Bassam, A. Kwan, W. Chen, M. Helaoui, and F. M. Ghannouchi, "Subsampling feedback loop applicable to concurrent dual-band linearization architecture," *IEEE Trans. Microw. Theory Tech.*, vol. 60, no. 6, pp. 1990–1999, Jun. 2012.
- [7.11] Y.-J. Liu, J. Zhou, W. Chen, B. Zhou, and F.M. Ghannouchi, "Low-complexity 2D behavioural model for concurrent dual-band power amplifiers," *Electron. Lett.*, vol.48, no.11, pp.620-621, May 2012.
- [7.12] Y.-Jiang Liu, W. Chen, J. Zhou, B.-Hua Zhou, and F. Ghannouchi, "Digital predistortion for concurrent dual-band transmitters using 2-D modified memory polynomials," *IEEE Trans. Microw. Theory Tech.*, vol.61, no.1, pp.281-290, Jan. 2013.
- [7.13] Y.-J. Liu, W. Chen, B. Zhou, J. Zhou, and F.M. Ghannouchi, "2D augmented Hammerstein model for concurrent dual-band power amplifiers," *Electron. Lett.* , vol.48, no.19, pp.1214-1216, Sept. 2012.
- [7.14] J. Moon, P. Saad, J. Son, C. Fager, and B. Kim "2-D enhanced Hammerstein behavior model for concurrent dual-band power amplifiers", in *Proc. 42th Eur. Microw. Conf.*, pp. 1249-1252, Oct. 2012.
- [7.15] L. Ding, Z. G. Yang, and H. Gandhi, "Concurrent dual-band digital predistortion", in *IEEE MTT-S Int. Microw. Symp. Dig.*, pp.1-3, June 2012.
- [7.16] Z. Huang, W. Chen, Z. Feng, and F.M. Ghannouchi, "Forward behavioral modeling of concurrent dual-band power amplifiers using extended real valued time delay neural networks," in *Int. Microw. Millim. Wave Tech. (ICMMT) Conf.*, pp.1-4, May 2012.

- [7.17] J. Kim, P. Roblin, D. Chaillot, and Z. Xie, "A generalized architecture for the frequency-selective digital predistortion linearization technique," *IEEE Trans. Microw. Theory Tech.*, vol.61, no.1, pp.596-605, Jan. 2013.
- [7.18] A.S. Tehrani, C. Haiying, S. Afsardoost, T. Eriksson, M. Isaksson and C. Fager, "A comparative analysis of the complexity/accuracy tradeoff in power amplifier behavioral models," *IEEE Trans. Microw. Theory Tech.*, vol. 58, no. 6, pp. 1510-1520, June 2010.
- [7.19] R. Raich, H. Qian, and G. T. Zhou, "Orthogonal polynomials for power amplifier modeling and predistorter design," *IEEE Trans. Veh. Technol.*, vol. 53, pp. 1468–1479, Sep. 2004.
- [7.20] C. Quindroit, N. Naraharisetti, P. Roblin, S. Gheitanchi, V. Mauer, and M. Fitton, "Concurrent dual-band digital predistortion for power amplifier based on orthogonal polynomials," in *IEEE MTT-S Int. Microw. Symp. Dig.*, Seattle, WA, USA, Jun. 2013.
- [7.21] C. Quindroit, N. Naraharisetti, P. Roblin, S.Gheitanchi, V. Mauer, and M. Fitton, "FPGA Implementation of Orthogonal 2D Digital Predistortion System for Concurrent Dual-Band Power Amplifiers Based on Time-Division Multiplexing," *IEEE Trans. Microw. Theory Tech.*, vol.61, no.12, pp. 4591-4599, Dec. 2013.
- [7.22] C. Yu, L. Guan, E. Zhu, and A. Zhu, "Band-limited volterra series based predistortion for wideband RF power amplifiers," *IEEE Trans. Microw. Theory Tech.*, vol. 60, no. 12, pp. 4198–4208, Dec. 2012.

## 8. CONCLUSION

This Chapter presents overall conclusions related to the performed research work, including the thesis summary, original contributions to knowledge and suggestions for the future work.

### 8.1. Thesis Summary

In recent years, the design of linear and efficient transmitters for base stations and terminals has become one of the major tasks for researchers and engineers. A great concern has been expressed so far with regard to enhancing the PA performances due to the fact that the most challenging part of a transmitter is the power amplifier. A common approach for achieving both the high linearity and efficiency is to design a PA operating in a nonlinear efficient mode and to provide its linearisation by an external DSP device.

In this thesis, a comprehensive research work on the topic of linearisation of power amplifiers in modern wireless transmitters such as 4G SISO and dual-band transmitters has been presented. The advanced digital predistortion linearisation techniques for these transmitters have been developed during this research work. The theoretical concept, practical implementation and validation of the proposed techniques by simulations and experiments have been outlined in the thesis.

The research work included the following areas. Initially, the PA system parameters, a signal quality metrics, the PA behavioural modelling metrics, OFDM as a basis of 4G wireless communications and the main parameters of 4G LTE standard were described. Also, the distortion problem in multi-branch and multi-frequency MIMO transmitters was discussed. A comparative overview of the existing digital predistortion techniques in different types of transmitters was accomplished, accompanied by a brief summary of their advantages and shortcomings. Since digital predistortion is one of the most cost-effective, easily integrated and flexible linearisation methods, it was selected as a basis for the development of the proposed technique. One of the major tasks of this work was to reduce high complexity of existing digital predistorters. Consequently, injection-based linearisation techniques

have been investigated and their advantages and disadvantages were described. These techniques have been chosen as a basis for developing of advanced injection-based digital predistortion techniques. In this thesis, the adaptive nonlinearity compensation technique for 4G wireless transmitters was proposed and verified experimentally using developed test bed for adaptive DPD. This is the first time that one injection-based technique is experimentally verified using high PAPR signal such as real LTE signal. On top of that, this is the first adaptive, injection-based DPD. Furthermore, for the first time, the injection-based theory is expanded to be applicable in concurrent dual-band transmitters with different PAs. To the best knowledge of the author, the proposed DPD is the first injection-based DPD for concurrent dual-band transmitter. It has been clearly shown that the technique outperforms conventional injection-based techniques in terms of EVM and PSD performances when they were tested in emulated concurrent dual-band transmitter. During this work, the proposed theory is further expanded and generalised DPD for concurrent dual-band transmitters was developed. A general fundamental frequency model for concurrent dual-band transmitter was derived. The generalised DPD based on this theory was proposed. This DPD was experimentally attested using highly nonlinear PA that exhibits memory effects. In addition to this, the reduction of distortion compensation limit phenomena in concurrent dual-band transmitter was considered theoretically and verified in experiments.

Chapter 2 has covered the PA system parameters, nonlinear behavioural modelling metrics and PA memory effects. The main signal quality metrics in time and frequency domain have been defined, while OFDM technology, as a basis of recent and future wireless communications systems, has been explained. Some of the important features of 4G LTE were given in this Chapter. Also, the other problems that cause distortion such as crosstalk specific to multi-branch MIMO transmitters as well as cross-modulation specific to multi-frequency MIMO transmitters were discussed.

Chapter 3 has presented a comparative overview of existing, behavioural model based DPD linearisation techniques including LUT-based DPD, Volterra-based DPD, memory polynomial DPD and DPD based on artificial neural networks (ANN). The theoretical concept, main advantages and drawbacks of these DPDs were discussed. The adaptive DPD architectures such as direct learning architecture (DLA) and indirect learning architecture (ILA) were depicted in the Chapter. The DPD approaches for

multi-branch and multi-frequency MIMO transmitters were depicted also. Recent developments and existing problems in the area of DPD linearisation were discussed.

The injection-based linearisation concept has been described in Chapter 4. This Chapter provides an overview of state-of-the-art linearisation techniques based on injection of distortion products either in RF or baseband. This Chapter focuses on digitally implemented baseband injection-based techniques, particularly on technique based on IM3 and IM5 injection as well as technique based on iterative injection approach. It was shown that these injection-based techniques have tolerable complexity and therefore, they were chosen as a basis of the original developments of the thesis explained in Chapter 5, 6 and 7.

In Chapter 5, the adaptive, low-complexity DPD for 4G SISO wireless transmitters is introduced. PA linearisation was demonstrated using this DPD based on iterative injections of the in-band distortion components. This method has three important advantages in comparison with existing solutions. First, the proposed DPD was verified experimentally using more than 10 dB peak-to-average power ratio (PAPR) 5-MHz downlink LTE signal. Secondly, it uses real multiplications and real additions only and avoids complex Volterra, LUT or polynomials for nonlinearity compensation. Third, in contrast with existing injection-based DPD, the technique uses adaptive architecture, and therefore, is adaptive to the variation of PA nonlinear transfer function in real environmental conditions. The nonlinear PA modelling extraction method based on AM/AM least-squares polynomial regression approximation was explained and used in experiments. The adaptive experimental test-bed was described. It was shown that the technique achieves about 10 dB improvements in spectrum regrowth and about 7 % in EVM.

Chapter 6 presents the first injection-based memoryless digital predistortion technique for concurrent dual-band transmitters. It is based on simultaneous injection of IM and CM distortion components. The theoretical concept of the proposed DPD technique and verification of its feasibility and linearisation performances by experiments were presented in this Chapter. The mathematical model of the proposed technique was derived for the fifth-order polynomial. The PA nonlinearity characterisation in single band and concurrent dual-band transmitter mode were

described and discussed. The linearisation of the low-power ZFL-500 PA was demonstrated in experimentally emulated concurrent dual-band transmitter using this new 2-D DPD.

In Chapter 7, the proposed technique, described in Chapter 6, has been further expanded and new advancements have been introduced. The technique has been further generalised to any degree of nonlinearity. Also, an initial injection approach presented in Chapter 6 was extended in Chapter 7 to generalised iterative injection approach, which was used to overcome distortion compensation limit phenomena in concurrent dual-band wireless transmitters caused by initial injection. In other words, this approach is based on simultaneous iterative injection of the in-band IM and CM products. Moreover, in comparison with memoryless ZFL-500 PA, it was shown in experiments that CFH 2162-P3 PA exhibits memory effects that degrade the performances of DPD at the output of concurrent dual-band transmitter. The CFH 2162-P3 PA nonlinear characterisation in single band and concurrent dual-band mode were presented. The presence of memory effects were detected by concurrent two-tone test which was also described in this Chapter. These memory effects have been minimised in frequency domain by utilising baseband symbol adjustable normalised inverse  $S_{21}$ -parameter parallel multiplication. This procedure has been carried out separately for both bands of concurrent dual-band transmitter. The experiments were conducted using different signal sets (LTE 1.4 MHz, LTE 3 MHz and LTE 5 MHz at 880 MHz and WCDMA at 2.14 GHz). On the whole, this Chapter has introduced the theoretical background and experimental verification of the complete DPD system for concurrent dual-band wireless transmitters. The numerous advantages of this DPD in comparisons with existing concurrent dual-band DPDs were discussed in detail.

## **8.2. ORIGINALITY and CONTRIBUTIONS to KNOWLEDGE**

The thesis focuses on novel solutions for distortion reduction of power amplifiers in modern wireless transmitters such as 4G SISO and concurrent dual-band transmitters. The adaptive injection-based DPD was developed and experimentally verified using 4G signal. In addition to this, the injection-based DPD theory was

extended for application in concurrent dual-band wireless transmitters. The proposed DPDs have adjustable nature and can be tuned to achieve the best ratio of linearisation degree to computational complexity for every particular wireless application. The proposed solutions reduce implementation costs and the overall complexity of the design of modern wireless transmitters without sacrificing performance of power amplifiers. The author believes that this research work will considerably contribute to the international academic research on digital predistortion of power amplifiers suitable for 4G and beyond wireless transmitters' applications. There are three main contributions, which resulted from the completed project:

- The proposed baseband adaptive DPD that has lower computational complexity in comparison with state-of-the-art adaptive DPDs. It was experimentally verified using 4G signal and ZFL-500 PA as a DUT.
- The proposed and experimentally verified memoryless 2-D DPD based on simultaneous injection of IM and CM distortion products. The technique does not depend on frequency separation between frequency bands in concurrent dual-band transmitter and has low complexity in comparison with existing solutions.
- This proposed theory on concurrent dual-band DPD has been further extended to be applicable in concurrent dual-band transmitter with highly nonlinear PAs that exhibit memory effects. A general fundamental frequency model for concurrent dual-band transmitter was developed theoretically and proved experimentally. An individual impact of each IM and CM distortion component was theoretically derived and analysed. It was clearly proved by experiments that the proposed predistorter improves the in-band and out-of-band performances of both signals. The proposed generalised 2-D DPD architecture based on derived fundamental frequency model does not depend on frequency separation between bands and has low complexity in comparison with concurrent dual-band DPD's state-of-the-art. In addition to this, it was clearly shown in experiments that when using iterative simultaneous injections of IM and CM distortion products, a phenomenon

known as distortion compensation limit can be reduced in concurrent dual-band wireless transmitters. The presence of memory effects and their mitigation in frequency domain for each band of concurrent dual-band transmitter were also demonstrated in experiments. Furthermore, the potential extension of the proposed DPD to be applicable in concurrent multi-band wireless transmitters will be much more suitable than the extension of the other 2-D DPD solutions.

### 8.3. Future Work

One of the directions for the future work would be the extension of current work on digital processing technique with baseband injection with the aim of improving linearity of real-life device under test (power amplifier) in multi-branch MIMO transmitters that have nonlinear crosstalk problem which degrade the quality of existing DPD solutions.

The proposed solutions would be further validated by involving the new high-power, high-efficiency types of power amplifiers (Doherty, class F, inverse class F or class J PAs that exhibit strong memory effects and PM/AM and PM/PM distortions) as DUTs into system and carrying out experimental tests of proposed algorithms in 4G SISO, dual-band and dual-input MIMO transmitters. Comparative analysis of DPD solutions for different types of transmitters and PAs in the same experimental conditions is another possible area of future work.

Another area of the suggested future work is to investigate the performances and limitations of the developed adaptive lineariser for different OFDM digitally modulated signals in different transmitter types using computer modelling, analysis and optimisation by ADS and Matlab as well as using of real, adaptive test-bed for experimental validation. Carrying out experimental tests of the created predistortion systems with OFDM signals that have different bandwidth will bring some new problems and a novel band-limited DPD will be needed. The extension of the proposed DPD in this direction is a potential area of the future work. The experimental testing would be done in different types of transmitters.

The variations in environmental conditions cause degradation of the lineariser performances. Consequently, the proposed predistorter's adaptive implementation for multi-band and multi-branch MIMO transmitters would be preferable. However, the receiver at feedback adaptation significantly increases the transmitter's complexity and there is a trade-off between transmitter complexity and signal quality at transmitter's output. This trade-off should be solved for every particular wireless transmitter's application.

The extension of the fundamental frequency model for the concurrent dual-band transmitter for modelling of the transmitters with more than two concurrent bands is also possible. The presented baseband simultaneous IM and CM injection methodology is much more suitable for the extension and application in transmitters with more than two concurrent bands. This is mainly because the fact that the proposed approach has significantly smaller run-time complexity in comparison with state-of-the-art approaches. In contrast, the extensions of the previously proposed concurrent dual-band DPDs for transmitters with more than two concurrent bands would be very complex and impractical. The baseband equivalent simulations would be very useful in these multi-band transmitters in order to find an individual impact of each distortion component. In this way, a significant complexity reduction of DPD would be achieved. Generally, the further complexity reduction of DPD in different kind of modern wireless transmitters would be a very interesting direction of the future work. Further experiments with IM DPD and CM DPD would be performed in experimentally emulated concurrent dual-band transmitter.

The simultaneous injections of IMs and CMs are excellent because the additional manual tuning of the DPD coefficients would be performed in order to suppress distortion as much as possible in any type of PAs. Therefore, the additional phase adjustment procedure of the proposed digital predistorter might be used in order to improve performances at transmitter output. It would be especially useful when using highly-efficient PA structures as DUTs.

Moreover, one of the directions for the future work would be developing and applying the extension of the proposed DPD for compensating real-life I/Q imperfections in different types of wireless transmitters. Upon achieving successful results, the injection-based methodology would be investigated for improving the linearity and jointly compensating real-life imperfections introduced by PA, modulator and other components.

Generally, the polynomial model can include both the AM/AM and AM/PM distortions if the coefficients are obtained in the complex form. It will be interesting to test injection methodology when using much more complex models. This will increase run-time complexity of the predistorter, but possibly have some advantages. For instance, the memory mitigation procedure and VNA measurement might be omitted in that case.

The developed theory on concurrent dual-band DPD would be very useful for researchers and engineers who design PAs for developing of RF lineariser incorporated in dual-band PA design to achieve high linearity and efficiency of PA. This would also be a very interesting direction for the future work.

Finally, a real-life implementation of the designed DPDs using FPGA would become a part of further studies. The real-life experiments with the FPGA design of the proposed predistorter would evaluate the overall performance of the system before mass production.

## LIST OF PUBLICATIONS

- [P1] **M. Cabarkapa**, N. Neskovic, and D. Budimir, "A Generalized 2-D Linearity Enhancement Architecture for Concurrent Dual-Band Wireless Transmitters", *IEEE Transactions on Microwave Theory and Techniques*, vol. 61, no.12, pp. 4579-4590. Dec. 2013.
- [P2] **M. Cabarkapa**, N. Neskovic, A. Neskovic, and D. Budimir, "Adaptive nonlinearity compensation technique for 4G wireless transmitters," *IET Electronics Letters*, vol.48, no.20, pp.1308-1309, Sept. 2012.
- [P3] **M. Cabarkapa**, N. Neskovic, and D. Budimir, "2-D Nonlinearity Compensation Technique for Concurrent Dual-Band Wireless Transmitters," *IEEE International Microwave Symposium 2013, Seattle, WC, USA*, pp. 1–3, June 2013.
- [P4] **M. Cabarkapa**, M. Bozic, N. Neskovic, A. Neskovic and D. Budimir, "Compensation of Undesired Effects in MIMO Wireless Transceivers", *IEEE International Symposium on Antennas and Propagation and CNC/USNC/URSI National Radio Science Meeting (APS2012)*, pp. 1-2, July 8-14, 2012, Chicago, Illinois, USA.

# APPENDIX

## Data Sheets for the Power Amplifiers

### Coaxial Amplifier

50Ω Low Power 0.05 to 500 MHz

ZFL-500+  
ZFL-500



SMA version shown  
CASE STYLE: Y460

#### Features

- wideband, 0.05 to 500 MHz
- rugged, shielded case
- low noise, 5.3 dB typ.
- protected by US Patent, 6,943,629

#### Applications

- instrumentation
- lab use
- VHF/UHF

Connectors	Model	Price	Qty.
SMA	ZFL-500(+)	\$69.95	(1-9)
BNC	ZFL-500-BNC	\$74.95	(1-9)
BRACKET (OPTION "B")		\$5.00	(1+)

**+RoHS Compliant**  
The +Suffix identifies RoHS Compliance. See our web site for RoHS Compliance methodologies and qualifications

#### Amplifier Electrical Specifications

MODEL NO.	FREQUENCY (MHz)		GAIN (dB)		MAXIMUM POWER (dBm)		DYNAMIC RANGE		VSWR (-1) Typ.		DC POWER	
	f <sub>L</sub>	f <sub>H</sub>	Min.	Flatness Max.	Output (1 dB Compr.)	Input (no damage)	NF (dB) Typ.	IP3 (dBm) Typ.	In	Out	Volt (V) Nom.	Current (mA) Max.
ZFL-500(+)	0.05	500	20	±1.0	+9	+5	5.3	+18	1.9	1.9	15	80

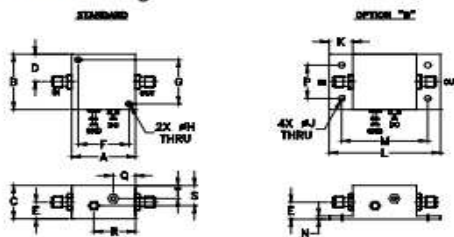
Open load is not recommended, potentially can cause damage.  
With no load derate max input power by 20 dB

#### Maximum Ratings

Operating Temperature	-20°C to 71°C
Storage Temperature	-55°C to 100°C
DC Voltage	+17V Max.

Permanent damage may occur if any of these limits are exceeded.

#### Outline Drawing



#### Outline Dimensions (inch / mm)

A	B	C	D	E	F	G	H	J	K	L	M	N	P	Q	R	S	T	wt.
1.25	1.25	.75	.63	.36	1.000	1.900	.125	.125	.46	2.18	1.668	.06	.750	.50	.80	.45	.29	grams
31.75	31.75	19.05	16.00	9.14	25.40	48.26	3.18	3.18	11.68	55.37	42.65	1.52	19.05	12.70	20.32	11.43	7.37	36

#### Notes

- Performance and quality attributes and conditions not expressly stated in this specification document are intended to be excluded and do not form a part of this specification document.
- Electrical specifications and performance data contained in this specification document are based on Mini-Circuit's applicable established test performance criteria and measurement instructions.
- The parts covered by this specification document are subject to Mini-Circuits standard limited warranty and terms and conditions (collectively, "Standard Terms"); Purchasers of this part are entitled to the rights and benefits contained therein. For a full statement of the Standard Terms and the exclusive rights and remedies thereunder, please visit Mini-Circuits' website at [www.minicircuits.com/MiniCircuitsTerms.jsp](http://www.minicircuits.com/MiniCircuitsTerms.jsp)

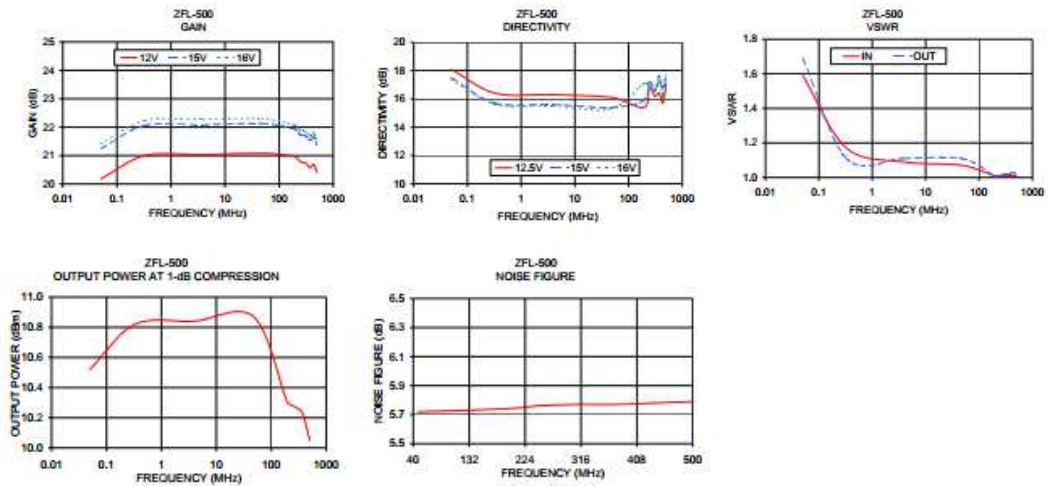


[www.minicircuits.com](http://www.minicircuits.com) P.O. Box 35166, Brooklyn, NY 11235-0003 (718) 934-4500 sales@minicircuits.com

REV. B  
M125292  
ZFL-500  
131015  
Page 1 of 2

*Typical Performance Data/Curves*

FREQUENCY (MHz)	GAIN (dB)			DIRECTIVITY (dB)			VSWR (-1) 15V		NOISE FIGURE (dB) 15V	POUT at 1 dB COMP. (dBm) 15V
	12V	15V	16V	12V	15V	16V	IN	OUT		
0.05	20.18	21.24	21.41	18.10	17.50	17.40	1.59	1.69	—	10.52
0.33	21.00	22.06	22.23	16.40	15.70	15.60	1.17	1.11	—	10.82
3.90	21.03	22.08	22.27	16.30	15.60	15.50	1.09	1.11	—	10.84
47.90	21.08	22.13	22.30	16.10	15.40	15.30	1.07	1.11	5.72	10.87
192.30	20.96	21.93	22.07	15.40	15.90	17.10	1.01	1.01	5.74	10.31
243.60	20.79	21.74	21.90	16.80	17.20	16.80	1.01	1.01	5.76	10.28
307.70	20.74	21.70	21.84	16.20	16.60	16.60	1.01	1.02	5.77	10.26
371.80	20.58	21.55	21.70	16.40	17.20	17.60	1.01	1.02	5.77	10.23
435.90	20.69	21.65	21.80	15.70	16.80	16.10	1.01	1.03	5.78	10.14
500.00	20.40	21.36	21.52	17.10	17.70	16.70	1.01	1.02	5.79	10.05



**Notes**  
 A. Performance and quality attributes and conditions not expressly stated in this specification document are intended to be excluded and do not form a part of this specification document.  
 B. Electrical specifications and performance data contained in this specification document are based on Mini-Circuit's applicable established test performance criteria and measurement instructions.  
 C. The parts covered by this specification document are subject to Mini-Circuits standard limited warranty and terms and conditions (collectively, "Standard Terms"); Purchasers of this part are entitled to the rights and benefits contained therein. For a full statement of the Standard Terms and the exclusive rights and remedies thereunder, please visit Mini-Circuits' website at [www.minicircuits.com/MCLStore/terms.jsp](http://www.minicircuits.com/MCLStore/terms.jsp)



[www.minicircuits.com](http://www.minicircuits.com) P.O. Box 35166, Brooklyn, NY 11235-0003 (718) 934-4500 [sales@minicircuits.com](mailto:sales@minicircuits.com)



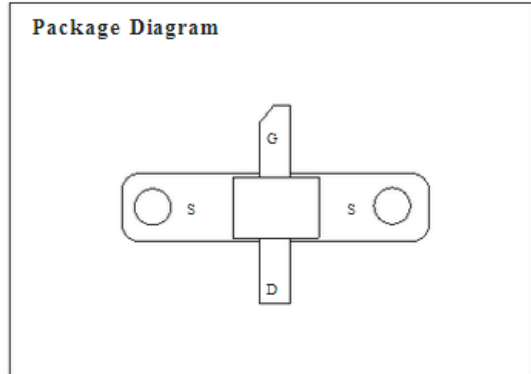
# CFH2162-P3

Advanced Product Information  
 May 1996 (1 of 2)

## 1.8 to 2.0 GHz +36 dBm Power GaAs FET

- Features**
- t High Gain
  - t +36 dBm Power Output
  - t Proprietary Power FET Process
  - t >45% Linear Power Added Efficiency
  - t +33 dBm with 30 dBc Third Order Products

- Applications**
- t PCS/PCN Base Stations
  - t Wireless Local Loop



**Description**

The CFH2162-P3 is a high-gain, linear FET intended for driver amplifier applications in high-power systems, and output stage usage in medium power applications at power levels up to +36 dBm. The device is easily matched and pro-

vides excellent linearity at 4 Watts. Manufactured in Celeritek's proprietary power FET process, this device is assembled in a power flange package.

Specifications (TA = 25°C) The following specifications are guaranteed at room temperature in Celeritek test fixture at 1.95 GHz.

Parameters	Conditions	Min	Typ	Max	Units
Vd = 10V, Id = 1100 mA (Quiescent)					
P-1dB		36.0	37.0	—	dBm
G-1 dB		13.0	14.0	—	dB
3rd Order Products (1)		30	35	—	dBc
Efficiency	@ P1dB	—	45	—	%
Vd = 8V, Id = 1300 mA (Quiescent)					
P-1dB		—	36.0	—	dBm
G-1 dB		—	13.0	—	dB

Parameters	Conditions	Min	Typ	Max	Units
gm	Vds = 2.0V, Vgs = 0V	—	1700	—	mS
Idss	Vds = 2.0V, Vgs = 0V	—	2.8	—	A
Vp	Vds = 3.0V, Ids = 65 mA	—	-1.8	—	Volts
B V G D	Igd = 6.5 mA	20	24	—	Volts
© JL (2)	@150°C TCH	—	8	—	°C/W

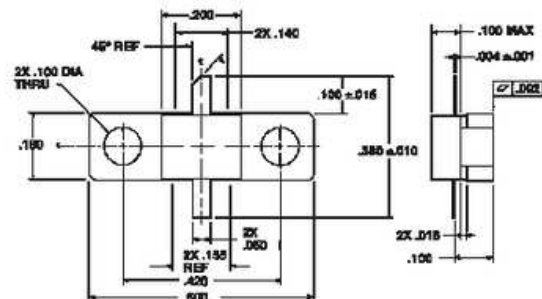
**Absolute Maximum Ratings**

Parameter	Symbol	Rating
Drain-Source Voltage	V D S	15 V (3)
Gate-Source Voltage	V G S	-5V
Drain Current	I D S	Idss
Continuous Dissipation	PT	10W
Channel Temperature	T C H	175°C
Storage Temperature	T S T G	-65°C to +175°C

**Notes:**

1. Sum to two tones with 1 MHz spacing = 33 dBm.
2. See thermal considerations information.
3. Maximum potential difference across the device (Vd + Vg) cannot exceed 18V.

**Power Flange Package Physical Dimensions**



3236 Scott Boulevard

Santa Clara, California 95054

Phone: (408) 986-5060

Fax: (408) 986-5095